12-16-2019

IDENTIFICATION OF NOVEL DRUGGABLE TARGETS IN TWO MEMBERS OF MONONEGAVIRALES

Venice DuPont

IDENTIFICATION OF NOVEL DRUGGABLE TARGETS IN TWO MEMBERS OF *MONONEGAVIRALES*

by

VENICE DU PONT

Under the Direction of Richard K. Plemper, PhD

ABSTRACT

Measles virus (MeV) is considered one of the most contagious human viruses and has recently been declared endemic again in several countries despite a highly efficacious vaccine. The viral RNA dependent RNA polymerase (RdRP) is a heterologous complex comprised of the large protein (L), which provides all catalytic domains for RNA synthesis, and the phosphoprotein (P), which provides chaperone support for L and mediates the interaction between L and the ribonucleoprotein complex (RNP). Though essential for polymerase function, the interface between P and L remains poorly characterized, as well as the role of P in RdRP advancement along the RNP. Through biochemical interface mapping, functional assays, and domain swapping

of P, we have identified a bipartite L binding domain on P. One domain consists of a conserved helical motif upstream of the oligomerization domain (OD), and the second is a face of the P X-domain (PXD). Using stoichiometrically-controlled trans-complementation studies and applied mathematical modeling, we also determined the PXD:L interaction to be mutually exclusive to the PXD:N interaction. These findings suggest a model that centers PXD as a master regulator of RdRP advancement.

Rabies virus (RABV) causes a severe and 100% fatal neurological disease that is vaccine preventable and treatable prior to the onset of clinical symptoms. The post-exposure prophylaxis (PEP) for RABV treatment is prohibitively expensive, especially in developing countries where the majority of cases occur and does not confer cross-protection against the newly emerging phylogroup II lyssaviruses. To address the unmet clinical need for cross-protective anti-RABV therapeutics, we developed and implemented an innovative high-throughput screening approach utilizing a novel single cycle RABV reporter strain maintained in BSL-2 laboratory conditions. From our extensive screening library, we have identified the first direct-acting multi-strain RABV entry inhibitor, GRP-60367. Resistance profiling of GRP-60367 revealed escape mutations that accelerate the fusion kinetic of the RABV glycoprotein (G). We have solved two of the feasibility issues with current RABV antiviral drug discovery: i) BSL-2^{+} RABV containment restraints and ii) reliable drug efficacy determination, thus paving the way for future drug discovery campaigns to alleviate the deficit and cost of current therapeutic options against lyssaviruses.

INDEX WORDS: measles virus, rabies virus, RNA-dependent RNA polymerase, protein-protein interactions, antiviral, drug discovery, high-throughput screening

IDENTIFICATION OF NOVEL DRUGGABLE TARGETS IN TWO MEMBERS OF *MONONEGAVIRALES*

by

VENICE DU PONT

A Dissertation Submitted in Partial Fulfillment of the Requirements for the Degree of

Doctor of Philosophy

in the College of Arts and Sciences

Georgia State University

2019

IDENTIFICATION OF NOVEL DRUGGABLE TARGETS IN TWO MEMBERS OF *MONONEGAVIRALES*

by

VENICE DU PONT

Committee Chair: Richard Plemper

Committee: Margo Brinton

Sang-Moo Kang

Electronic Version Approved:

Office of Graduate Studies

College of Arts and Sciences

Georgia State University

December 2019

DEDICATION

This dissertation is dedicated to my mother and husband, for their incredible support and patience

ACKNOWLEDGEMENTS

First and foremost, I would like to express my sincerest gratitude to my advisor Dr. Richard Plemper for the invaluable guidance and support he has given to me during this incredible journey. Many thanks to my committee members Dr. Margo Brinton and Dr. Sang-Moo Kang, who have provided invaluable and perceptive feedback for my dissertation projects. I would also like to thank the Plemper lab members and GSU colleagues, past and present, for their incredible advice and friendship over the years.

TABLE OF CONTENTS

LIST OF TABLES

LIST OF FIGURES

1 LIST OF ABBREVIATIONS

MeV	Measles Virus
RABV	Rabies Virus
MuV	Mumps Virus
PIVs	Parainfluenza Viruses
HeV	Hendra Virus
NiV	Nipah Virus
SeV	Sendai Virus
RPV	Rinderpest Virus
PPRV	Pestes-des-Petites Ruminants Virus
MOKV	Mokola Virus
N	Nucleoprotein
P	Phosphoprotein
M	Matrix Protein
G	Glycoprotein
H	Attachment Protein
F	Fusion Protein
L	Large Protein
RNP	Ribonucleoprotein Complex
RdRP	Viral RNA-dependent RNA Polymerase
IGS	Intergenic Junctions
R_0	Reproduction Number

ADEM	Acute Disseminated Encephalomyelitis
MIBE	Measles Inclusion Body Encephalitis
SSPE	Subacute Sclerosing Panencephalitis
IG	Immunoglobulin
PPI	Protein-Protein Interfaces
SLAM	Signal Lymphocyte Activation Molecule
N-4	Nectin-4
PXD	Extreme C-terminal Domain of P
MoRE	P Molecular Recognition Element
Ncore	N-terminal Core Domain
Ntail	C-terminal Intrinsically Disordered Tail Domain
$\mathbf{N_{NTD}}$	MeV N N-terminal Domain
$\mathbf{N_{CTD}}$	MeV N C-terminal Domain
CRI-VI	MeV L Conserved Regions
LR	MeV L Long Region
HR	MeV L Hinge Region
$\mathbf{P_{NBD}}$	MeV P N^0 Binding Domain
OD	MeV P Oligomerization Domain
$\mathbf{K_D}$	Dissociation Constant
coIP	Co-Immunoprecipitation
Y2H	Yeast-2-Hybrid
HSP90	Heatshock Protein 90
PEP	Post-Exposure Prophylaxis Treatment

hRIG	Human-Derived Anti-RABV Immunoglobin
MP	Milwaukee Protocol
IFN-α	Interferon-α
BBB	Blood-Brain Barrier
DAA	Direct-Acting Antiviral
HTA	Host-Targeting Antiviral
EC_{50}	50% Effective Dose Concentration
CC_{50}	50% Cytotoxic Concentration
SI	Selectivity Index
RNAi	RNA Interference

1 INTRODUCTION

1.1 *Mononegavirales* Overview

The viruses of the order *Mononegavirales* are characterized by enveloped virions of variable morphologies that shelter a linear non-segmented, negative sense RNA genome. The viral genome is encapsulated by nucleoprotein (N) which forms the ribonucleoprotein complex (RNP) [1]. The genome encodes a linear sequence of genes, with limited overlaps, and each ORF is divided by noncoding intergenic junctions (IGS). Each gene is expressed as an individual transcription unit that is bordered by short transcription start and termination sequences recognized by the viral RdRP. The 3′ end of the genome contains the leader sequence that directs the RdRP for transcription initiation and mRNA is transcribed by sequential interrupted synthesis [2]. Transcription for members of *Mononegavirales* occurs with a gradient that results in decreasing expression of proteins further down the genome [3]. The viral RdRP contains an enzymatic capping domain that is conserved throughout the order called the GDP polyribonucleotidyltransferase (PRNTase). This domain caps 5′ viral mRNA using unique capping mechanism that co-transcriptionally incorporates a GDP to the cap structure, which is then methylated at the G-N^7 using the viral RdRP methyltransferase (MTase) domain [4, 5]. This method is in contrast to the traditional capping strategy employed by eukaryotic cells and viruses with positive sense RNA genomes, which utilizes the enzyme RNA 5′ -triphosphatase (RTPase) for phosphate removal that results in GDP followed by transfer of a GMP moiety to the cap structure by guanylytransferase (GTase) [6]. The RdRP punctuates mRNA synthesis by adenylation of viral mRNA via iterative transcription from a short polyU tract at the end of each gene [1].

The order of major structural proteins is highly conserved amongst members of *Mononegavirales* and include N, phosphoprotein (P), matrix protein (M), envelope proteins, and the large protein (L) [1]. The RNP comes pre-loaded with the viral RdRP, which consists of a dimeric heterocomplex of L and P. To ensure particle assembly and budding, vital contacts are made by the RNP with M coating the luminal side of the viral envelope bilayer. M in turn interacts with the cytosolic tail of surface glycoproteins (the attachment (H), and fusion (F) proteins, for measles virus (MeV) or G, for rabies virus (RABV). N, P, M, envelope proteins, and L proteins are standard for all members of the order, though there are several viral genomes that encode additional proteins. For example, several viruses encode for virulence factors such as MeV C and V proteins, which are transcribed by leaky scanning and mRNA editing, respectively, RdRP processivity factors, or separation of function for attachment and fusion, e.g. the MeV receptor protein, H, and its fusion protein F. Of the eight families that comprise the viral order *Mononegavirales*, two of which harbor the most contagious virus, MeV, within *Paramyxoviridae,* and the most lethal virus, RABV, within in *Rhabdoviridae,* both of which continue to cause significant morbidity and mortality for humans worldwide [7, 8].

Although efficacious vaccines exist for MeV and RABV, there are currently no drugs licensed for therapeutic intervention. It was the goal of the first chapter of this dissertation to determine the critical contacts between MeV polymerase core components (L and P). We determined that the L:P interaction is bipartite. Based on this discovery, we also present a new model of polymerase advancement along the viral genomic template due to a dynamic interaction between extreme C-terminal domain of P (PXD) and L. Furthermore, due to conservation of the molecular architecture of the PXDs among *Paramyxoviridae*, we hypothesize that this interaction could be exploited as a potential drug target.

In the second chapter, this dissertation details our development and implementation of a novel high-throughput screening (HTS) protocol for small-molecule drug discovery against RABV. From our screening library of over 150,000 compounds, we identified GRP-60367 as a potent entry inhibitor of RABV. Discovery of this compound not only demonstrates the feasibility of a large-scale RABV drug discovery campaign, but further resistance profiling of GRP-60367 shed new light into RABV fusion kinetics.

1.2 Chapter 1: Bipartite interface of the measles virus phosphoprotein X domain with the large polymerase protein regulates viral polymerase dynamics

1.2.1 Measles Virus Disease and Treatment

With over 100,000 deaths annually, MeV continues to be a leading cause of vaccine-preventable morbidity and mortality for children worldwide. MeV is identified as one of the most infectious respiratory viruses with a basic reproduction number (R_0) ranging between 12 to 18, meaning that every infected individual has the capacity to cause 12-18 secondary cases [9]. As the archetypal member of the family *Paramyxoviridae*, MeV is a lymphotropic virus that spreads via nasopharyngeal droplets or airborne aerosols and clinical symptoms begin to arise 9-19 days post-exposure. Early infection begins in the lymphoid tissue of the lower respiratory tract, and progressively spreads to infiltrate epithelial tissues of the upper respiratory tract [10]. Prodromal symptoms include fever and malaise coupled with cough, coryza, and conjunctivitis. Also, during the early stages of infection, white lesions on the buccal mucosa known as Koplik's spots appear. The erythematous maculopapular skin rash characteristic of clinical MeV disease begins several days later. It starts behind the ears, spreads to the face and eventually covers the rest of the body [11]. Although MeV infection is typically cleared by the patient and results in life-long immunity, 4-11 of every 100,000 cases can result in fatal CNS complications such as

acute disseminated encephalomyelitis (ADEM), measles inclusion body encephalitis (MIBE), or subacute sclerosing panencephalitis (SSPE) [12-15]. The late-onset SSPE occurs within 7-10 years. A tri-residue motif within the M protein has been suggested to serve as a molecular determinant for SPPE because it promotes trans-synaptic migration of viral particles, though the exact mechanism involved remains undetermined [16]. MeV also induces immunosuppression up to 2-3 years post-infection, resulting in a predisposition to bacterial superinfections and increased risk of mortality [17]. Although there is a highly efficacious live-attenuated MeV vaccine readily available, there has been a global resurgence of MeV cases and within the United States, with over 1000 cases reported this year alone. Post-exposure prophylaxis of MeV infection involves vaccination, if exposure is under 72 hours, or a dose of human immunoglobulin (IG) within six days of exposure [18, 19]. Administration of vaccine or IG within the limited time window presents a challenge while cost and requirement of cold-chain for treatment with IG are also barriers for treatment. Another consideration is that treatment with IG also does not confer immunity, and, additionally, interferes with the immune response to vaccination [20]. For cases involving neurological complications there are no standard treatment protocols and typically broad-spectrum antivirals, such as IFN-α and/or ribavirin, were administered. However, these treatments have questionable efficacy and SSPE continues to have a 95% fatality rate [21-23]. The increase in cases as well as the chance of progression toward life-threatening neurological disease has highlighted the unmet need for MeV specific antivirals.

Several antiviral strategies have been proposed to combat MeV infection, such as peptide inhibitors, natural compounds, and small-molecule inhibitors including nucleoside analogs and non-nucleoside analog inhibitors [21-33]. Short-chain peptide inhibitors designed to specifically target critical viral protein-protein interfaces (PPI) have been suggested as a potential antiviral

therapeutic option against MeV. Outwardly, designer peptides are a promising antiviral solution due to their low cytotoxicity, and high specificity to their target. Despite promising *in vitro* efficacy, advancement of peptides as a therapeutic solution remains hindered by poor oral bioavailability, relatively short half-life, poor membrane permeability, and the high cost of production [21, 33]. Natural compounds have also been extensively explored as antiviral options, yet they are considered to be poor candidates due to inherent cytotoxicity, high efficacious dose requirements, and unknown mechanisms of action [34].

Due to its critical role in the viral life cycle, its highly conserved nature, lack of cellular orthologs and its multifunctional catalytic domains, the RdRP complex presents an enticing target for anti-viral therapy. The RdRP also engages in important PPI such as the L-P binding domain [35]. The only approved nucleoside analog against MeV to date remains ribavirin, a broad-spectrum RdRP inhibitor with reportedly poor efficacy and a plethora of adverse side-effects [21]. Recently, a highly encouraging non-nucleoside inhibitor of the MeV RdRP, ERDRP-0519, has been identified and characterized as both orally bioavailable and highly efficacious against multiple MeV genotypes. Furthermore, drug treatment resulted in the generation of attenuated escape mutants. The compound showed *in vivo* efficacy in the closely related canine distemper virus (CDV)/ferret model when given prophylactically (50 mg/kg twice daily) with a substantial decrease in viral load and delayed lymphopenia [32]. Although, prophylactic treatment with the drug prolonged the lives of CDV-infected ferrets for two weeks, they eventually succumbed to disease resulting from a lack of proper immune stimulation. Animals that received the drug therapeutically mounted a strong innate and adaptive antiviral immune response and survived re-challenge. These studies clearly demonstrated the potential

antiviral impact of targeting the viral polymerase as well as demonstrated that the delicate balance of drug administration and immune stimulation must also be considered.

1.2.2 MeV Lifecycle

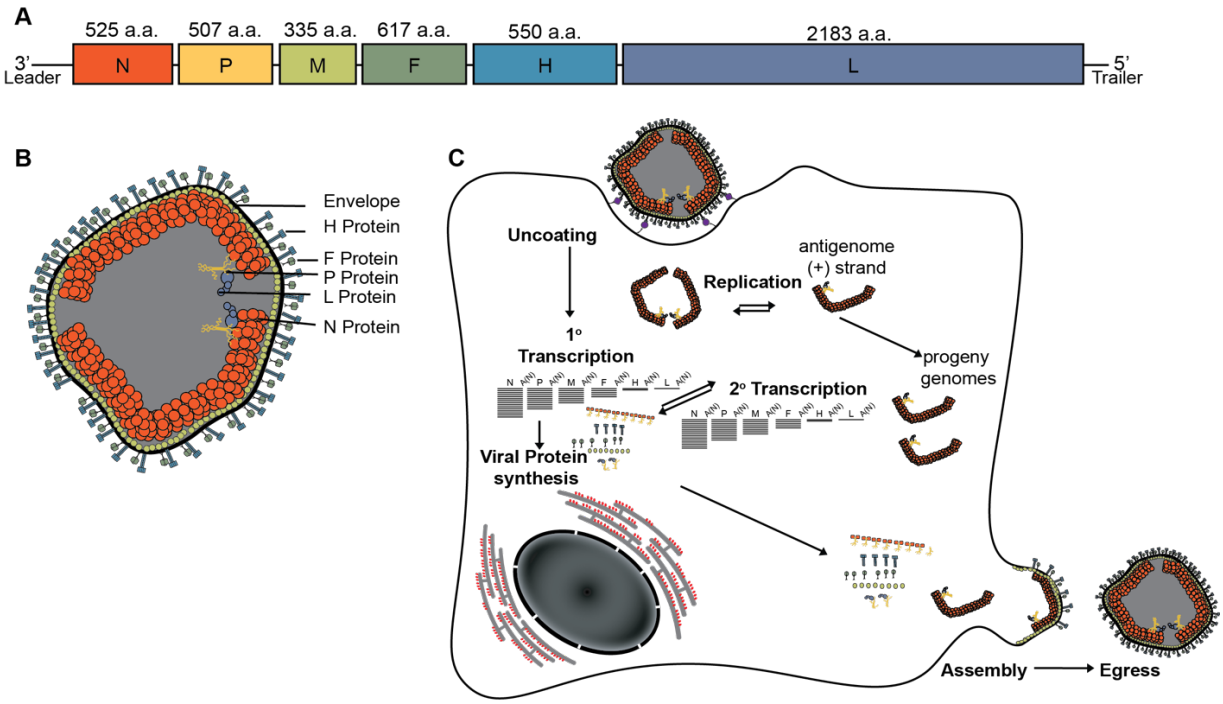

Figure 1. *Measles virus lifecycle **A)** Schematic of genomic organization of MeV **B)** Illustrative depiction of MeV virion including Envelope (black), Attachment protein (H, light blue), Fusion protein (F, green), Phosphoprotein (P, yellow), Large protein (L, lavender) and Nucleoprotein encapsidated genome (N, orange). C) Graphic depiction of MeV replication.*

MeV is in the genus *morbillivirus* within the viral family *Paramyxoviridae*, which also houses a wide range of other clinically relevant respiratory pathogens, including mumps virus (MuV), the parainfluenza viruses (PIVs), and the newly emerging zoonotic Hendra (HeV), and Nipah (NiV) viruses. The MeV viral genome contains approximately 16,000 nucleotides and is encapsidated by the N protein to form the characteristic 20 nm herringbone-like RNP complex, all enclosed within a host-derived lipid bilayer membrane [36] (**Figure 1A, B**). The surface molecules of MeV are the tetrameric attachment protein (H), which mediates receptor binding,

and the trimeric type-1 fusion protein (F) [37]. The MeV H tetramer has a globular head domain containing the receptor binding sites, a stalk domain that is arranged in a four-helix bundle conformation, and four transmembrane domains [38]. F trimerization is thought to occur within the endoplasmic reticulum, where it is also predicted to hetero-oligomerize with H [39]. F is first synthesized as an F_0 precursor, which is then cleaved into two distinct polypeptides, F_1 and F_2, by host-derived furin proteases during transport through the trans-golgi network [40]. Furin cleavage of F loosens its interaction with H, an event that promotes F bioactivity [41]. The H:F complexes are expressed on the infected cell surface after traveling through the cell secretory pathway. Signal lymphocyte activation molecule (SLAM) and nectin-4 (N-4) are the primary host-cell receptors recognized by H for all wildtype MeV strains, while CD46 is only recognized by Edmonston and all vaccine strains derived from it [42-44]. F is maintained in a metastable pre-fusion state through its interaction with H. However, upon receptor binding, H undergoes conformational changes that result in a release of the F trimers. This release triggers the F stalk domains to extend and the HRA domain refolds into an extended coiled-coil to expose a hydrophobic fusion peptide. The fusion peptide inserts into the target membrane and forms the "pre-hairpin" structure. This structure begins to collapse, causing membrane curvature of both the viral envelope and host cell target membrane. Finally, the HRB and HRA domains form a stable six-helix bundle that bring the phospholipids of each membrane into close enough proximity that allows lipid-mixing and fusion pore formation. It is from this pore, that viral genetic material is released from the virion and enters the host cell. [37, 45-47]. The viral RNP serves as a template for cytosolic replication by the pre-assembled RdRP complex that begins primary transcription followed by translation of viral proteins by the host machinery. Although the mechanism for the switch from transcription to viral RNA replication remains unclear, excess

RNA-free N (N^0) protein has been suggested as a trigger [48]. As nascent viral genomes are synthesized, they are concurrently encapsidated by N. Virion assembly is orchestrated by direct interaction of N with M proteins, which in turn interact with the surface glycoproteins. Fully assembled infectious MeV virions egress in an ESCRT-independent manner [49-51] (Figure 1C).

1.2.3 MeV Transcription and Replication

Replication and transcription of the MeV genome is accomplished through the concerted cooperation between three viral proteins, N, P, and L. The bioactive RdRP is a hetero-oligomeric complex comprised of L and P. L provides the enzymatic domains required for RNA synthesis, capping, and cap methylation, while P provides L-chaperoning support and bridges the interaction of L to the RNP through direct interaction with N. The RdRP can function both as transcriptase and replicase, though the exact mechanism for the switch between functions remains unknown. It has been shown, however, that an accumulation of N^0P complexes promotes replication over transcription [48]. The viral genome contains *cis*-acting elements that provide transcription cues for the RdRP such as those for initiation, polyadenylation, and termination of viral mRNA synthesis. RdRP begins all transcription events at the leader sequence at the 3′ end of the antigenome and progresses through the template in a continuous cycle of N-RNA disassociation, mRNA capping, mRNA synthesis, non-templated polyadenylation followed by scanning through IGS for the next gene initiation sequence [52]. Re-initiation of mRNA synthesis is only partially efficient, resulting in an attenuation gradient that varies between IGS for each successive gene [48, 53]. Access of L to the template involves a dynamic interplay of attachment and release between the PXD and a highly conserved region that acts as a P molecular recognition element within the disordered tail of N (MoRE) [54]. Although the exact mechanism remains unknown, one predominant theory proposes that P acts as an axle to which L

remains fixed, while PXD proceeds in a dynamic cartwheel fashion to engage adjacent MoRE domains of neighboring Ns [55]. What is also unknown is the trigger resolving PXD binding to MoRE, since PXD and MoRE form a highly stable four-helix bundle.

1.2.4 Viral Proteins involved in MeV RNA synthesis

1.2.4.1 The Nucleoprotein (N)

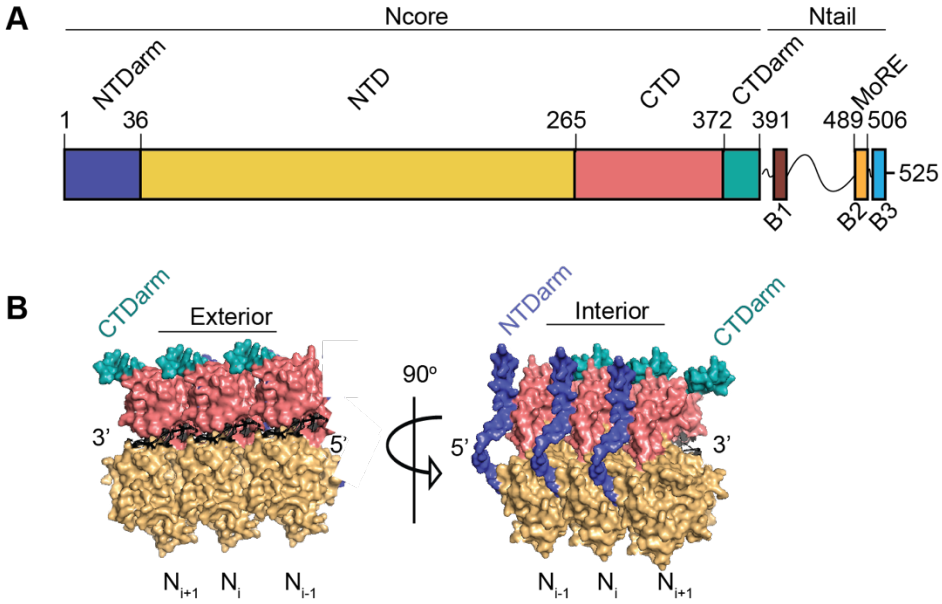

Figure 2. *The Measles Nucleoprotein* ***A)*** *Schematic representation of MeV N organization* ***B)*** *Structure of oligomeric interactions between individual N monomers. The CTDarm is aqua, the NTDarm is purple and RNA is black. The CTD is in pink, and the NTD is yellow* ***(PDB: 4UFT).***

The N protein of MeV consists of 525 residues and is divided into an N-terminal core domain (Ncore) (residues 1-391) and a C-terminal intrinsically disordered tail domain (Ntail) (residues 392-525) (**Figure 2A**). Ncore is further divided into two globular domains, the N-terminal domain (N_{NTD}) (residues 37-265) and the C-terminal domain (N_{CTD}) (residues 266-372), which are linked by a short hinge region that acts as the binding cleft for the genomic viral RNA [56-59]. Homo-oligomerization of N is mediated by interaction of two Ncore subdomains, the

N_{NTDarm} (1-36) and the N_{CTDarm} (373-391) [60]. Recent cryo-EM structure determination of RNP revealed that N oligomerization occurs through the binding of an N_{NTDarm} protomer into a groove of the N_{CTDarm} of the neighboring N monomer (**Figure 2B)** [57, 61]. The highly disordered Ntail contains three highly conserved regions, called boxes 1 (400-420), 2 (489-506), and 3 (517-525) [59]. Ntail is also critical in the spatial organization of the Ncore protomers by ioccupying the space between each successive rung of the N:RNA helix. This organization causes approximately the first 50 residues of Ntail to be buried within the RNP helical capsid [58, 62]. It has also been shown that removal of Ntail increases rigidity of the N:RNA helix, causing decreased diameter and pitch of the total nucleocapsid structure [63]. The box 2 of Ntail is responsible for interacting with the PXD through an intrinsically disordered region, called MoRE. Prior to PXD binding, MoRE adopts an equilibrium between partially α-helical and fully unfolded [64]. Mutagenesis studies performed to investigate the binding kinetics between PXD and MoRE have revealed that the binding affinity of the complex is finely tuned to ensure efficient transcription and replication [65]. Of course, mutations that completely disrupt the interaction abolish polymerase activity. However, those mutations that resulted in an increased binding affinity, such as PXD_{F497A}, are associated with decreased transcription elongation rates [66, 67]. This is further supported by the observation that circulating MeV strains contain only substitutions of residues with the least disruptive impact on PXD-MoRE binding affinity [68]. Similar mutagenesis studies have determined that MoRE did not evolve to undergo conformational change into α-helical organization, thus resulting in some steric hindrance when it is induced [69]. The hindrance of α-helical induction results from a dampening effect from the long and disordered region of residues preceding the intrinsically disordered MoRE and further suggests this region as a regulatory element that promotes reiterative dissociation and association

of PXD with MoRE, though the exact mechanism of resolution remains unclear [70]. Although a popular fly-catching model has been proposed in which Ntails are required for polymerase recruitment and subsequent transcription, Ntail truncation studies have shown that boxes 2 and 3 are dispensable for loading RdRP onto the template [71]. Despite activity in minigenome assays, an Ntail truncated recombinant virus was not able to be recovered, thus further supporting the hypothesis that Ntail is critical for preventing premature polymerase termination[72]. Furthermore, internal deletion of residues within Ntail produced viable, albeit attenuated, recombinant MeV and CDV viruses. This study that demonstrated that the region plays more of a regulatory role in transcription rather than polymerase recruitment [72]. Relocation of MoRE from Box 2 to Ncore resulted in restored bioactivity and recovery of recombinant virus [73]. The recovered virus was proficient in promoting replication and mRNA editing, yet the mutant was temperature sensitive and had a flattened transcription gradient. The translocation of MoRE into Ncore demonstrated that Ntail is required for regulating the transcription gradient, thus acting as a vital modulator of gene expression [73]. Not all viral families within the Order *Mononegavirales* encode a C-terminal Ntail, e.g. *Rhabdoviridae* and *Pneumoviridae*. These viruses mediate PXD interaction via Ncore. The evolution of Ntail may have provided newly emerging paramyxoviruses with enhanced N capabilities, beneficial host interactions, and an extra level of regulation of gene expression [73]

1.2.4.2 The Large Protein (L)

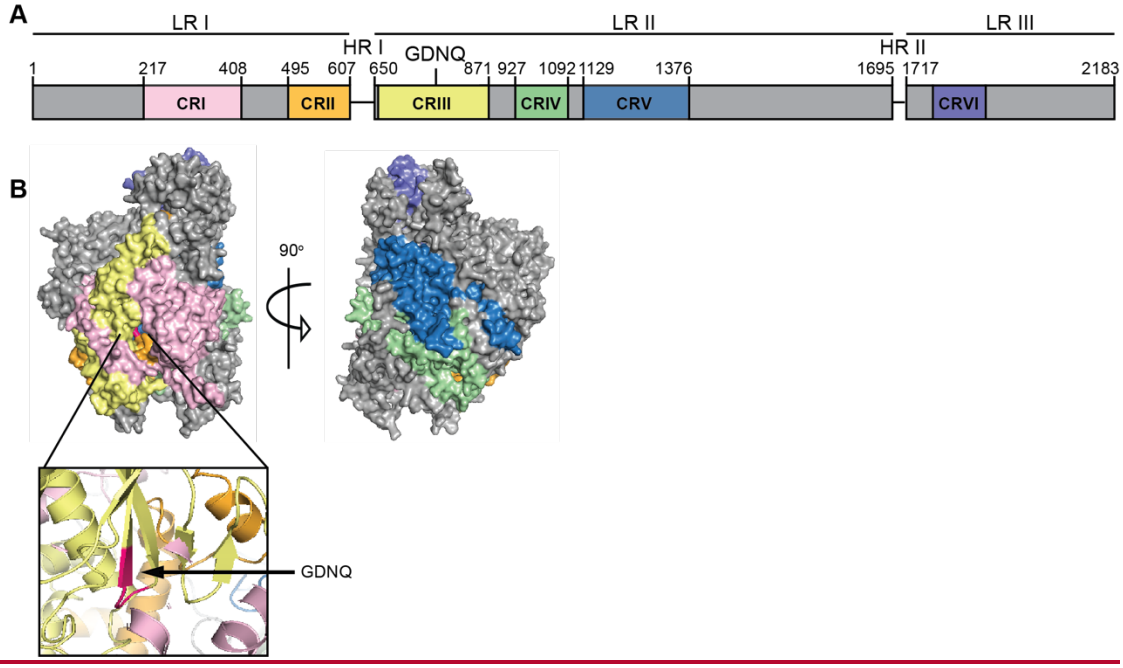

Figure 3. *The Measles Large Protein* ***A)*** *Schematic representation of L protein organization. Long regions (LR), Conserved regions (CRI, pink; CRII, orange; CRIII,yellow; CRIV, green; CRV, blue; CRVI, purple), Hinge regions (HR) and catalytic GDNQ motif are denoted. Numbers represent amino acid numbering N-terminal to C-terminal orientation.* ***B)*** *MeV homology model based on vesicular stomatitis virus (VSV) L cryoEM structure* ***(PDB: 5A22)****, colored regions depict CRI-VI and GDNQ site (magenta) surface model and ribbon form in 20Å resolution.*

Analogous to all *Mononegavirales members,* the MeV L is comprised of approximately 2,200 nucleotides, and provides all of the catalytic functions required for viral RNA transcription and replication such as phosphodiester bond formation, mRNA capping and methylation, and mRNA polyadenylation. The L sequence is organized into six highly conserved regions (CRI-VI) (**Figure 3A, B**). The P binding domain was determined to reside within the first 408 residues of L, which includes part of CRI [74, 75]. The RNA recognition site is found within CRII. CRIII contains the catalytic center with the GDN motif identified as essential for phosphodiester bond formation during viral mRNA synthesis [76]. The L proteins of all non-segmented negative

sense RNA viruses, including MeV, contain a PRNTase-like domain suggesting that they share an unconventional capping mechanism as shown for vesicular stomatitis virus (VSV), discussed in Chapter 2 [4, 5]. This is in contrast to previously published data that suggest the paramyxovirus L protein uses GTase and RTPase activities for capping [77, 78]. Without an equivalent trans-capping assay to the one used to establish VSV L's unique capping mechanism, we cannot definitively assign a specific capping activity to the paramyxovirus L. The L sequence is divided into 3 conserved long regions (LR) with variable sequences between, called hinge regions (HR). HRI (residues 607-650) is less tolerant of epitope tag insertion than HRII (residues 1695-1717) suggesting less flexibility in HRI [79]. Based on these data along with *in silico* protein folding and sequence analyses, it was determined that the first 1,708 N-terminal residues (consisting of LR1 and LR2), which include the catalytic center along with the P and putative L interaction sites of the L protein, form an independent folding domain [80]. Currently, there are no high-resolution structural data available for any of the *Paramyxoviridae* L proteins. Recently, the structure of the L protein for respiratory syncytial virus (RSV) has been solved by cryoEM to a resolution of 3.2Å. Within this structure the phosphoprotein wraps around L with the C-terminal RNP binding domain of one monomeric arm, and has a second L contact point with its oligomerization domain [81]. This structure was revealed one month after the findings of this dissertation were published; however, the structure not only bolsters our findings of a bipartite interface, but also suggests there is a shared molecular architecture with the RdRP complexes of other nonsegmented negative-sense RNA viruses as well. There is also a near atomic resolution (3.8Å) structure for VSV L solved by cryo-electron microscopy that includes three enzymatic domains (the polymerization domain, PRNTase, and MTase), and two structural domains [82]. A loop from the capping domain was also observed to project into the catalytic site, suggesting a

role in priming that is predicted to enhance fidelity and couple initiation with capping. This location of the priming loop also suggests dynamic changes in L confirmation after initiation that result in the loop receding to make room for the nascently synthesized RNA, a mechanism similar to the reovirus polymerase [83]. P is required by MeV L for stabilization and function, yet the exact location required for the interaction remains unclear. The VSV L structure was determined in the presence of a small N-terminal P fragment that is sufficient for inducing a structural initiation confirmation that promotes RdRP processivity of a non-encapsidated RNA template. However, the VSV P peptide was not resolved in the cryo-EM reconstruction [82, 84]. Although the critical residues and mechanism of P interaction with L remained unclear, it was suggested that the P binding domain may lie within the first 408 residues of MeV L and stabilizes the independently folded domains [82].

1.2.4.3 The Phosphoprotein (P)

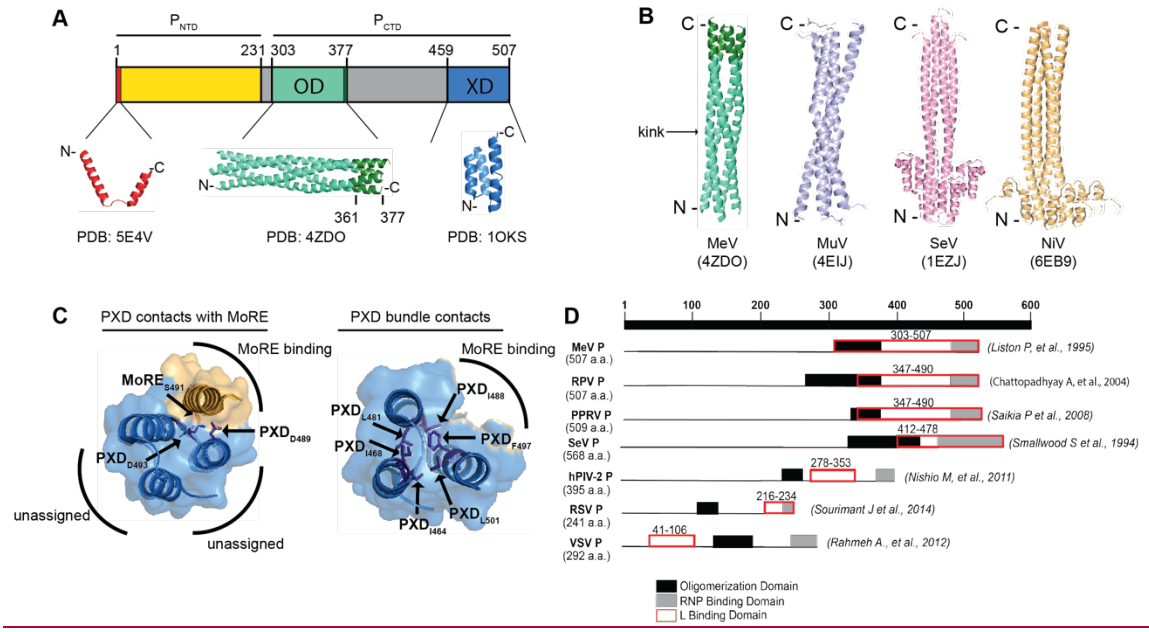

Figure 4. *The Measles Phosphoprotein* ***A)*** *Schematic representation of P protein organization. The N-terminal region of P (P_{NTD}, yellow), C-terminal region of P (P_{CTD}), oligomerization domain (OD, green), and the extreme C-terminal domain (XD, blue) are annotated by residue numbering. Residues 361-377 within the OD are dark green.* ***B)*** *ODs of closely related paramyxoviruses: MeV (green, PDB: 4ZDO), MuV (purple, PDB: 4EIJ), Sendai virus (pink, SeV, PDB: 1EZJ), NiV (yellow, PDB: 6EB9)* ***C)*** *Diagram depicting critical residue interactions with PXD, either with MoRE (left), or the hydrophobic contacts within the PXD bundle (right). The MoRE helix is depicted as yellow, and the PXD is colored blue. (PDB: 1T60)* ***D)*** *Summary depiction of current knowledge of the L binding site for several members of Mononegavirales.*

MeV P, though catalytically inactive, is an essential RdRP cofactor that provides a diverse repertoire of functions critical for viral replication and transcription. These functions include sequestering soluble monomeric RNA-free N (N^0) to prevent unintentional encapsidation of host cell mRNAs, L chaperoning support, and promotion of RNA synthesis by bridging the interaction between L and the RNA template [54]. Reflecting its multifunctional nature, P is a modular protein organized into three distinct and highly conserved domains that are separated by

long disordered regions: the N^0 binding domain (P_{NBD}, a.a. 1-40), the oligomerization domain (OD, a.a. 303-373), and PXD (a.a. 459-507) (**Figure 4A**) [85-87]. The N-terminal residues 1-48 have been previously mapped as the N^0 binding region found to be highly conserved among members of the *Mononegavirales [88]*. Recent high-resolution crystallographic data has unveiled that the molecular mechanism of P interaction with the Ncore occurs through hydrophobic coiled-coil interactions with two adjacent N protomer arms. The resulting steric hindrance is predicted to prevent N protomer oligomerization [56]. These interactions are also presumed to induce a conformational change that lowers RNA binding affinity. For the paramyxovirus, Nipah virus (NiV), a similar mechanism of NTarm interaction was uncovered. However, it was proposed to interfere with the molecular opening and closing switch of N^0, thus rigidifying the NiV P in an open conformation [89]. This mechanism contrasts with that of VSV P, however, since part of the N-terminal region of VSV P extends into the N protomer arm binding cavity and a small helical region binds the hinge region between N_{CTD} and N_{NTD}, thereby extending into the RNA-binding groove [90]. Although the crystal structure of the MeV N^0P complex provides insight into the chaperoning function of P, the mechanism of release of N^0 and subsequent encapsidation of newly synthesized viral genomes still remains poorly understood.

Self-association of P is highly conserved among all members of the *Mononegavirales.* Early predictive modeling of P OD identified heptad repeats spanning residues 303-375. The coiled-coil multimerization domain was later confirmed through X-ray crystallography. The crystal structure of MeV P OD revealed it to be a coiled-coil parallel homo-tetramer that features a tightly packed hydrophobic interface and kinked helices [86]. This finding was in contrast to the recently solved Sendai virus (SeV) P OD, which has a hollow hydrophilic interface and is capped by an N-terminal helical bundle [91]. The crystal structure of MeV P OD and those of

several other paramyxoviruses, e.g. NiV and mumps virus (MuV), exhibit a central kink in the three-dimensional structure due to a break in the heptad repeat (**Figure 4B**) [92]. In the case of MeV, this break is due to a stammer of leucine repeats that induce the coiled-coils to adopt a 3_{10} α-helical conformation. The role of the kink has recently been identified as a regulatory element for viral gene expression [93]. Interestingly, a short disordered section within the C-terminal region of the P OD consisting of residues 361-375 was identified through comparison of two contrasting solved crystal structures of P [94]. Recent studies have further implicated these residues as crucial for L structural stabilization in addition to promoting RdRP bioactivity [93]

Bridging of the polymerase complex to the viral genomic template is orchestrated by the direct interaction of PXD with MoRE. Recent structural characterization of PXD revealed it to be a globular domain organized into three antiparallel α-helices that are held together primarily by hydrophobic intermolecular interactions [87]. The association of MoRE with PXD implements an association-induced folding by the induction of a local α-helical fold of MoRE to form a hetero-four-helix bundle that principally relies on hydrophobic contacts within the large hydrophobic cleft between the α-2/α-3 face of the triangular PXD prism [65] (**Figure 4C**). The PXD-MoRE complex is assembled in a 1:1 stoichiometry and has an equilibrium dissociation constant (K_D) of about 3.1 μM [67]. A complex hydrogen bonding network governs the PXD-MoRE interaction; specifically, association between residues S491 within MoRE and L489 and N493 on PXD reportedly has the most impact on binding [67, 95-97]. Residue F497 within α3 on PXD was also recognized as a critical residue for intermolecular hydrophobic interactions with residues I464, I468, L481, I488, and L501 of PXD that stabilize the α-helical bundle scaffold that promotes MoRE binding without direct interaction (**Figure 4C**) [98]. Furthermore, the folding pathway between native, intermediate, and bound states of PXD to MoRE has been

characterized and shows varying levels of compaction, presumably reflecting a necessity to negotiate association and dissociation with MoRE.

P interacts directly with L to stabilize its native conformation and to mediate physical interaction of the RdRP with the viral genome. Though the L:P interaction is essential for viral transcription and replication, the mode of contact between the two proteins is poorly characterized. Early MeV P mapping studies using co-immunoprecipitation (coIP) and yeast-2-hybrid (Y2H) analyses of truncated P fragments determined that PNT does not harbor the L binding domain [99]. The rinderpest virus (RPV) L binding domain on P was investigated with C-terminally truncated P fragments using Y2H assays. This study resulted in the proposal that the interface comprises the entire P C-terminus (PCT) including the OD [100]. This finding was bolstered by data obtained using the construction of chimeras consisting of swapped morbillivirus PCT domains between rinderpest virus (RPV) and pestes-des-petites-ruminants virus (PPRV) that showed they were still able to form heterologous complexes with the RPV L (**Figure 4D**) [101]. This discovery inferred that shared residues among members of the genus either govern the interaction, or that the interaction is based on a similar molecular architecture conserved across morbilliviruses. Inclusion of the OD within the L binding interface also suggests either a requirement of higher oligomeric order, or that highly conserved residues are involved in the L binding interface. Interestingly, the OD also has several charged residues within its coiled-coil interface. It also contains a stretch of leucines that alter the helical structure resulting in a kink at residue L342. This kink was suggested by Communie, et al. to act as a platform for a binding partner such as L [86]. Replacement of the OD with the tetramerization domain of GCN4 revealed that this kink is dispensable for L interaction, albeit required for bioactivity [92]. Highly conserved residues within the extreme C-terminal region of the OD were

found to be essential for L stability, hinting at a role in binding of L, either directly or indirectly [93]. P is furthermore critical for recruitment of host heatshock protein 90 (HSP90) chaperones that mediate proper folding and solubilization of functional L proteins and the subsequent formation of mature and stable L-P complexes [102]. Though required for maturation of the core RdRP complex, HSP90 is dispensable for bioactivity [102]. The recruitment of HSP90 for chaperoning support has been confirmed for various mononegaviruses including, besides MeV, VSV and NiV. However, the location and purpose of the HSP90 interaction with P has yet to be determined [102-105] .

1.2.5 Aim of Dissertation Chapter 1

The overarching aim of Chapter 1 is to disclose critical elements involved in the L:P interaction, as well as to disclose how the L:P heterocomplex negotiates the viral template through its interaction with MoRE.

The first aim of this study was to characterize and identify critical molecular determinants for L:P interaction. This was accomplished via mutational analysis, alanine scanning, terminal and internal truncations in combination with co-immunoprecipitation studies. Critical residues for L:P binding were confirmed by minireplicon bioactivity studies, and biological relevance was tested by recovery of recombinant viruses.

The second aim of this study was to identify the molecular stoichiometry of MoRE:P:L that is required for RdRP processivity. The stoichiometric ratio of the P:L interaction was determined by trans-complementation of P mutants deficient for L interaction. Secondly, determination of whether the L:P interaction is mutually exclusive to P:MoRE was determined by trans-complementation between P:L and P:MoRE deficient mutants and tested through co-immunoprecipitation as well as minireplicon bioactivity assays.

1.2.6 Chapter 1 Materials and Methods

Cell culture: Baby hamster kidney cells (C-13; ATCC) stably expressing T7 polymerase (BSR-T7/5), African green monkey kidney epithelial (Vero) cells (CCK-81; ATCC), and Vero cells stably expressing human signaling lymphocytic activation molecule (Vero-hSLAM) were maintained in Dulbecco's modified Eagle's medium (DMEM) supplemented with 7.5% fetal bovine serum at 37°C and 5% CO_2 . The stable cell lines were incubated in the presence of G418 (Thermo-Fisher) (100 μg/ml) at every fifth passage. Cells were transiently transfected using GeneJuice (Novagen) according to the manufacturer's instructions.

Molecular biology: Codon-optimized open reading frames encoding MeV IC-B-derived L, L_{1708}, and P were synthesized *in vitro* (GeneWiz). The PΔOD variant lacking residues 303-360 was generated through PCR amplification and re-ligation at an added HindIII site. Yeast-derived GCN4 tetramerization domain was PCR amplified from a previously generated template [47] and inserted using the HindIII site. All alanine substitutions and amino acid changes were performed by site-directed PCR mutagenesis using the QuikChange protocol (Stratagene). C-terminal truncations were performed by PCR mutagenesis and subsequent religation at an added AgeI site. Plasmids encoding the MeV minireplicon luciferase reporter, non-optimized MeV IC-B N, IC-B P, and IC-B L under T7 promoter control, and a full-length cDNA copy of the MeV IC-B genome were previously described [106]. A full-length cDNA of recMeV IC-B expressing P-V463R and P $(361\text{-}364)_{Ala}$ in tandem was generated based on non-codon optimized mutant versions of IC-B P using the NEBuilder® HiFi DNA Assembly kit, introducing an artificial intergenic sequence (IGS) between the two P copies. The assembled recMeV IC-B P-V463R-N-IGS-P $(361\text{-}364)_{Ala}$ cassette was transferred to the full-length genomic plasmid between the N-P

and P-M intergenic junctions using existing XbaI and SalI restriction sites. Mutagenesis success and the integrity of all PCR-amplified nucleic acids was confirmed through Sanger sequencing.

SDS-PAGE, immunoblotting and densitometric quantitations: Cells were transfected in a 6-well plate format (5 x 10^5 cells/well) with 1 μg of plasmid DNA encoding codon-optimized MeV L_{1708} with a C-terminal FLAG epitope tag and 1.8 μg of plasmid DNA encoding MeV P or P mutants, each with a C-terminal HA epitope tag. After 36 hours, cells were washed two times with phosphate buffered saline (PBS) and lysed chemically (50 mM HEPES (pH 7.2), 300 mM NaCl, 1.0 mM EDTA, 1% Triton X-100, protease inhibitors (Roche)). Cleared (10-minute centrifugation at 12,000 rpm, 4°C) lysates were mixed with 5×urea buffer (200 mM Tris/Cl [pH 6.8], 8 M urea, 5% SDS, 0.1 mM EDTA, 0.03% bromophenol blue, 1.5% dithiothreitol). Samples were incubated for 30 minutes at 50°C and separated on 8% SDS-PAGE gels, tank-blotted on polyvinylidene difluoride (PVDF) membranes (Millipore), and subjected to chemiluminescence detection using specific antibodies directed against the FLAG (M2; Sigma) or HA (16B12; Abcam) epitopes, MeV N (clone 83KKII; Millipore Sigma), or against cellular glyceraldehyde-3-phosphate dehydrogenase (GAPDH; 6C; Ambion) as specified. Immunoblots were developed using a ChemiDoc digital imaging system (Bio-Rad) for image visualization. Densitometry was carried out on non-saturated images with global background correction. A full set of positive (wild type P) and negative (equivalent amount of vector DNA replacing P-encoding plasmid DNA) controls were included on each immunoblot, and no normalizations across different blots were conducted.

Native-PAGE: Cells transfected with 1.0 μg MeV P or P mutant-encoding plasmid DNA were harvested after 36 hours as specified above. Cleared lysates were mixed with 1 μl G-250 sample additive (Invitrogen) and 4×Native-PAGE sample buffer (Invitrogen). Electrophoretic gel

fractionation was carried out using 3-12% Bis-Tris gradient gels (Invitrogen) and NativePAGE running buffer. Immunoblotting and detection were performed as outlined above.

Co-immunoprecipitation: Cells (5 x 10^5 cells/well) were transfected with MeV L_{1708} and P or P mutant-encoding plasmid DNA as detailed above. Cells were lysed 24 hours after transfection and cleared lysates incubated with specific antibodies directed against HA or HIS epitopes (HIS.H8; Invitrogen; only for immunodetection after trans-complementation; Figure 5A), or against MeV N (only for immunoprecipitations in Figure 4D) at 4°C, followed by precipitation of immunocomplexes with immobilized protein G (Pierce) in 50 µl bed volume at 4°C. G-protein bound protein samples were washed twice each in cold lysis buffer and PBS, each wash with 20 bed volume equivalents (1 ml), followed by resuspension in 5x urea buffer. Denatured samples were subjected to SDS-PAGE analysis using 8% homogenous gels followed by immunoblotting and detection using specific antibodies directed respectively against the FLAG, HA, or HIS epitopes as described. To calculate relative co-immunoprecipitation efficiencies, densitometric quantitations of co-precipitated L were normalized for those of L co-precipitated by standard P. This approach is based on the rationale that although L turnover rates are increased in the absence of P or presence of L binding-incompetent P mutants, synthesis rates of plasmid-encoded L is independent of P and standard and mutant P have therefore equal initial opportunity to productively interact with nascent L polypeptides.

Minireplicon reporter assay: BSR-T7/5 cells (5,000 cells/well in a 96-well plate format) were transfected in nine technical replicates per condition assessed with plasmids encoding MeV IC-B L (0.02 µg), IC-B N (0.016 µg), the MeV luciferase replicon reporter (0.044 µg), and either IC-B P or P mutants as specified (0.02 µg unless stated otherwise in Figure captions). In all experiments that involved transfecting variable amounts of mutant and wild type

P-encoding plasmid DNA ratios, empty vector (pUC-19) DNA was added in the appropriate amounts to ensure that all transfection reactions received the same total amount of DNA. Firefly luciferase activities were determined 24 hours post-transfection in a Synergy H1 microplate reader (BioTek), using Bright-Glo luciferase substrate (Promega) directly added to the wells and signal detection after a 1 to 2-minute stabilization period. Relative RdRP activities, expressed as percentages of that observed in the presence of wild type P, were determined according to the formula % rel. activity = $(signal_{sample}\text{-}signal_{min})/(signal_{max}\text{-}signal_{min}) \times 100$, with $signal_{max}$ corresponding to cells having received wild type P and $signal_{min}$ corresponding to cells having received equal amounts of pUC-19 in place of P-encoding plasmid. Results calculated for each biological repeat represent the means of the nine technical repeats, and each condition (P mutant, competition or trans-complementation setting) was assessed in at least three biological repeats.

Recovery of recombinant MeV: recMeV were recovered by transfection of BSR-T7/5 cells with full-length antigenomic plasmid (1.25 μg) and the plasmids encoding IC-B N (0.42 μg), IC-B-P (0.54 μg), and IC-B-L (0.55 μg). Transfected cells were overlaid after 48 hours onto Vero-hSLAM cells. Emerging infectious centers were individually transferred to and then passaged twice on Vero-hSLAM cells, followed by whole RNA extraction from infected cells (RNeasy kit; Qiagen), first strand synthesis using random hexamer primers and Superscript III reverse transcriptase (Invitrogen), PCR amplification of synthesized cDNAs using appropriate primers, and Sanger sequencing. Titers of MeV stocks were determined through $TCID_{50}$ titration on Vero-hSLAM cells as described [107].

Viral growth kinetics: Vero-hSLAM cells were plated in 12-well format (1.0×10^5 cells/ well) and infected with recovered viruses, either recMeV IC-B or recMeV IC-B P-V463R-P $(361\text{-}364)_{Ala}$ at a multiplicity of infection (MOI) 0.01 $TCID_{50}$ units per cell for 1-hour, followed

by replacing the inoculum with growth media. To ensure accurate inoculum concentrations, virus stocks were pre-diluted to approximately 5,000 $TCID_{50}$/ml and inoculum titers validated through $TCID_{50}$ titration. Cell-associated viral particles were harvested in 12-hours intervals through scraping of cells in serum-free DMEM, two consecutive freeze/thaw cycles, and clearance centrifugation (2,000 rpm, 4°C). Viral titers in cleared samples were determined through $TCID_{50}$ titration.

Photometric CPE quantitation: Vero-hSLAM cells were plated in a 12-well format (1.0×10^5 cells/well) and infected with either recMeV IC-B or recMeV IC-B P-V463R-P $(361\text{-}364)_{Ala}$ at a MOI of 0.01 $TCID_{50}$/cell for one hour, then inoculum was replaced with growth media. Infected cells were imaged in 2-hour increments over a period of 36 hours post-infection with a Cytation5 automated high content imager with phase contrast microscopy capacity (BioTek). The increase in μm^2 area size covered by individual infectious centers first detected at 24 hours after infection was quantified over time using the Gen5 microplate software program (Ver. 3.05.11) (BioTek). A maximum of four syncytia/well were followed, quantitations are based on 10 distinct syncytia/virus analyzed. CPE kinetics are expressed as fold-change of area size relative to the 24-hour after infection timepoint.

Mathematical models of bioactivity: Based on behavior in native-PAGE, mutant and wild type P co-expressed in the same cell were given equal probability to tetramerize and the mutant occupation of one P monomer was treated independent of the other three monomers. The ratio between mutant (M_x) and wild type (wt) P was denoted as ρ. Adapting a previous approach to a comparable problem [108], the probabilities of the formation of tetramers with different compositions were calculated as follows:

$$P_{4wt} = \left(\frac{1}{1+\rho}\right)^4,$$

$$P_{3wt1M} = 4\left(\frac{1}{1+\rho}\right)^3\left(\frac{\rho}{1+\rho}\right)^1,$$

$$P_{2wt2M} = 6\left(\frac{1}{1+\rho}\right)^2\left(\frac{\rho}{1+\rho}\right)^2,$$

$$P_{1wt3M} = 4\left(\frac{1}{1+\rho}\right)^1\left(\frac{\rho}{1+\rho}\right)^3,$$

$$P_{4M} = \left(\frac{\rho}{1+\rho}\right)^4.$$

A number of interactions of host proteins with MeV P and N have been proposed [109], but very limited insight into this complex interactome precludes integration into rational modeling. We therefore applied a deconstruction approach, concentrating on individual point mutations affecting specific interactions between P-XD and L or N-MoRE, respectively. At any given mutant to wild type P ratio ρ, all five different P tetramer compositions will be present in the system (illustrated in Figure 7D). Two hypotheses regarding the bioactivities of these tetramer species were examined. In both models, the α-values reflect the individual contribution of each of the different P tetramer assemblies to overall bioactivity, with consideration of the relative abundance of each assembly in the system.

i) Linear combination: all tetramers with at least one wild type P monomer is bioactive and their contributions to RdRP bioactivity (A) are linearly additive:

$$A = \sum_{i=1}^{4} \alpha_i P_{iwt} = \alpha_0 P_{0wt4M} + \alpha_1 P_{1wt3M} + \alpha_2 P_{2wt2M} + \alpha_3 P_{3wt1M} + \alpha_4 P_{4wt0M}$$

Assumptions made: all-mutant P tetramers (P_{0wt4M}) are bio-inactive (Figures 7C, 10, 12E), $\alpha_0 = 0$. Therefore, only four weights needed to be fitted; positive weights reflect positive and negative weights negative contributions to overall bioactivity; tetramer species with a weight of 0 are bio-inactive.

ii) Non-linear pairwise P-XD competition: in addition to each tetramer species potentially contributing to bioactivity, a possible impact of competition for binding sites was considered:

$$A = XD\ binding\ to\ L + const.XD\ binding\ to\ MoRE - XDs\ competing\ for\ binding\ to\ L$$

as in:

$$A = \alpha_1 \left(P_{1wt3M} + \frac{P_{2wt2M}}{2} + \frac{P_{3wt1M}}{3} + \frac{P_{4wt0M}}{4} \right) + \alpha_2 P_{MoRE} - \alpha_3 \left[\left(\frac{P_{2wt2M}}{2} \right)^2 + \left(\frac{P_{3wt1M}}{3} \right)^2 + \left(\frac{P_{4wt0M}}{4} \right)^2 \right]$$

Assumptions made: all-mutant P tetramers (P_{0wt4M}) are bio-inactive (Figures 8E, 12A, 12C); all four P-XDs within a P tetramer function independently of each other; bioactivity requires XD binding to L and MoRE; both wild type and mutant XDs are equally MoRE binding competent (Figure 8B); the V463R mutation selectively impairs XD interaction with L only; and a single L binding-competent XD in the P tetramer is necessary and sufficient for bioactivity of the RdRP complex (Figures 12B-3 and 12D-1).

Data fitting: Experimental measurements of relative RdRP bioactivities were fitted to the above models using lsqcurvefit, a nonlinear regression model in Optimication Toolbox of MATLAB R2017a (MathWorks). Goodness of fit was calculated using R^2 values, defined as the proportion of the variance in the dependent variable that is predicable from the independent variables. Activity data sets for P $(361\text{-}364)_{Ala}$ and P-V463R were assigned a default bioactivity data point A = 1 when ρ = 0.

Statistical analyses: One or two-way ANOVA with Tukey's post-hoc multiple comparisons tests or T-tests were used to assess statistical difference between samples, in all cases using the Prism 8 software package (Graph Pad). The nature of individual statistical tests applied is specified in each Figure legend, p value-intervals are shown. Wherever possible,

graphical representations of experimental results show both the means of all biological replicates ± standard deviations (SDs) and individual biological repeats. All experiments were carried out in at least three biological repeats.

1.2.7 Chapter 1 Results

To dissect the contribution of individual MeV PCT domains to L binding, we first focused on OD. In MeV P expression plasmids, we either deleted this domain by removing residues 303-360 (OD structure up to residue 360 was resolved in [110]) or replaced this section up to residue 360 or 377 (end of defined heptad repeat motif), respectively, with the tetrameric mutant of the yeast general control protein 4 (GCN4) coiled-coil [111] (**Figure 5B**). The effect of these modifications on the physical interaction of P with L was assessed through co-immunoprecipitation (co-IP) of the proteins from the lysates of transiently transfected cells. All co-IPs were carried out with a C-terminally truncated form of L, L_{1708} lacking the L methyltransferase domain, that we have previously shown to be fully folding competent and capable of forming bioactive polymerase complexes when post-translationally combined with the corresponding C-terminal L fragment [80]. Co-IP efficiencies of L_{1708} or full-length L with P are indistinguishable (**Figure 6**), but L_{1708} facilitates biochemical analysis of P-to-L binding due to a lower tendency to self-aggregate spontaneously [74].

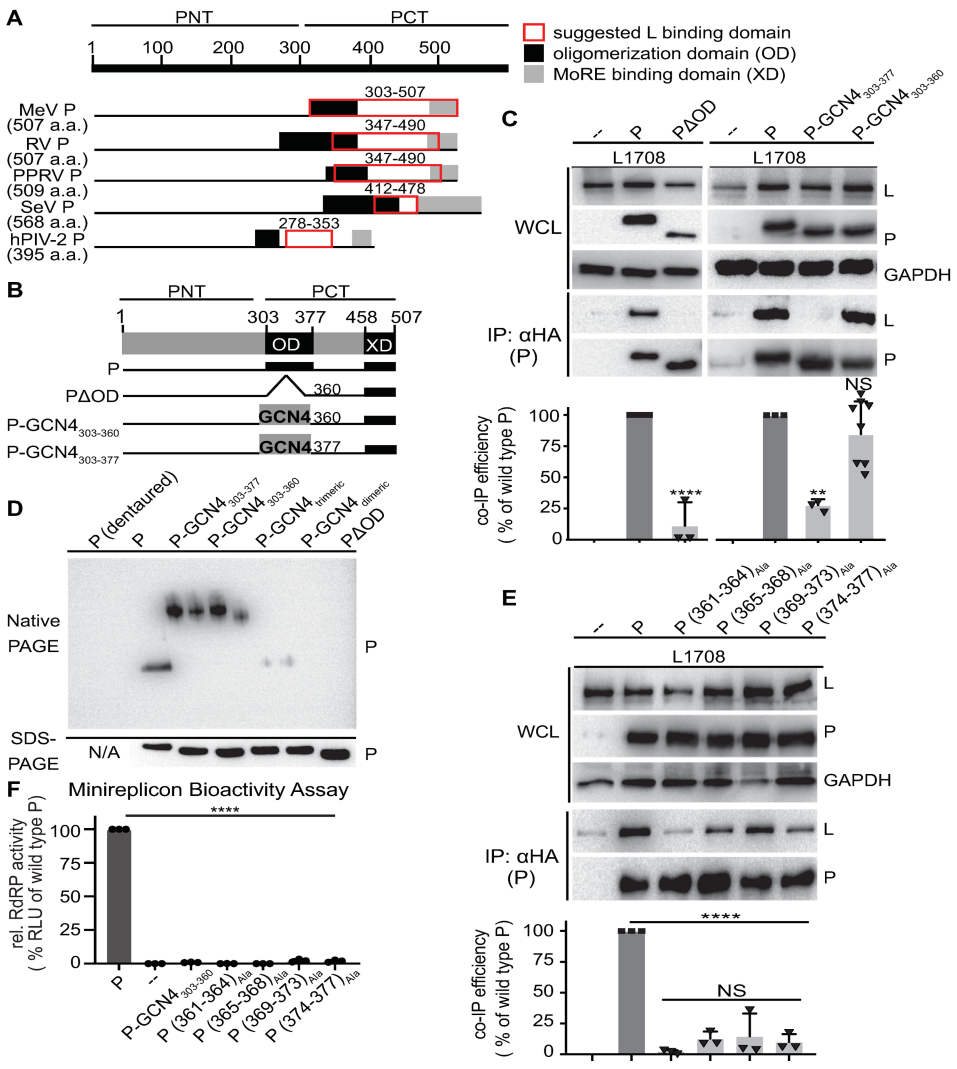

Figure 5. *P OD C-terminal microdomain is required for P-to-L binding* ***A)*** *Overview of proposed L binding domains on P for different Paramyxoviridae. Numbering refers to MeV P.* ***B)*** *Schematic representation of P with OD deletion or exchange with yeast GCN4.* ***C)*** *Immunoblots of whole cell lysates (WCL) and immunoprecipitates (IP) after co-transfection with L_{1708} (L) and P variants shown in (B). P was detected with anti-HA antibodies, L with anti-FLAG antibodies. GAPDH served as loading control. Graph shows relative co-IP efficiency of L with P; columns are means ± SD, symbols show individual biological repeats (n = 3).* ***D)*** *Native PAGE analysis of P constructs shown in (B). Trimeric and dimeric variants of yeast GCN4 (P-$GCN4_{Trimeric}$ and P-$GCN4_{Dimeric}$, respectively) were included for mobility reference. SDS-PAGE shows immunoblots of the identical samples after denaturation and reduction.* ***E)*** *P-L co-IP of alanine scanning mutagenesis of the P (361-377) microdomain.* ***F)*** *Monocistronic minireplicon assay performed in the presence of wild type P or P mutants specified. Columns are means ± SD, symbols show individual biological repeats (n = 3). All statistical analyses through one-way ANOVA with Tukey's post hoc multiple comparison test. (NS, not significant; **, $p \leq 0.01$; ****: $p \leq 0.0001$).*

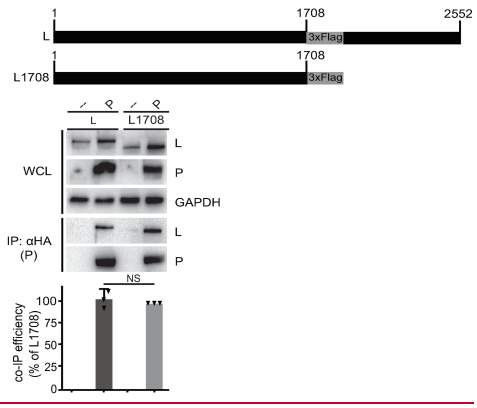

Figure 6. *Full-length L and truncated L1708 interact with P with equal efficiency. Cartoons provide a schematic overview of the L constructs. Numbers refer to amino acids. Immunoblots of input and co-precipitated material assessing P interaction with full-length and truncated L. Detection and quantitative analysis as in Figure 1C. Columns show means ± SD, symbols represent individual biological repeats (n = 3). Statistical analysis through unpaired T-test (NS, not significant).*

1.2.7.1 MeV P residues proximal to the structurally defined OD are critical for L interaction

When subjected to this assay, the PΔOD mutant lacking the oligomerization domain was unable to co-precipitate L (**Figure 5C**). In contrast, efficient wild type P-equivalent L binding was maintained when P OD up to residue 360 was replaced with yeast GCN4 (P-GCN4$_{303\text{-}360}$). Further extension of the GCN4-substituted area up to P residue 377 eliminated any appreciable interaction with L. Native-PAGE analysis confirmed that both GCN4-substituted P mutants tetramerized efficiently, whereas PΔOD predictably remained monomeric (**Figure 5D**). In contrast to previous theories [86, 92, 99], residues in the MeV P OD core do not, therefore, form a physical interface with L but contribute to the interaction only indirectly through the initiation of mandatory P tetramerization. However, residues in the short stretch at the OD C-terminus from position 361 to 377 are candidates for direct L binding.

Alanine-scanning mutagenesis of the 361-377 microdomain revealed that all sub-sections tested are required for efficient L binding (**Figure 5E**). Although reductions in L co-IP efficiency

were statistically equivalent, we noted the lowest relative interaction with L when P residues 361-364 were substituted with alanines, creating P $(361\text{-}364)_{Ala}$. Employing a mono-cistronic firefly luciferase MeV minireplicon reporter system that we have previously described [73], we assessed bioactivity of the different alanine mutants after co-expression with unmodified, homotypic MeV N and L proteins. Consistent with impaired physical interaction of these P mutants with L, all four constructs abolished RdRP bioactivity (**Figure 5F**). Despite its unaltered physical interaction with L, P-$GCN4_{303\text{-}360}$ also lacked bioactivity in minireplicon assays, indicating that the P OD has a role in viral RdRP activity distinct from L binding and mediating P tetramerization.

1.2.7.2 Substitutions in the P OD C-terminal microdomain are dominant-negative to RdRP bioactivity

Residues in the P OD section 361-377 follow a 3-4 heptad repeat pattern that is characteristic for α-helical coiled-coils and conserved across pathogens of the morbillivirus genus (**Figure 7A**). To increase resolution of the alanine scan, we followed up with pairwise and individual substitutions in the 361-364 microdomain that had shown the strongest disruption of co-IP efficiency. This biochemical assessment demonstrated that disruption of P interaction with L was equally carried by residues 363 and 364, although the quadruple substitution still returned the most robust effect on average (**Figure 7B**). Independent of residual L binding capacity, all single and tandem substitutions except S361A eliminated RdRP bioactivity in minireplicon assays (**Figure 7C**).

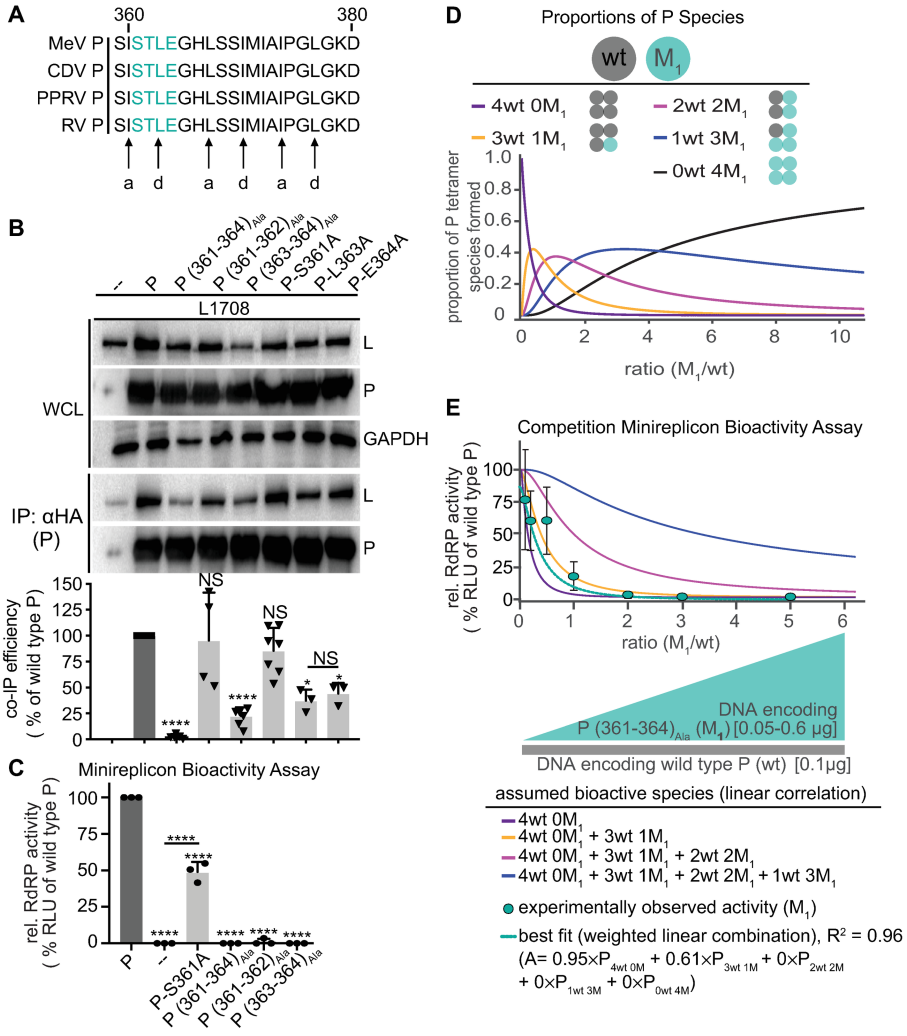

***Figure** 7. P (361-364)Ala acts on RdRP bioactivity in a dominant-negative manner **A)** Alignment of P residues 361-377 of selected morbilliviruses. Predicted a and d positions of heptad repeat motif are highlighted. **B)** P:L interaction analysis of P mutants with alanine substitutions at positions 361-364. Detection and quantitative analysis as in Figure 1C ($n \geq 3$). **C)** Minireplicon assay with P alanine substitutions at positions 361-344 ($n = 3$). **D)** Schematic of mixed P tetramer species present after co-expression of P (361-364)$_{Ala}$ (M_1) and wild type P (wt). Equations specify the probability of formation for each tetramer species, and the graph shows the relative proportion of these species in co-transfected cells as a function of wild type and mutant input plasmid ratio, graphically represented below the x-axis. **E)** Observed RdRP activity in minireplicon assays in the presence of different P (361-364)$_{Ala}$ and wt P ratios as depicted in (D). Symbols show means of experimentally observed biological repeats ± SD ($n = 3$). Solid lines represent activity curve predictions according to a linear combination model and the relative distributions of the P tetramer species shown in (D). The dotted line (red) represents the best fit curve of the experimental data with weight assignments specified in the equation (A, relative RdRP activity), goodness of fit (R^2) is indicated. All statistical analyses and symbols as detailed in Figure 5.*

Structural analysis has revealed that some helices of the P-OD coiled-coil extend to residue 373 [86]. Combined with an intact heptad repeat pattern up to residue 377, assembly of the entire 361-377 stretch into an extended coiled-coil and interaction with L as a tetrameric assembly appears likely. To test whether the P $(361\text{-}364)_{Ala}$ substitution has a cooperative effect on P tetramer activity, we generated competition profiles of mixed P tetramers by gradually increasing the relative amount of mutant P in minireplicon assays in the presence of a constant, low level of wild type P. Under these conditions, five distinct P tetramer species will form in all co-transfected cells, with the relative species distribution determined by the input ratio of mutant and wild type P-encoding plasmid DNA (**Figure 7D**), since native-PAGE analysis confirmed that the 361-364 alanine substitution did not affect the ability of P to tetramerize (**Figure 8**). Minireplicon-based assessment of RdRP bioactivity in the different cell populations revealed a steep decline in minireplicon expression in the presence of increasing amounts of the P $(361\text{-}364)_{Ala}$ mutant (**Figure 7E**). This decline was not simply due to increasingly unfavorable ratios of P- versus N- and L-encoding plasmid transfected. When we generated P plasmid concentration-activity profiles, relative activities followed an optimum curve, but activity differences were statistically not-significant over the plasmid ratio range explored in the minigenome competition profile (**Figure 9**).

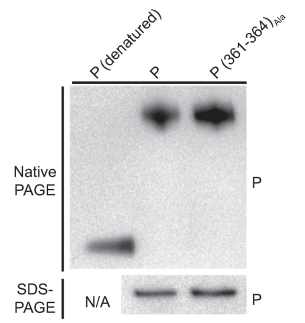

Figure 8. *Native PAGE analysis of P (361-364)Ala and respectively denatured and native wild type P. SDS-PAGE shows immunoblots of the identical samples after denaturation and reduction.*

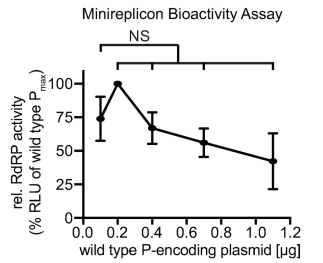

Figure 9. *RdRP minireplicon activity profile describing the effect of different relative amounts of wild type P-encoding plasmid DNA transfected. Amounts of plasmids encoding L and N were kept constant. Symbols show means of experimentally observed biological repeats ± SD (n = 3). Statistical analyses through one-way ANOVA with Dunnett's multiple comparison test, relative to starting conditions (0.1 µg); (NS, not significant).*

We tested a series of mathematical models for the best description of the experimental competition data. Assigning all mutant and wild type P proteins co-expressed in the same cell equal probability to tetramerize, we considered the mutant occupation of one P monomer to be independent of the other three monomers. Goodness of fit was excellent ($R^2 = 0.96$) for a linear combination model in which only tetramers consisting of four wild type (4×wt) or three wild type and one mutant (3×wt/1×P $(361\text{-}364)_{Ala}$) P monomers contribute to RdRP bioactivity, while all other P tetramer species are biologically inactive (**Figure 7E**). These results indicate that at

most one P $(361\text{-}364)_{Ala}$ monomer can be present in a partially bioactive P tetramer, revealed a dominant-negative effect of the P $(361\text{-}364)_{Ala}$ mutation that we consider to be due to interference with coiled-coil extension.

1.2.7.3 P-XD is an essential contributor to efficient P interaction with L

The C-terminal 50 residues of P form the XD, which has been shown biochemically and crystallographically to mediate binding of the polymerase complex to the RNP through interaction with the MoREs located near the end of each N-tail [96, 98, 112]. To confirm that P-XD has a direct role in L binding, we generated a series of mutants with C-terminal truncations of gradually increasing length (**Figure 10A**). Co-IP analyses identified an essential function of P-XD in mediating efficient interaction with L (**Figure 10B**), since even partial shortening of P-XD was sufficient to cause significant reduction in co-IP efficiency and larger truncations abolished all appreciable interaction between P and L. Consistent with a dual role of P-XD in both MoRE and L binding, all C-terminal P truncation mutants lacked bioactivity in minireplicon assays (**Figure 11**). When we co-expressed isolated P-XDs – either in the form of individual polypeptides or as fusion proteins with GST for stabilization – with L, however, no biochemical interaction could be detected (**Figure 10C**). We conclude that P-XD is an essential contributor to efficient P-to-L binding. Unlike the strong interaction of P-XD with MoRE affording efficient co-immunoprecipitation [106], the affinity of isolated P-XD polypeptides for L is low, suggesting that isolated P-XDs are folding compromised, or P-XD does not share a direct interface with L.

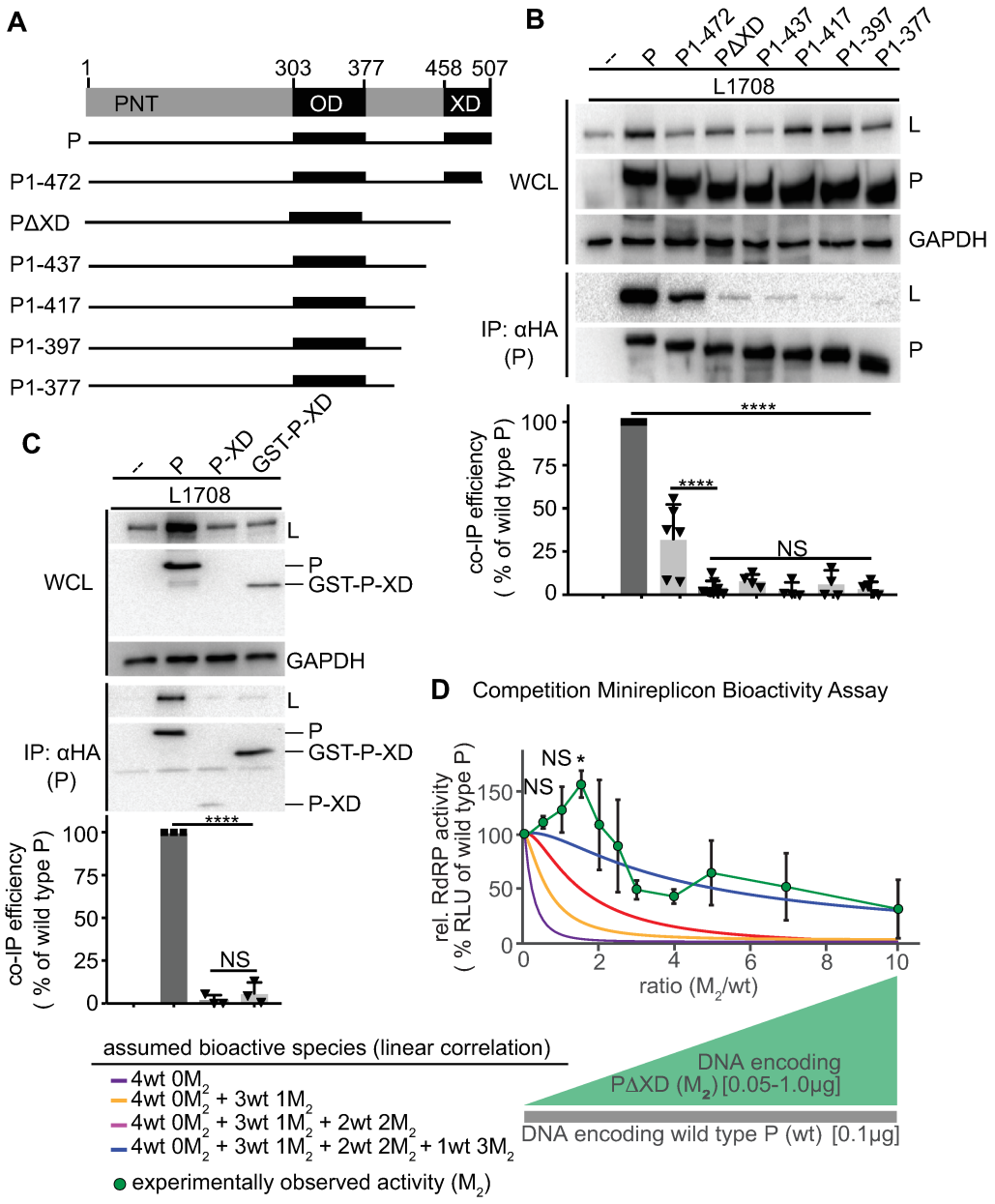

Figure 10. *P-XD is essential for efficient P:L interaction, but P-XD deletion mutants lack cooperative negative impact on RdRP activity* ***.*** ***A)*** *Schematic of P mutants generated with C-terminal truncations.* ***B, C)*** *P:L interaction analysis of P mutants shown in (A) and P-XD expressed in isolation (P-XD) or as a GST fusion protein (GST-P-XD). Detection and quantitative analysis as in Figure 1C (n ≥4 (B) and n = 3 (C)).* ***D)*** *Observed RdRP activity in minireplicon assays in the presence of different PΔXD (M_2) and wt P ratios as graphically depicted below the graph. Symbols with connecting line represent means of experimentally observed biological repeats ± SD (n = 3). Solid lines represent activity curve predictions according to a linear combination model as in Figure 2E. All statistical analyses and symbols as detailed in Figure 1 (*, $p \leq 0.05$).*

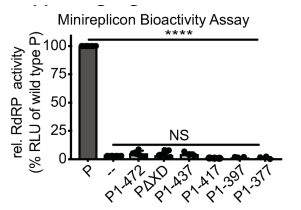

Figure 11. *Minireplicon analysis of bioactivity of the C-terminally truncated P mutants depicted in Figure 3A. Columns represent mean relative RdRP activities, symbols show individual biological repeats ± SD (n = 3). Statistical analyses through one-way ANOVA and Tukey's multiple comparison test (NS, not significant; ****, $p \leq 0.0001$).*

To explore the minimal stoichiometry of intact XDs per P tetramer that is required for bioactivity, we again co-expressed increasing relative amounts of the PΔXD mutant with wild type P in minireplicon competition assays. The resulting activity profile was notably distinct from that obtained with the P $(361\text{-}364)_{Ala}$ substitution (**Figure 10D**). Even at the highest relative ratios (up to 10) of the PΔXD mutant, RdRP activity remained significantly higher than background, indicating that PΔXD has no dominant-negative effect, and lower relative ratios of the PΔXD unexpectedly resulted in a significant boost in RdRP activity compared to that observed in the presence of wild type P only.

Modeling attempts revealed that these data could not be described with a weighted linear combination function. We, therefore, explored several non-linear models, but the complex biology of P-XD prevented a satisfying mathematical representation of the experimental results without overfitting the data set. While our results thus reveal that partially reducing the number of L and MoRE binding-competent XDs within a P tetramer boosts overall RdRP bioactivity, meaningful mathematical modeling of the phenotype requires a better-targeted approach than removal of P-XD entirely. We, therefore, explored the mapping of the P-XD interface contacting L.

1.2.7.4 Distinct faces of the P-XD triangular prism mediate binding to MoRE and L

In co-crystals with MoRE, MeV P-XD assumed a helix-turn-helix fold of three α-helices approximately arranged as a triangular prism (**Figure 12A**). One side of this prism forms the interface with MoRE. To map individual residues mediating P-XD interaction with L, we targeted amino acids located at the surface of the other two sides of the prism through charge-reversal or charge-introducing substitutions, respectively. All of the resulting mutants were expressed efficiently (**Figures 12B and C**). Substitutions in the prism face between P-XD helices α1 and α2 did not affect L binding (Figure 12B), but three residues located in the face between α1 and α3 (V463 and S466 on α1, and H498 on α3) either abolished, or significantly reduced, P interaction with L **(Figure 12C)**. Together these residues form a continuous microdomain covering the lower quadrant of the α1/α3 P-XD prism surface (**Figure 12A**). To test whether the absence of the C-terminal methyltransferase domain in the L_{1708} fragment impacted co-IP results, we re-examined two P mutations abolishing interaction, $P\ (361\text{-}364)_{Ala}$ and P-V463R, against full-length L. Neither P mutant precipitated L efficiently, validating the L_{1708}-based results **(figure 13)**.

We next asked whether the P-V463R substitution in α1 that caused the strongest reduction in co-IP efficiency specifically impairs P-to-L binding or globally alters the P-XD conformation. To address this question, we examined its impact on the P-XD interaction with MoRE. Since N-terminal residues of P directly bind to Ncore [56], we generated and employed P C-terminal fragments (PCTs) starting upstream of the tetramerization domain at P residue 231 for this analysis. Co-IPs of wild type PCT and the PCT-V463R mutant with standard N revealed efficient binding, indicating that this mutation in the α1/α3 prism face does not affect interaction with MoRE and thus suggesting that global P-XD folding is intact (**Figure 12D**). The assay was

validated through F497D or D493K substitutions, which are located in the hydrophobic core of P-XD between α2 and α3 [66] or predicted to reside on the surface of the MoRE-binding face of P-XD, respectively, and each indeed destroyed the interaction (**Figure 12D**).

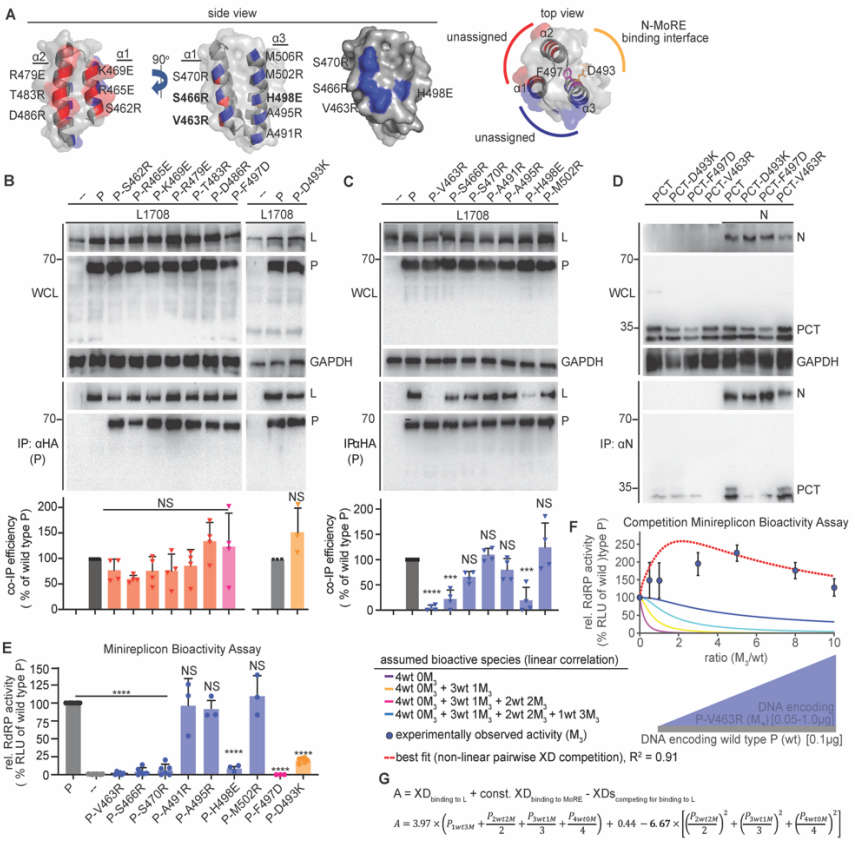

Figure 12. *Identification of a specific L-binding face of the triangular prism fold of P-XD with regulatory effect on RdRP bioactivity* ***A)*** *Structural representations of MeV P-XD (PDB: 1T6O; only the P-XD component is represented), shown in side and top views. Areas between helices α1/α2 (red) and α1/α3 (blue) form faces of the prism without known interaction partners or bioactivities. Specific residues on each face are specified. Top view shows the known MoRE-binding face of P-XD between helices α2/α3 (yellow), residues confirmed (F497) or predicted (D493) to respectively impair P-XD fold or MoRE binding when mutated are highlighted. Grey background represents space-fill surface model.* ***B, C)*** *P:L interaction analysis of P mutants with individual substitutions of residues specified in (A), forming the "red" and "blue" prism surfaces or implicated in MoRE binding (yellow). Detection and quantitative analysis as in Figure 1C (n = 4 (B); n = 3 (C)).* ***D)*** *PCT:N interaction after mutation of residue D493 on the MoRE interaction face of P-XD. Anti-N antibodies were used for IPs and anti-HA to detect PCT variants.* ***E)*** *Minireplicon analysis of RdRP activity in the presence of the specified P mutants. Columns represent means of experimentally observed values ± SD, symbols show individual biological repeats (n ≥ 3).* ***F)*** *Observed RdRP activity in minireplicon assays in the presence of different P-V463R (M_3) and wt P ratios as graphically depicted below the graph. Symbols show means of experimentally observed biological repeats ± SD (n = 3). Solid lines represent activity curve predictions according to a linear combination model as in Figure 2E. The dotted line (red) represents the best fit curve of the experimental data based on a non-linear pairwise P-XD competition model, goodness of fit (R^2) is indicated.* ***G)*** *Mathematical description of the model represented in (E). P-XD bioactivities considered and the corresponding weight assignments are specified. All statistical analyses and symbols as detailed in Figure 1 (***, $p \leq 0.001$).*

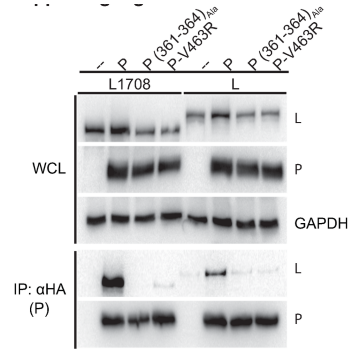

Figure 13. *Effect of P (361-364)Ala and P-V463R mutations on P binding to full-length L. Interaction analysis was carried out as specified in Figure 5C, using equally Flag epitope-tagged L1708 and full-length L as co-IP targets.*

Bioactivity testing of all P-XD mutants in minireplicon assays demonstrated a direct correlation between the effect of substitutions in the α1/α3 P-XD prism face on L binding and RdRP bioactivity (**Figure 12E**). α1 substitutions V463R and S466R and the α3 mutation H498R in particular eliminated all polymerase activity, as did the F497D and D493K changes suppressing P-XD binding to MoRE. Competition profiles of the P-V463R mutant with wild type P revealed remarkable RdRP hyper-activity at higher relative amounts of the V463R mutant, more than double that seen in the presence of wild type P alone (**Figure 12F**). Also, this experimental data set was incompatible with a linear combination function.

We, therefore, considered again non-linear models, based on the following assumptions: all four P-XDs within a P tetramer function independently of each other; bioactivity requires XD binding to L and MoRE; both wild type and mutant XDs are equally MoRE binding competent; and the V463R mutation selectively impairs XD interaction with L only. Most notably, the best fit ($R^2 = 0.80$) mathematical description of the experimental data critically depends on the addition of a strong negative effect on bioactivity that arises from P-XD competition for L binding (**Figure 12G**). This model assumes that a single L binding-competent XD in the P

tetramer is necessary and sufficient for bioactivity of the RdRP complex. Corroborating RdRP hyperactivity seen in the earlier PΔXD competition profiles, these results for the MoRE binding-competent but L binding-defective P-V463R mutant revealed that assignment of L-binding competence to only one XD per P tetramer creates conditions most favorable for overall RdRP activity.

1.2.7.5 Trans-complementation of P mutants with distinct L binding deficiencies in minireplicon and recMeV

Having identified two discrete P microdomains that are required for interaction with L and highly conserved across major human pathogens in the paramyxovirus family (**Figure 14**), we explored whether these domains are functionally distinct. Co-expression of P $(361\text{-}364)_{Ala}$ and P-V463R, each by itself unable to co-IP L, restored physical interaction with L (**Figure 15A**). Wild type P-like binding efficiency was observed in the presence of the highest relative excess of P-V463R tested. When applied to minireplicon assays, we found that successful trans-complementation of L binding capacity extended to bioactivity of mixed P tetramers, remarkably resulting in RdRP activity equivalent to that observed with wild type P when cells received P $(361\text{-}364)_{Ala}$ and P-V463R-encoding plasmid DNA in approximately a 1:3-relative ratio (**Figure 15B**). Trans-complementation profiles over a wide plasmid ratio range corroborated this result, revealing a steep, asymmetric bell curve with a wild type P-equivalent RdRP bioactivity peak at a relative plasmid DNA ratio of 1:3 (P $(361\text{-}364)_{Ala}$:P-V463R) (**Figure 15C**). We conclude that at least two structurally and functionally distinct P microdomains are engaged in productive P-to-L binding. Wild type P-like bioactivity in the presence of an excess of P-V463R in mixed P tetramers corroborates our earlier observation that designating L binding-competence to a single

XD per P tetramer boosts bioactivity, thus compensating for the negative effect associated with the presence of even one P $(361\text{-}364)_{Ala}$ monomer.

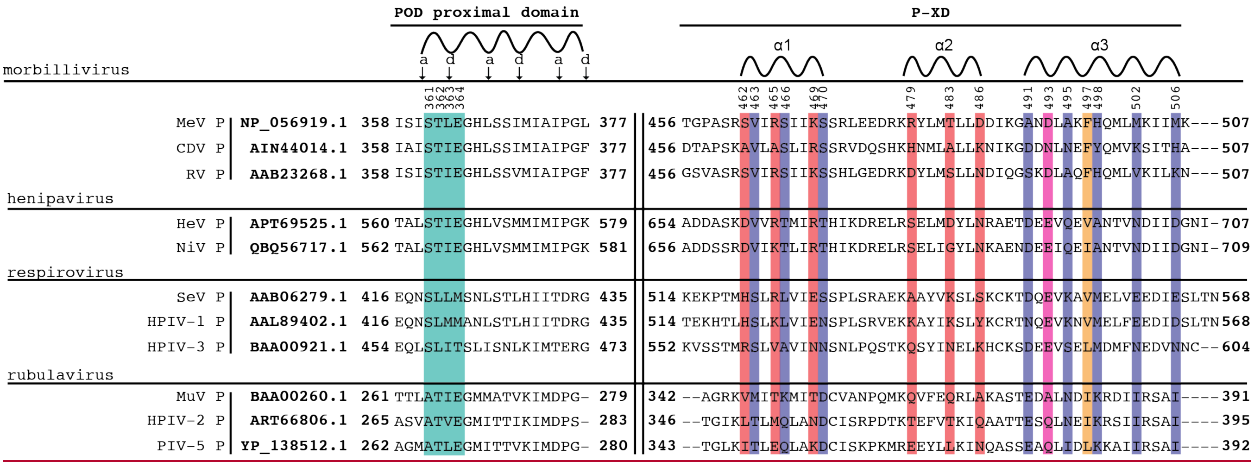

Figure 14. *Multi-sequence alignments of P proteins of selected paramyxoviruses, representing genera of major clinical importance. Alignment with Clustal Omega algorithm (MeV P (NP_056919.1); CDV P (AIN44014.1); RV P (AAB23268.1); hendra virus (HeV) P (APT69525.1); nipah virus (P) P (QBQ56717.1); SeV P (AAB06279.1); HPIV-1 P (AAL89402.1); HPIV-3 P (BAA00921.1); mumps virus (MuV) P (BAA00260.1), HPIV-2 P (ART66806.1), and PIV-5 (YP_138512.1). α-helical regions are highlighted above the sequences and heptad repeats in P-OD indicated; numbering refers to MeV. P residues 361-364 are highlighted in green, color-coding of individual residues in P-XD according to the scheme used in Figure 11A.*

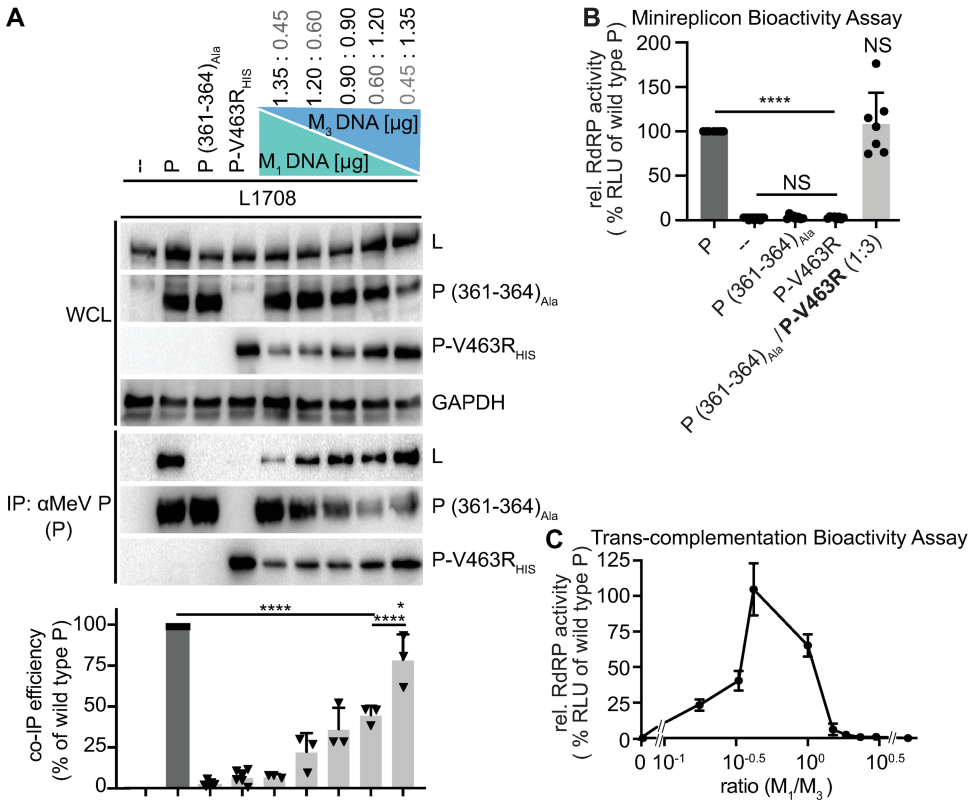

Figure 15. *L-binding null-mutants in P OD C-terminal microdomain and P-XD efficiently trans-complement* ***A)*** *Graphic depiction of P (361-364)$_{Ala}$ / P-V463R trans-complementation ratios tested and P:L interaction analysis of the different trans-complementation pairs. A HIS-tagged version of the P-V463D mutant was used to enable differential immunoprecipitation, detection and quantitative analysis otherwise as in Figure 5C (n ≥ 3).* ***B)*** *Minireplicon assay of candidate trans-complementation P mutants alone and co-expressed at 1:3 relative ratio (n ≥ 3).* ***C)*** *Trans-complementation RdRP activity profile of the pair shown in (A) and (B), analyzed in minireplicon assays over the specified relative ratio range. Error bars show means of biological repeats ± SD (n = 3). All statistical analyses and symbols as detailed in Figure 5.*

Minireplicon assays are highly informative for functional dissection of RdRP activities, but the physiological relevance of the results can be compromised by the shortcoming that only a subset of the multiple RdRP activities required for successful virus replication is examined [71]. To test whether trans-complementation restores the complete functional range of MeV RdRPs, we engineered a recMeV genome in which the wild type P gene was replaced with a tandem

arrangement of genes encoding P-V463R and P $(361\text{-}364)_{Ala}$, respectively (**Figure 16A**). P-V463R was intentionally placed upstream of P $(361\text{-}364)_{Ala}$ to capitalize on the *Mononegavirales* transcription gradient [113] and ensure that L binding-deficient P-V463R would be present in relative abundance over P $(361\text{-}364)_{Ala}$ in infected cells. The corresponding recMeV P-V463R-P $(361\text{-}364)_{Ala}$ virus was recovered successfully, replicated as efficiently as the genetic parent virus (**Figure 16B**) and displayed equivalent cytopathic effect (CPE) size (**Figure 15C**) and CPE kinetics (**Figure 16D**) in cell culture. Sanger sequencing of both P genes after five consecutive passages of four independently recovered recombinants confirmed the integrity and genetic stability of both P mutations in replicating virus (**Figure 16E**). Like all paramyxovirus RdRPs, MeV polymerase is error-prone, and mutations advantageous for viral fitness become genetically fixed rapidly [114]. The clean chromatograms at both mutation sites in all recMeV examined indicate a remarkable lack of selective pressure to acquire revertant or compensatory mutations. This observation was consistent with the parent recMeV-like growth profiles of the double mutant virus and underscores that all P bioactivities required for unimpaired virus replication are restored through trans-complementation.

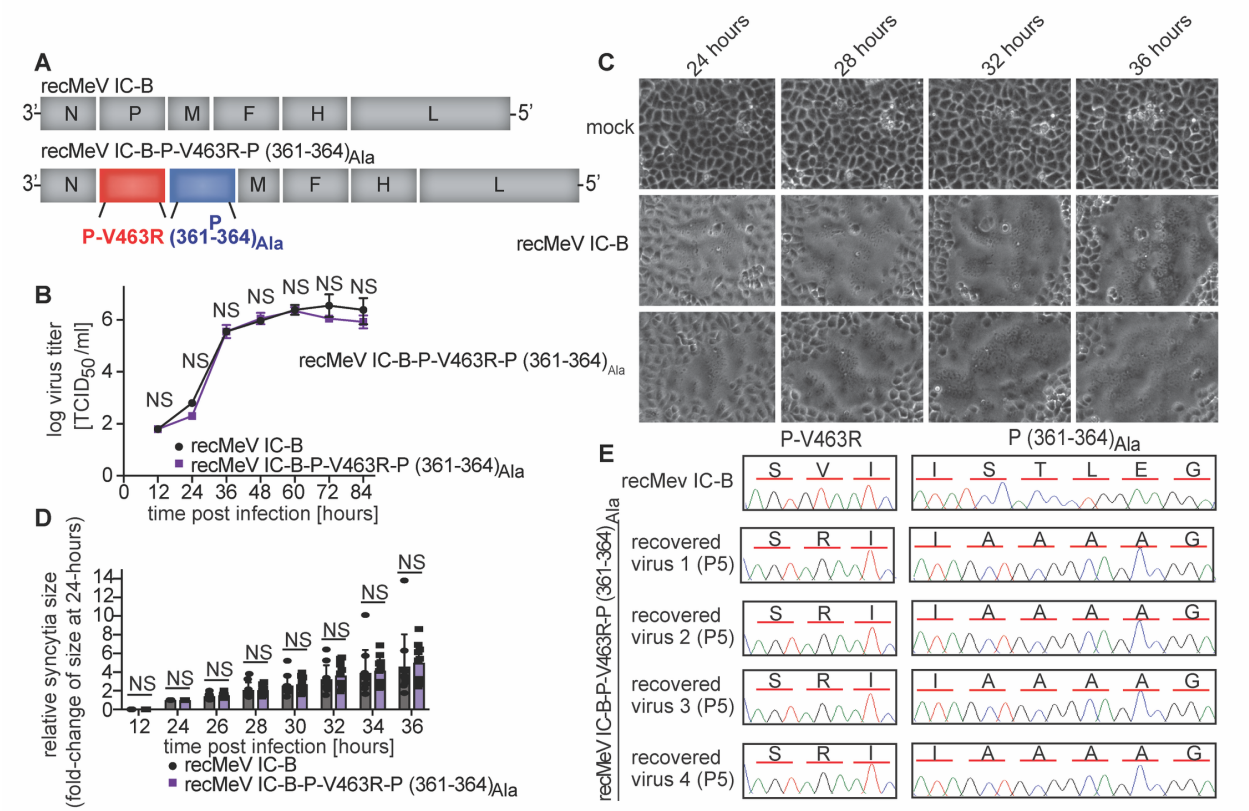

Figure 16. A) *Graphic genome representations of standard MeV (strain IC-B) and trans-complementation candidate. The relative positions of the P-V463R (red) and P (361-364)$_{Ala}$ (blue) genes are highlighted.* ***B)*** *Viral growth curves after recovery of parent recMeV IC-B and trans-complemented recMeV IC-B P-V463R-P (361-364)$_{Ala}$. Symbols represent mean titers of biological repeats ± SD (n = 3). Statistical analysis through two-way ANOVA with Sidak's post-hoc comparison tests.* ***C)*** *Microphotograph time-courses of uninfected Vero-hSLAM cells (mock) or cells infected with recMeV IC-B or recMeV IC-B P-V463R-P (361-364)$_{Ala}$, taken in 4-hour intervals from 24-36 hours after infection. Each series shows a specific area, monitored over time.* ***D)*** *Quantitation of CPE kinetics after infection of cells with standard and trans-complemented recMeV. Syncytia sizes in 10 distinct areas/virus were quantitated automatically using a high-content imager, and are each expressed as fold-change increase in syncytia size (in μm^2 area covered) relative to syncytia size at the same plate coordinates at 24 hours pI. Columns represent means of experimentally observed values ± SD, symbols show individual repeats (n = 10); NS not significant.* ***E)*** *Chromatograms of P sequences at mutated areas of recovered recMeV IC-B and recMeV IC-B P-V463R-P (361-364)$_{Ala}$ after five serial passages on Vero-hSLAM cells. Encoded amino acids are specified above the chromatograms.*

1.2.7.6 OD proximal and connector region residues reside in the same functional group

To scan the approximately 80-residue connector region between the P OD C-terminus and P-XD for amino acids potentially contributing to L binding, we explored heterotypic interactions

between MeV and very closely related CDV P and L. Both viruses share considerable protein sequence homology and identity, and heterotypic co-IPs confirmed that MeV P associates with MeV or CDV L with equal efficiency (**Figure 17**). Heterotypic interaction suggests that any residue in the connector region contributing to P-to-L binding should be conserved between both viruses. We identified nine distinct microdomains of three to four consecutive identical amino acids in sequence alignments of the MeV and CDV P connector regions (**Figure 18A**) and subjected each individually to alanine scanning mutagenesis.

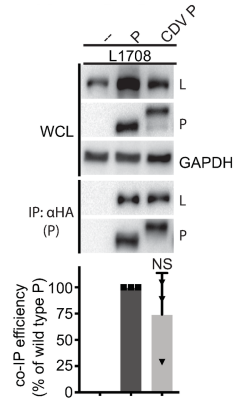

Figure 17. *Homo- and hetero-typic interaction of MeV L with P derived from MeV or CDV, respectively. Interaction analysis, immuno-detection and signal quantitation in Figure 5C. Columns show means ± SD, symbols represent individual biological repeats (n = 3). Statistical analysis through unpaired T-test (NS, not significant).*

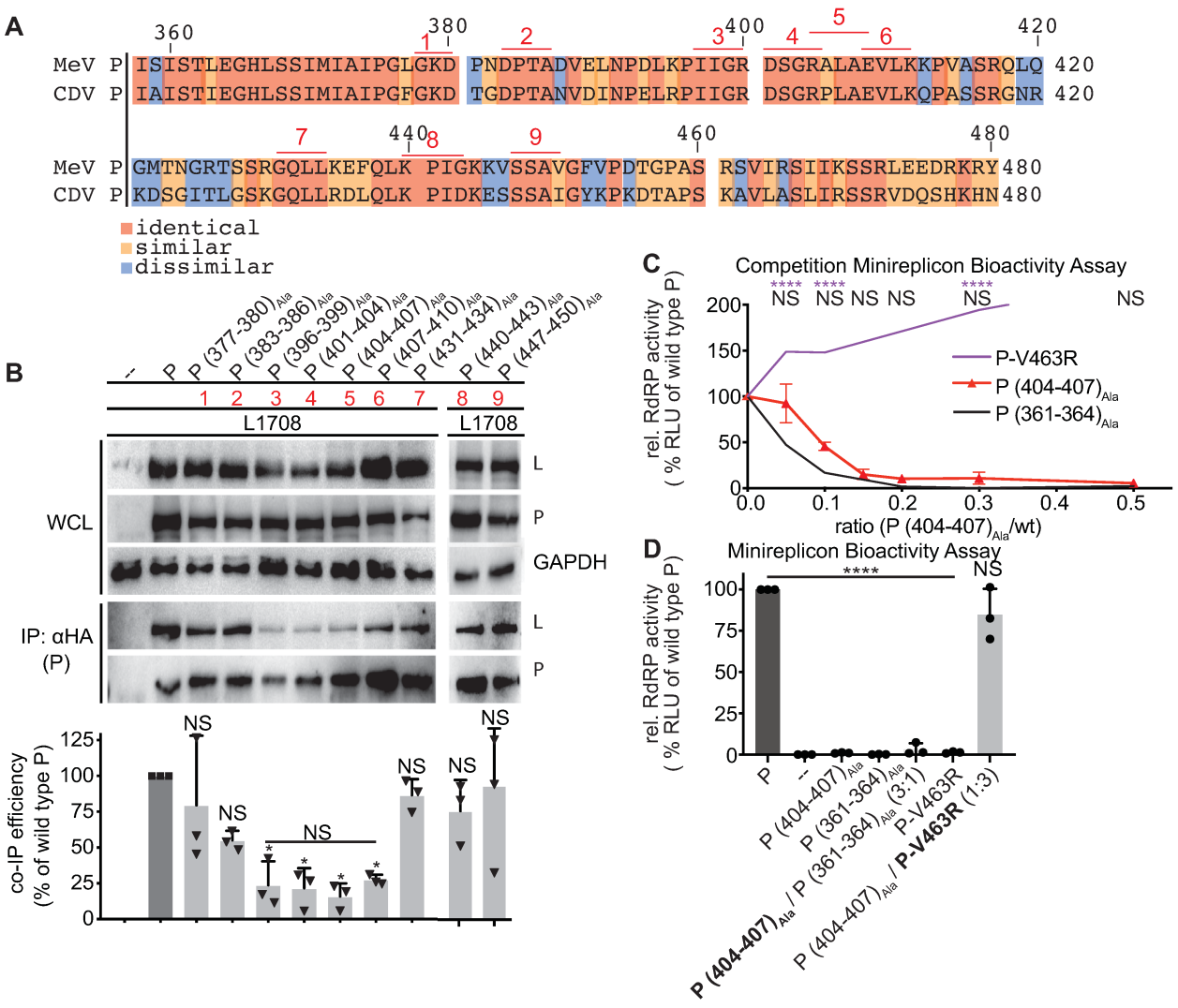

Figure 18. *Residues in the connector region between P position 377 and 458 trans-complement P-XD mutations but are functionally linked to the OD C-terminal microdomain* ***A)*** *Alignment of MeV and CDV P sequences between residues 351 and 490. Conserved patches (≥3 identical residues) are underlined and numbered consecutively.* ***B)*** *P:L interaction analysis of P mutants with alanine substitutions of residues in conserved patches identified in (A; red numbers). Detection and quantitative analysis as in Figure 5C (n = 3).* ***C)*** *Minireplicon competition experiment between P (404-407)$_{Ala}$ and wt P, set-up as in Figure 2D and E. Symbols show means of relative RdRP activity ± SD, three biological repeats. Blue and black lines show competition profiles respectively between P-V463R (Figure 12G) and P (361-364)$_{Ala}$ (Figure 7E). Statistical analysis with two-way ANOVA and Sidak's post-hoc multiple comparison test.* ***D)*** *Trans-complementation minireplicon assays of P (404-407)$_{Ala}$ with P (361-364)$_{Ala}$ and P-V463R, respectively, relative ratios of P-encoding plasmid DNA transfected as specified. Columns represent mean relative RdRP activities ± SD, symbols show biological repeats (n = 3). Statistical analyses in (B) and (D) and symbols as in Figure 5.*

Co-IPs with the resulting MeV P mutants highlighted a stretch of four consecutive conserved patches in the connector domain, spanning P residue 396 to 410, that significantly impaired P-to-L interaction when mutated (**Figure 18B**). A local co-precipitation minimum was reached by the P $(404\text{-}407)_{Ala}$ mutant. However, all mutants tested with alanine substitutions in the connector domain, including those capable of physical interaction with L, significantly reduced P bioactivity in minireplicon assays (Supporting Figure S8). When increasing amounts of P $(404\text{-}407)_{Ala}$ were co-transfected with wild type P in minireplicon competition assays, bioactivity profiles markedly differed from those of the P-XD mutants but closely resembled the dominant-negative P $(361\text{-}364)_{Ala}$ (**Figure 6C**). Trans-complementation of P $(404\text{-}407)_{Ala}$ was likewise successful with P-V463R but not with P $(361\text{-}364)_{Ala}$ (**Figure 12D**), placing the P OD C-terminal residues and connector region in the same complementation group, each functionally distinct from the L binding face of P-XD.

Co-IPs with the resulting MeV P mutants highlighted a stretch of four consecutive conserved patches in the connector domain, spanning P residue 396 to 410, that significantly impaired P-to-L interaction when mutated (**Figure 18B**). A local co-precipitation minimum was reached by the P $(404\text{-}407)_{Ala}$ mutant. However, all mutants tested with alanine substitutions in the connector domain, including those capable of physical interaction with L, significantly reduced P bioactivity in minireplicon assays (**Figure 19**). When increasing amounts of P $(404\text{-}407)_{Ala}$ were co-transfected with wild type P in minireplicon competition assays, bioactivity profiles markedly differed from those of the P-XD mutants but closely resembled the dominant-negative P $(361\text{-}364)_{Ala}$ (**Figure 18C**). Trans-complementation of P $(404\text{-}407)_{Ala}$ was likewise successful with P-V463R but not with P $(361\text{-}364)_{Ala}$ (**Figure 18D**), placing the P OD C-terminal

residues and connector region in the same complementation group, each functionally distinct from the L binding face of P-XD.

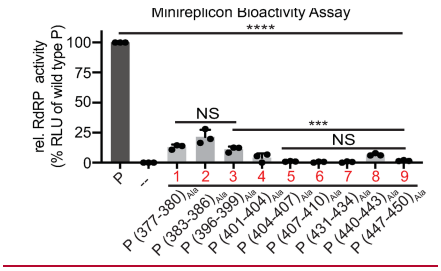

Figure 19. *Minireplicon analysis of relative bioactivity of P mutants with alanine substitutions in conserved patches in the connector domain (specified in Figure 13A; red numbers). Columns show means ± SD, symbols represent individual biological repeats (n = 3). Statistical analysis through one-way ANOVA and Tukey's multiple comparison test (NS, not significant; ***, $p \leq 0.001$; ****, $p \leq 0.0001$).*

1.2.7.7 P-XD is a central regulator of the dynamic interplay between polymerase and encapsidated template

To query whether the same P-XD monomer in a P tetramer must be both L and MoRE binding-competent to support RdRP activity, we examined trans-complementation of the P-D493K mutation abrogating P-XD-to-MoRE binding with P-V463R blocking P-XD-to-L interaction at different relative ratios. Efficient trans-complementation occurred between MoRE-binding impaired (L^+ $MoRE^-$) and L-binding defective (L^- $MoRE^+$) P-XDs (**Figure 20A**). Albeit trans-complementation efficiency was reduced at each of the ratio extremes (1:10 and 10:1, respectively), presumably reflecting an accumulation of a large proportion of bio-inactive homotypic mutant tetramers under these conditions, appreciable RdRP activity remained (**Figure 20B**). We then attempted trans-complementation between P-D493K and P $(361\text{-}364)_{Ala}$. Since our mathematical modeling has demonstrated that at most one P $(361\text{-}364)_{Ala}$ monomer can be present in a bioactive P tetramer, this mutant enabled us to probe the stoichiometric requirements of the different P-XD functionalities. In contrast to our successful earlier trans-complementation

of (L^- $MoRE^+$) P-XDs with P $(361\text{-}364)_{Ala}$, the combination of (L^+ $MoRE^-$) P-XDs with P $(361\text{-}364)_{Ala}$ did not restore RdRP activity. These results indicated that the presence of one MoRE binding-competent or one L binding-competent XD per P tetramer is sufficient for RdRP activity, but these competencies must not reside on the same P-XD if the other three P-XDs are unable to interact with MoRE (**Figure 20B**).

Three-way trans-complementation studies, in which we paired each of the three functional groups tested in all possible combinations reinforced this conclusion, since P-V463R efficiently trans-complemented with a P-D493K - $(361\text{-}364)_{Ala}$ double mutant, while the combination of P-V463R-D493K with P $(361\text{-}364)_{Ala}$ was bio-inactive (**Figure 20C and D**). The presence of only one each L and MoRE binding-competent XD in P tetramers is therefore necessary and sufficient to achieve approximately wild type P-like bioactivity, but both binding partners cannot be simultaneously engaged by the same P-XD monomer. Interaction of a P-XD with L takes priority over MoRE binding when the number of fully functional XDs present in mixed P tetramers is restricted. These data reveal P-XD as a regulatory element of the highly dynamic and multi-faceted protein-protein interplay between RdRP and the RNP template, placing it at the center of a mechanistic model of polymerase advancement.

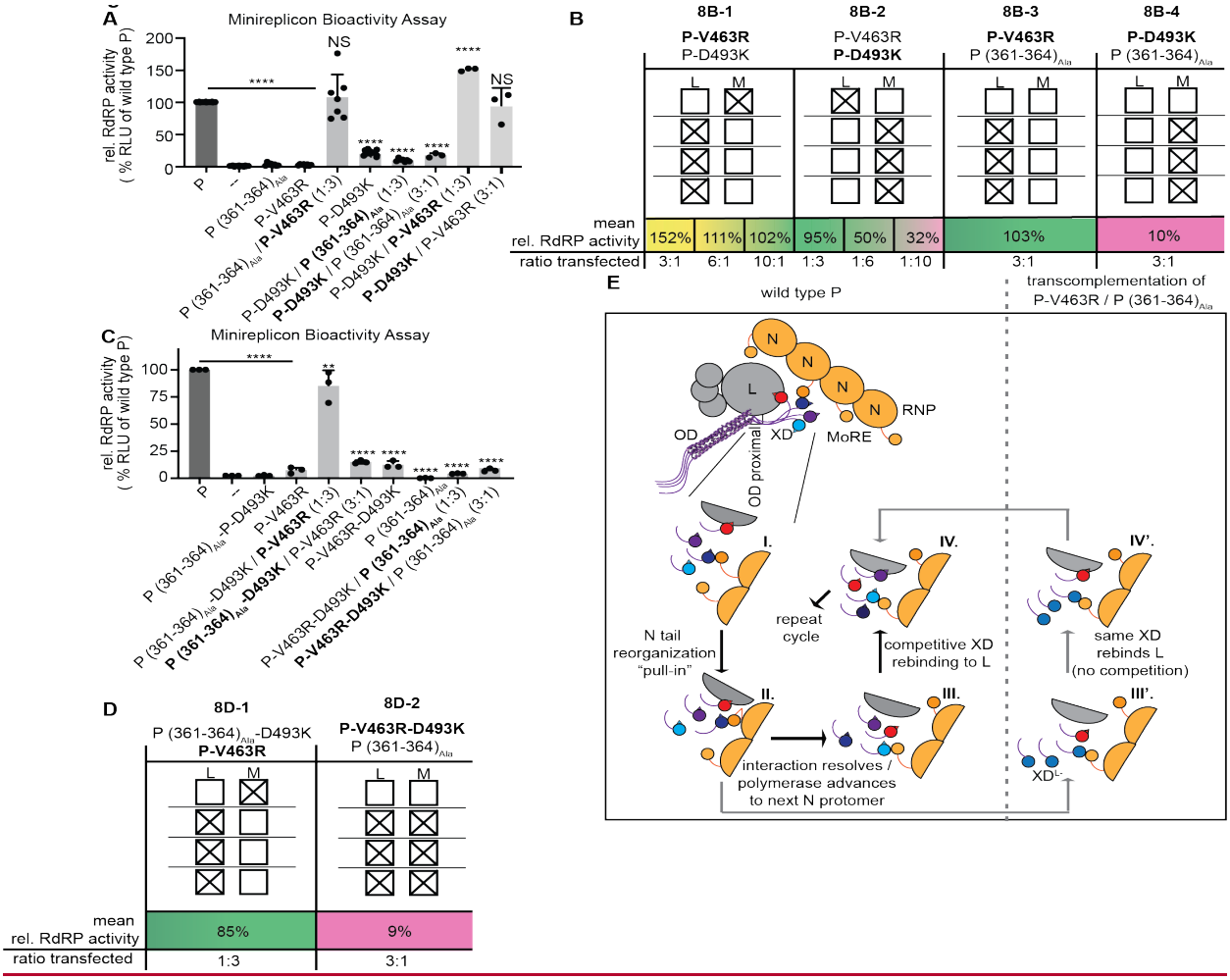

Figure 20. *2-way and 3-way trans-complementations to probe stoichiometric requirements of the different P-XD functionalities in bioactive RdRP complexes* ***A, C)*** *Trans-complementation minireplicon assays of P single and double mutants as specified. Relative ratios of P-encoding plasmid DNA transfected are indicated. Columns represent mean relative RdRP activities, symbols show individual biological repeats ± SD (n ≥ 3). Statistical analyses through one-way ANOVA and Tukey's multiple comparison test, symbols as detailed in Figure 1.* ***B, D)*** *Schematic overview of the predominant P tetramer populations of selected trans-complementation pairs from (A) and (C) as specified. P-encoding plasmid DNA ratios transfected are indicated and mean relative RdRP activities are color-coded (green, wild type P-like activity; yellow, hyper-active; magenta, inactive). Boxes represent dominant XDs composition of trans-complemented mixed P tetramers. Open boxes indicate L (L) or MoRE (M) binding-competence, crossed boxes denote the presence of loss-of-function substitutions for the respective binding activity.* ***E)*** *Mechanistic summary model of P interaction with L and P-XD-mediated regulation of RdRP negotiation of the N-encapsidated template. Individual XDs of the P tetramer are differentiated by color, Ncore and MoREs are shown in gold. Roman numerals in close-up inserts depict specific interactions identified through trans-complementations and are discussed in the text. A model for RdRP activity boosting by the signature trans-complementation pair P-V463R / P (361-364)$_{Ala}$ is shown on the right.*

1.2.8 Chapter 1 Discussion

This study demonstrates that distinct microdomains in MeV P are involved in efficient P hetero-oligomerization with L. We favor the view that these microdomains engage L through direct protein-protein contacts, although more indirect associations involving, for instance, host-derived adapter proteins cannot be excluded. Here, the term P:L interface will be used to refer to both direct and multi-component interactions between the P and L proteins. Based on a combination of biochemical and functional assays, we have pioneered a trans-complementation system to probe the stoichiometric requirements for productive P:L interactions. While trans-complementations were carried out in minireplicon assays, a recombinant MeV carrying a P trans-complementation pair in two tandem open reading frames could be recovered readily, efficiently proliferated with a standard MeV-like growth profile and was genetically stable over multiple passages. The absence of compensatory or reversion mutations, in particular, serves as a compelling indicator that the mutant recMeV does not experience strong selective pressure. These results confirm that trans-complementation restored all RdRP activities required for successful paramyxovirus replication. Thus, assured of the physiological relevance of the strategy, the assay has advanced our mechanistic understanding of how paramyxovirus RdRp negotiates the encapsidated template in four areas:

i) The P:L interface is bipartite. P monomers were unable to interact with L, but replacement of P-OD with yeast GCN4 was tolerated, demonstrating that P tetramerization is essential for L binding. In contrast to previous suggestions [86], however, residues located in the P OD core section are not part of the physical interface. Rather, a 17-residue stretch at the C-terminal end of P OD mediates L binding after extension of the helical coiled-coil up to residue 377. This conclusion is supported by the natural continuation of the heptad repeat patterns of P

OD through to position 377, complete abrogation of the ability of L to co-IP with P after insertion of alanine substitutions in this microdomain, and the dominant-negative competition profile of P $(361\text{-}364)_{Ala}$ with wild-type P. It furthermore is consistent with a very recent study demonstrating that the coiled-coil OD of MeV P is required for viral gene expression [93]. Mathematical description of the experimentally determined data revealed that in the presence of both P $(361\text{-}364)_{Ala}$ and wild type P, only mixed P tetramers harboring precisely one copy of this mutant are bioactive. We have thus shown that three wild type P monomers are able to structurally control one mutant and form proper tertiary assemblies, but two or more P $(361\text{-}364)_{Ala}$ subunits in a P tetramer cannot be contained.

Downstream of the P OD proximal section, we identified a conserved second microdomain centered around P residues 404-410 that was a major determinant for the efficiency of P-to-L binding. Changes in this connector region likewise had a dominant-negative effect on P bioactivity, suggesting that the section between P OD and P-XD very likely does not exist monomeric in P complexes, but engages in a tertiary assembly. Trans-complementation revealed that the P-OD proximal and connector sections reside in the same functional groups, raising the possibility of an extended interface with L or, if only one of these regions engages in physical contact with L, interference of mutations in the other microdomain with proper assembly of the actual contact zone.

Remarkably, we identified specific residues located on two different α-helices of P-XD that are essential for P-to-L binding. These residues map to a microdomain on a previously unappreciated face of the P-XD triangular prism that is distinct from the side binding MoRE. Importantly, this microdomain resides in a separate functional group from the P OD proximal and connector regions, and mutations destroying this newly discovered L-binding face of P-XD

were recessive in competition studies with wild type P. These results indicate that the P-XD interaction with L is mediated by a single XD subunit of the P tetramer, and that at least two distinct binding sites for different P microdomains exist on L, the P oligomerization domain-proximal tetrameric regions (tetrameric feet) and the P-XD (monomeric head) (**Figure 20E**). Neither site was able to form biochemically appreciable complexes with L in isolation, indicating moderate binding affinities of both interfaces. The formation of stable P-L hetero-oligomers appears to require the avidity gain arising from at least two independent contact sites.

ii) Only one each of the four XDs per P tetramer must be L or MoRE binding-competent (**Figure 20B-1, 2 and 20D-1**). By introducing point mutations in P-XD to the trans-complementation assay that selectively disrupt MoRE or L binding, we demonstrated that a single MoRE binding-competent P-XD is sufficient for wild type P-like RdRP bioactivity (**Figure 20B-2**). This finding is paradigm-shifting since prevailing models assign cartwheeling function to the four XDs of a P tetramer [115, 116], in which the polymerase supposedly advances along the RNP template through iterative formation and release of P-XD contacts with MoRE, ensuring that at all times at least one intact P-XD-MoRE interface is present. Our results demonstrate that no stringent requirement exists, and no P-XD-mediated cartwheeling needs to occur. This conclusion is also consistent with our earlier observation that RNPs formed by N mutants with tail deletions encompassing the C-terminal 86 amino acids that include MoRE are partially bioactive [71].

iii) P-XD interaction with L and MoRE is mutually exclusive, and L-binding of a given P-XD supersedes MoRE-binding (**Figure 20D-2, 20B-3 and 4**). These conclusions are based on the central premise revealed by the mathematical regression analysis of the P $(361\text{-}364)_{Ala}$ competition profile with wild type P, that at most one P $(361\text{-}364)_{Ala}$ monomer can be present in

bioactive mixed P tetramers. Employing the P $(361\text{-}364)_{Ala}$ mutant as a tool to control the stoichiometry of trans-complemented P tetramers, we noted that although only one each of the four P-XDs must be L or MoRE binding-competent, combining these competencies on only one P-XD per tetramer completely abrogates polymerase activity (**Figure 20D-2**). Presumably, steric hindrance prevents that the same P-XD simultaneously engages both MoRE and L. Importantly, the presence of only one (L^+MoRE^+) P-XD and three (L^-MoRE^+) P-XDs in a mixed P tetramer was sufficient to restore wild-type P like polymerase activity (**Figure 20B-3**), but the inverse constellation (one (L^+MoRE^+) P-XD and three (L^+MoRE^-) P-XDs) was entirely bio-inactive (**Figure 20B-4**). This complementation phenotype revealed the dominance of the P-XD interaction with L over MoRE but raised the question of why in the constellation depicted in Figure 20B-4 75% of the P-L hetero-oligomers (those in which one of the (L^+MoRE^-) P-XDs happens to contact L) did not remain bioactive.

iv) During RNA synthesis, P-XD iteratively separates from and reengages with L (**Figure 20B-1 and 4**). In all trans-complementation constellations that assigned L-binding competence to only one P-XD, we consistently noted a boost in RdRP bioactivity compared to wild type P tetramers. This unexpected phenotype can be best appreciated in the Figure 19B-1 setting, but is equally present in the Figure 20B-3 and Figure 20D-1 constellations, since the addition of only one P-$(361\text{-}364)_{Ala}$ monomer to otherwise wild type P tetramers reduced bioactivity by approximately 40% according to our regression model. Consequently, the wild type P-like 100% bioactivity seen for the Figure 20B-3 and Figure 19D-1 constellations reflects a near-perfect additive effect of the activity booster resulting from P-XD assignment and penalty associated with the presence of a P-$(361\text{-}364)_{Ala}$ monomer. Our competition studies of the P-V463R mutant with wild type P returned even higher peak RdRP values reaching 250% of reference bioactivity.

What could be the mechanistic basis for a boost in RdRP activity when only one P-XD subunit is able to interact with L? A previous study considered that negotiation of the encapsidated template by paramyxovirus polymerases might depend on continuous structural rearrangements within the RdRP complex, possibly including the repetitive dissolution and reassembly of P:L interaction [117]. Based on our identification of a bipartite P:L interface and the trans-complementation data, we propose that the newly discovered P-XD:L interface periodically resolves and reforms. In wild type P tetramers, all four P-XDs are L binding-competent. Iterative separation of P-XD from L creates an opportunity for competition between the individual P-XDs to reengage with L and/or need for rearrangement within the P-L hetero-oligomer every time a physically different P-XD than before is successful. Delegating L binding to a designated P-XD monomer as in our mixed P tetramers eliminates internal competition and associated rearrangements of the complex, unleashing maximal polymerase processivity. This conclusion is consistent with the mathematical description of our experimental data and provides ready explanations for why a bipartite P:L interface may have evolved – two distinct contact zones allow temporary separation of only the P-XD:L interface without presumably catastrophic full separation of P from L – and why the trans-complementation pair depicted in Figure 20B-4 is bio-inactive. If P-XD indeed transiently separates from and rebinds to L as the polymerase advances along the template, the single (L^+ $MoRE^+$) P-XD monomer present in every RdRP complex that can potentially initiate RNA synthesis in this constellation will eventually engage L. Because no other MoRE binding-competent P-XDs are present in that P tetramer, this event appears to create a dead-end situation, presumably resembling that experienced by the trans-complementation pair represented by Figure 20D-2.

We propose a 4-step model to describe the dynamic interplay between P, L, and the RNP (**Figure 20E**). The tetrameric base of P remains latched to L at all times, while the P-XD head reiteratively taps L. In the case of wild type P, one P-XD forms a temporary complex with L while another P-XD binds MoRE (stage I). MoRE engagement is thought to induce reorganization of N-tail [118], moving it closer to the core of the RNP helix (stage II). Possibly this change in microenvironment of the binding partners may destabilize the interfaces, resulting in temporary separation of both P-XD:MoRE and P-XD:L, which enables the advancement of the polymerase to the next N protomer (stage III). One of the four P-XDs then rebinds to L and another engages the MoRE of the new N protomer (stage IV), followed by a repeat of the cycle. Assignment of L-binding competence to a specific P-XD does not fundamentally change the process, however, P-XD competition for the L binding site as well as potential rearrangements within the complex when a separate P-XD moiety is present are eliminated because at every cycle the same P-XD monomer rebinds to L (stage III' to IV'). The remaining two P-XDs, not fully depicted in Figure 20E, may or may not engage other MoREs in the vicinity. However, these interactions are not essential for polymerase activity, if they occur. This mechanistic model assigns a fundamental role in regulating polymerase activity to the paramyxovirus P protein and identifies a novel principle, reiterative separation and restoration of P-XD interaction with L, that kinetically regulates RdRP negotiation of the encapsidated RNA template.

1.3 Chapter 2: Identification of a novel RABV entry inhibitor

1.3.1 RABV Disease and Current Treatment

Derived from the Latin word for madness, rabies is an ancient zoonotic viral disease that continues to be a global public health concern causing approximately 60,000 deaths annually. Considered the most lethal vaccine-preventable viral disease, rabies has a world-wide distribution of animal reservoirs and cases have been reported in over 150 countries and territories with 95% of cases occurring in developing countries within Asia and Africa [119]. The etiological agents of rabies disease, lyssaviruses, are characterized as negative-sense non-segmented RNA viruses that are grouped in the *Rhabdoviridae* family. The majority of zoonotic transmission events of RABV are from animal bites that expose the open wound to infectious saliva. After an asymptomatic incubation period that can last from a few days to up to one year, RABV enters the central nervous system via retrograde neuronal transport. Subsequently, the virus causes severe inflammation of the brain and spinal cord [120]. Most cases of rabies disease result in the furious form of rabies that causes hyperactivity, hydrophobia, and excitability within patients and eventually leads to death from cardio-respiratory failure. The less-common form of rabies disease, paralytic rabies, presents as a slow paralysis stemming from the initial site of infection that gradually takes over the body and is followed by a coma preceding death [121]. Diagnosis of rabies is only possible in late stages of infection due to immune evasion strategies of RABV and the treatment window closes once clinical signs develop [7]. Post-exposure prophylaxis treatment (PEP) of rabies disease for naïve individuals consists of passive immunization with human-derived anti-RABV immunoglobin (hRIG) combined with RABV vaccine on the day of exposure, followed by three additional doses of vaccine given on days 0, 3, 7, and 28 (**Figure 21**). For previously vaccinated individuals, the vaccine is administered on days

0 and 3 per WHO guidelines [7, 119, 122]. Although there are early and effective treatment options available both in the United States and abroad, the cost of PEP has increased by almost 400% in the past decade. Currently, in the United States, the cost of PEP can exceed $3,000/dose. In Africa and Asia, this cost equates to nearly 40-times an average daily income [119]. Prohibitive cost and limited supply of hRIG has led some countries to try alternative and more economical PEP treatments, such as equine RIG (eRIG). Treatment with eRIG, though effective, has resulted in severe adverse side effects including anaphylaxis, serum sickness, and other allergic reactions [123-125]. The exorbitant price and ineffectiveness of the current PEP treatment against emerging zoonotic phylogroup II lyssaviruses such as Mokola virus (MOKV), and Lagos bat virus have underscored an unmet clinical need for discovery of efficacious antiviral treatment against RABV [121, 126].

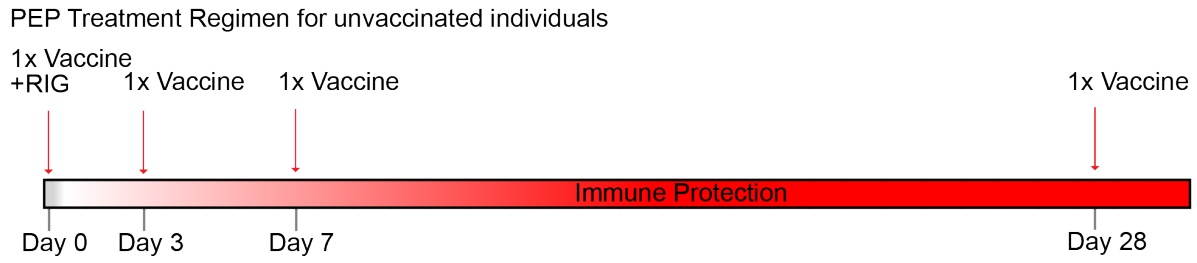

Figure 21. *Schematic diagram representing the current post-exposure prophylaxis treatment (PEP) schedule as recommended by the WHO for naïve individuals (from Du Pont et. al., 2018) [126]*

1.3.2 RABV Genome and Virion Organization and Replication

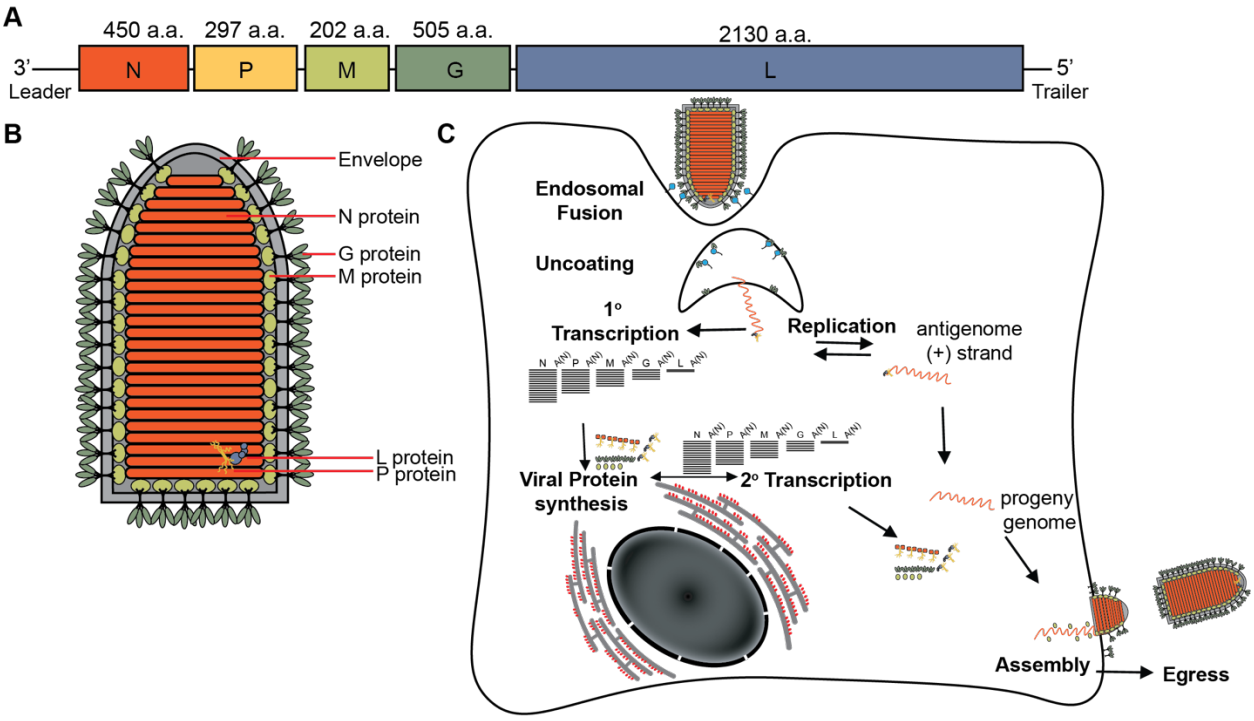

Figure 22. *RABV Genome, Virion and Lifecycle* ***A)*** *Schematic diagram of RABV genome organization.* ***B)*** *Diagram of bullet-shaped RABV virion. Host-derived envelope (black), L (lavender), P (yellow), N/RNP (orange), G (dark green), and M (light green) are denoted.* ***C)*** *Replication cycle of RABV*

RABV is a negative-sense nonsegmented RNA virus of the lyssavirus genus within the viral family *Rhabdoviridae*. The viral genome, which consists of aproximately 12,000 nucleotides, encodes five structural proteins, N, P, M, G, and L (**Figure 22A**) [128]. The host-derived viral envelope has a characteristic bullet-shape due to a complex of two nested left handed helices comprising of a spiraling inner layer of N encapsidated viral genome coated by an outer layer of M protein (**Figure 22B**) [129]. Host receptor binding and endocytotic viral entry is mediated by G, a trimeric type 1 membrane protein on the surface of the virion. Interaction of G with host cellular receptors (NCAM, p75TR, and aChR) triggers endocytosis of

the virion in a clathrin-dependent manner using the endosomal transport pathway [130-133]. Release of the RNP occurs after low pH-induced fusion between G and the endosomal membrane (**Figure 22C**)[134, 135]. L and P constitute the functional RdRP heterocomplex and are pre-loaded onto the genome to form the RNP. Viral replication and transcription occur within viral factories within the cytoplasm called Negri bodies [136, 137]. Transcription begins at the 3′ leader end of the viral genome. Viral monocistronic mRNAs are transcribed using genomically encoded start and stop signals, beginning with the N ORF. All mRNAs are capped and polyadenylated by L. The 3′-poly(A) tail consists of approximately 100-250 nucleotides. VSV L has been shown to have a unique capping mechanism that uses GDP as the methylation moiety for the cap structure via a specialized PRNTase domain. It is also assumed RABV caps mRNA in a similar fashion due to conservation of the PRNTase domain within the family [4]. A transcriptional gradient occurs during viral mRNA synthesis that results in a gradual decrease of transcripts starting from the 3′ leader to the 5′ trailer due to attenuation of reinitiation of the polymerase complex and variable intergenic seqeunce (IGS) lengths [138]. Replication of the viral genome occurs when RABV ignores transcription cues to produce antigenome, which in turn is used as the template to replicate genomic RNA. Both genome and antigenome are concomitantly encapsidated by N during replication. This process is faciliatated by N^0P complexes, whose accumulation has been implicated in the switch from the transcriptase to replicase mode for the polymerase [139, 140]. The RABV M also modulates polymerase activity by inhibiting transcription and stimulating replication [141, 142]. M coats and condenses the RNP and budding is facilitated by recruitment of ESCRT machinery and interaction with cytoplasmic tails of G [51]. Interestingly, it was found that budding still occurs in the absence of

G, however egress is a much slower and less efficient process that leads to more cell-associated virions, which has been used to facilitate pseudotyping [143].

1.3.3 Current RABV Treatment

The onset of clinical symptoms of rabies disease is universally fatal, however, there exist rare documented cases of survival after aggressive treatment was administered. All patients, except one, received doses of PEP combined with vaccine and all patients developed life-long neurological sequelae [122]. Also, because of the rarity of survival from symptomatic rabies, there exists debate whether the surviving patients actually were infected with RABV due to the absence of virus or viral antigens. The single survivor without PEP had undergone the Milwaukee Protocol (MP). The MP is a combinatorial therapy including a ketamine-induced coma with regular administration of ribavirin, midazolam, heparin, amantadine, and high doses of benzodiazepines and barbiturates [144]. The induction of coma is predicted to reduce neuronal cell damage and slow disease progression by reducing over-stimulation of brain cells. Presumably this also enables time for the adaptive immune response to develop protective antibodies. The singular success of the MP, and the 31 documented failures thereafter has prompted speculation that the survival of the MP patient was due to infection with an atypical RABV strain or low virulence within the bat that bit her [144-149]. The aggressive treatment options for pre- or post- symptomatic rabies include ribavirin, interferon-α (IFN-α), and ketamine/amantadine. Ribavirin is a broad-spectrum antiviral analogue of guanosine. Ribavirin has shown *in vitro* efficacy against several encephalitis inducing viruses, including Japanese encephalitis virus, West Nile virus, Argentinian hemorrhagic fever, hantavirus pulmonary syndrome, influenza, RSV, human immunodeficiency virus, MeV and CDV [27, 150-155]. Ribavirin has multiple mechanisms of action that directly affect RNA and DNA synthesis in

addition to inhibition of the *de novo* purine synthesis pathway [156-158]. So far, no clinical effect has been observed after treatment of rabies with ribavirin, and *in vivo* studies have demonstrated that it exhibits marginal penetration across the blood-brain barrier (BBB), though low levels were detected in cerebrospinal fluid after oral administration to HIV patients after several weeks [159-161].

IFN-α is a type I interferon has been administered to induce triggering of the innate immune response pathways. However, the lyssavirus P gene produces multiple truncated isotypes designed to antagonize the interferon-driven innate immune response. All P isotypes act directly to prevent STAT1 migration to the nucleus. P1 and P2 directly engage STAT1 and sequester it to the cytoplasm by encoding a nuclear export signal, P3 competitively binds to the STAT1 DNA binding site, as well as binds microtubules to block STAT1 shuttling to the nucleus [162]. The antagonistic properties of RABV P against STAT1 functionality make IFN-α a poor anti-viral treatment. The dissociative anesthetic, ketamine, rapidly penetrates the BBB and at prohibitively high concentrations has been shown to inhibit genomic replication of RABV in rat cortical neurons [163]. Even though ketamine was used in the MP, it was more likely included for its sedative properties than for potential therapeutic uses.

1.3.4 RABV Drug Discovery

As denoted in Tables 1 and 2, there have been multiple small-scale attempts at antiviral drug discovery against RABV, however, identification of druggable targets remains a great hindrance for advancement of small molecule hit candidates [127]. Druggable targets are identified by their affinity to bind to a commercially viable compound (i.e. one that is bioavailable and adheres to Lipinski's rule of five) that affects physiological function and provides therapeutic benefit [164].

One approach of antiviral drug discovery often implemented is the identification and indirect targeting of essential host proteins exploited by RABV for replication and pathogenesis. By indirectly targeting the viral lifecycle, there are several advantages over direct-acting antivirals (DAA):

i) There is a high barrier for resistance against host-targeting antivirals (HTA) due to host genetic stability provided by the proofreading capabilities of host polymerases in contrast to the low fidelity of viral polymerases.

ii) There are numerous host proteins that RABV exploits compared to the limited number of druggable viral proteins.

iii) There are a plethora of FDA-approved drugs targeting pro-viral host factors that can be repurposed to fast-track antiviral development.

iv) Broadened antiviral indication can be achieved by targeting commonly used pathways by members of the viral family, e.g. emerging viruses such as the phylogroup II lyssaviruses.

Table 1. *Host-directed RABV inhibitors*

Compound	Target	EC_{50} (uM)	CC_{50} (uM)	SI (CC_{50}/EC_{50})	Ref.
Catechin	Host Cell GAGs	36.50 ± 8.40	124.33 ± 33.53	3	[164, 165]
Quercetin	Host Cell GAGs	191.68 ± 24.25	670.02 ± 180.18	3	[164, 165]
3,4,5-Trimethoxybenzoic acid	Host Cell GAGs	2142.74 ± 266.3	>5042.41	2	[164, 165]
Trimethoxyacetophenone	Host Cell GAGs	1023.98 ± 64.62	3738.98 ± 1099.17	3	[164, 165]
3,4,5-Trimethoxybenzoic acid ethyl ester	Host Cell GAGs	822.23 ± 134.38	3204.20 ± 397.87	3	[164, 165]
Butyl gallate	Host Cell GAGs	109.79	113.23 ± 52.35	1	[164, 165]
PAV-866	ABCE1	~0.15–0.30	~2.5–10	~100	[166]
Sorafenib	Tyrosine Kinases	1.463	>160	109	[167]
2-piperidin-3-yl-benzothiazole analog	Nedd4	0.345	>1	>3	[168]
1-acetyl-3-(2,2,2-trifluoroethyl)-urea analog	Nedd4	0.210	>1	>8	[168]

*Table from *Du Pont et al., 2019 [126]*

Despite the promising advantages of HTAs, there are disadvantages such as cytotoxicity, irreproducibility *in vivo*, or prohibitively high 50% effective dose concentrations (EC_{50}) that impede serious development initiatives, as shown in Table 1 [170]. This is particularly evident in the current trend of repurposing cancer drugs for antiviral therapy [171]. RABV, like many other viruses, depends on the extracellular signal-regulated kinase (ERK) pathway for efficient viral pathogenesis. Sorefenib, a multikinase inhibitor of the ERK pathway approved for treatment of hepatocellular carcinomas has shown some efficacy against various viruses including adenovirus, MuV, chikungunya virus, dengue virus, West Nile virus, Yellow fever virus, and enteroviruses. Against RABV, this drug demonstrated only 77% viral inhibition *in vitro*, and

exhibited antagonistic properties when combined with ribavirin and IFN-β [172]. Not uncommon to cancer targeting drugs, Sorefenib has unfavorable adverse side-effects making it a poor candidate to advance for antiviral development [173-177]. An innovative drug screen specifically targeting nucleocapsid assembly identified a hit targeting the ABCE1 transporter proteins. The 50% cytotoxic concentration (CC_{50}) of this compound was exceptionally low 2.2-10 μM, thus closing the door on its potential. Minocycline has also been investigated for potential therapeutic use against RABV due to its ability to cross the BBB, ability to suppress HIV replication, and its demonstrated neuroprotective effects [178, 179]. When tested against RABV in neonatal mice, a disturbing turn of events revealed exacerbation of the disease by inducing an earlier onset of neurological symptoms [180] . And lastly, another screen of phenolic compounds as potential RABV drug candidates due to previous efficacy demonstrated against other viruses [165], showed demonstrated >50 μM EC_{50} virucidal activity against RABV, which is prohibitively high, thus limiting foreseeable advancement of these compounds for drug development.

The cytotoxicity and lack of successful *in vivo* studies with drug candidates prompted the discovery of DAA, Table 2, as a promising alternative strategy for therapeutic intervention. RABV proteins are a rich source of druggable targets that contain multi-functional domains, lack cellular orthologs, and engage in dynamic PPI. The highly conserved nature of RABV N, and its critical function for genome encapsidation and RdRP recruitment makes it an enticing druggable target. Several studies have shown that RNA interference (RNAi) technology targeting N can inhibit viral replication *in vitro* [181-185]. When tested *in vivo* however, there was only a 60% survival rate against RABV [181]. Similarly, small hairpin RNAs targeting N delivered by adeno-derived viral vectors were also shown to inhibit RABV and marginally increase the survival rate of mice [182]. Despite the promising avenue of RNAi therapy, the mode of efficient

delivery remains a barrier for effective antiviral treatment and was considered the reason for failure with these studies. The heterocomplex formation between RNP and P has also been investigated as a potential antiviral target. In an attempt to generate a broad-spectrum lyssavirus inhibitor, a Y2H screening assay was employed against both RABV P and MOKV P. The study identified several peptides with antiviral effect against RABV infection due to disruption of the RNP-P interaction when tested in peptide-transfected cells [186]. Similarly, peptides were shown to inhibit infection of neuronal cells by specifically targeting the amino terminal 42 and 60 residues of P [187]. Neither of these studies tested the peptides for *in vivo* efficacy and despite antiviral effect and high specificity, efficient drug delivery of therapeutic peptides remains a difficult and expensive obstacle to overcome [170]. The strong homology between lyssaviruses gleaned from recent structural information potentiates structure-guided design of broad-spectrum small-molecule inhibitors with cell permeability.

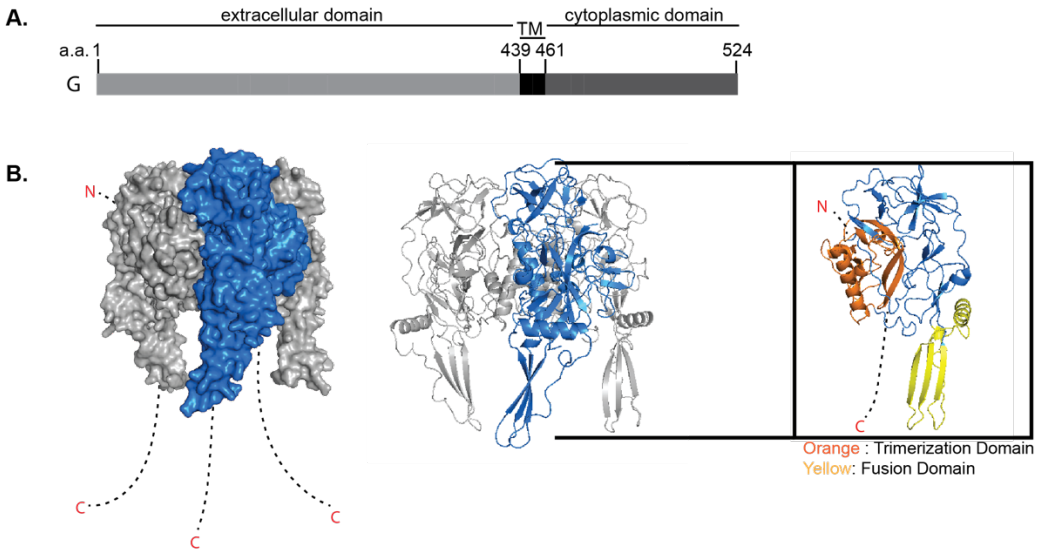

Figure 23. *Rabies virus glycoprotein A) Linear schematic of RABV G organization and amino acid position of the extracellular domain, the transmembrane domain, and the cytoplasmic domain. B) Homology model of RABV G trimer based on VSV G (PDB: 2J6J) and division of each functional domain: trimerization domain (orange), and fusion domain (yellow). [187-190]*

The primary PEP approach to combating RABV infection remains antibody therapy specifically targeting G **(Figure 23 A,B).** Despite continued and reasonably successful efforts to develop cross-strain antibodies, antigenic drift, cost, and cold-chain requirements prevent them from being a viable solution for individuals in developing nations that require PEP the most. Not to mention the lack of efficacy of PEP after the onset of clinical symptoms [192]. Besides antibodies, no further identification of entry inhibitors specifically targeting RABV G has been accomplished, though a couple of compounds have been identified to competitively inhibit RABV entry by interacting with its host receptors. One such compound derived from snake venom has been shown to prevent RABV entry, however, it irreversibly binds to AChR and subsequent studies have not been able to replicate this result [193]. Furthermore, RABV G interacts with multiple ubiquitous host receptors suggesting that direct targeting of G is a superior antiviral strategy. The antigenic sites discovered through antibody adaptation studies, or the more conserved stalk region of G are possible targets for small-molecules that would alleviate the cost barrier and cold-chain requirement [188, 194-197].

As a core constituent of the RdRP heterocomplex, L is organized into highly conserved enzymatic domains that specialize in RNA synthesis, mRNA capping and mRNA methylation (**Figure 24 A,B**) [198]. Pyrimidine analog, ara-C was shown to partially inhibit viral replication, though only at levels that completely abrogated host DNA synthesis [199]. Another pyrimidine analog, 6-Azauridine that showed virus reduction *in vitro*, however, was only efficacious against lab adapted RABV strains [200]. Viral inhibition was observed with purine analogs vidarabine and (S)-DHPA but the mechanism of inhibition was found to prevent both host and viral RNA synthesis [201]. In an effort to reduce cytotoxicity and enhance specificity, ribavirin analogs were also tested for efficacy against RABV but were found to only be potent against the vaccine

strain. Favipiravir, a broad-spectrum RdRP inhibitor, was also tested for efficacy against RABV. When tested against mice, there was a 50% survival rate, and the survivors developed debilitating limb paralysis [202, 203]. Furthermore, Favipiravir (T-705) has teratogenic and embryotoxic properties that also make it a less attractive drug candidate [35].

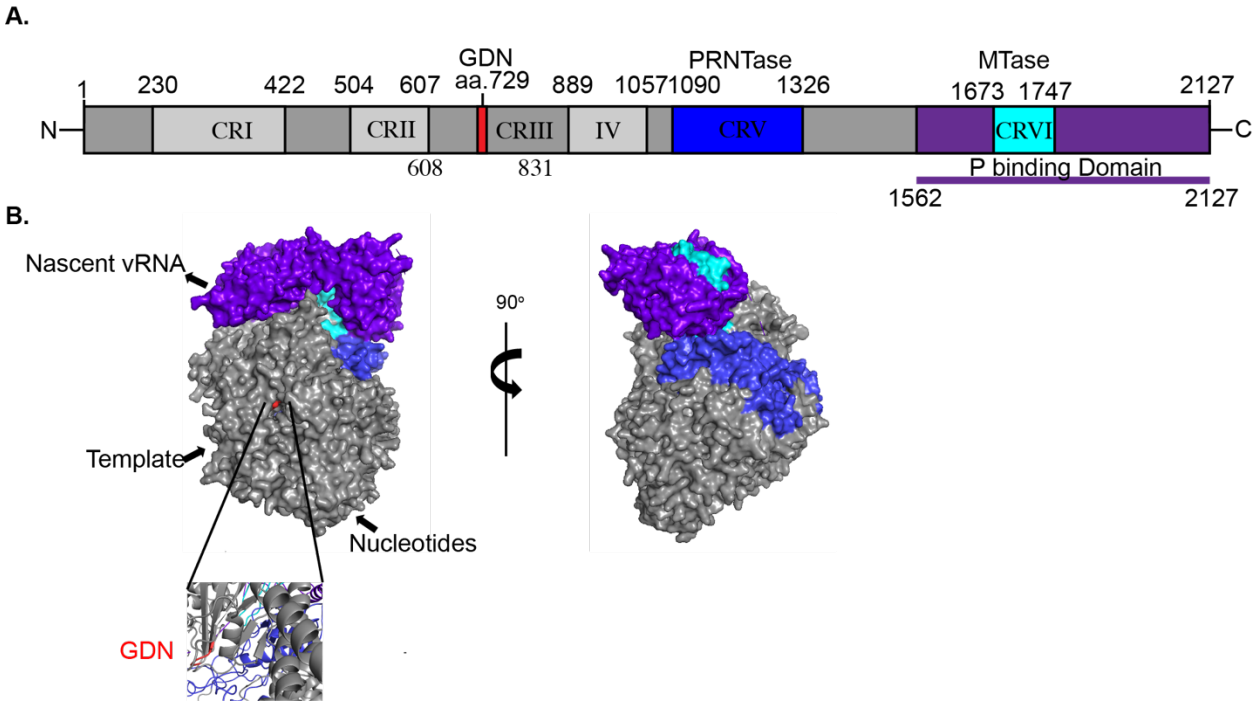

Figure 24. *Rabies virus large protein A) Schematic diagram depicting the domain organization of RABV large protein (L). The GDN polymerization motif is in red. The polyribonucleotidyltransferase (PRNTase) is in blue. The methyltransferase (MTase) is in cyan. The phosphoprotein (P) binding region is purple. Conserved regions (CR) of the non-segmented negative-sense RNA viruses are labelled CR I -VI.* ***B)*** *Surface representation of the RABV L generated by homology modelling based on the coordinates reported for the closely related VSV L structure. Below is a zoomed in ribbon representation of the GDN motif responsible for polymerase activity in red. [204-207] (Figure from Du Pont et al., 2019 [127]*

***Table 2**. Direct-acting RABV inhibitors*

Compound	Target	EC_{50} (uM)	CC_{50} (uM)	SI (CC_{50}/EC_{50})	Ref.
Ketamine	vRNA Synthesis	922.93 ± 68.48	3010.69 ± 171.26	3.3	[164, 207]
Ribavirin	*de novo* purine synthesis	18.55	>200	>10	[208]
EICAR	*de novo* purine synthesis	0.90	>200	>200	[208]
EICNR	*de novo* purine synthesis	3.80	>200	>50	[208]
Favipiravir	vRdRp	32.4	>2500	>1000	[202, 209]

*Table from *Du Pont et al., 2019 [126]*

1.3.5 Aim of Dissertation Chapter 2

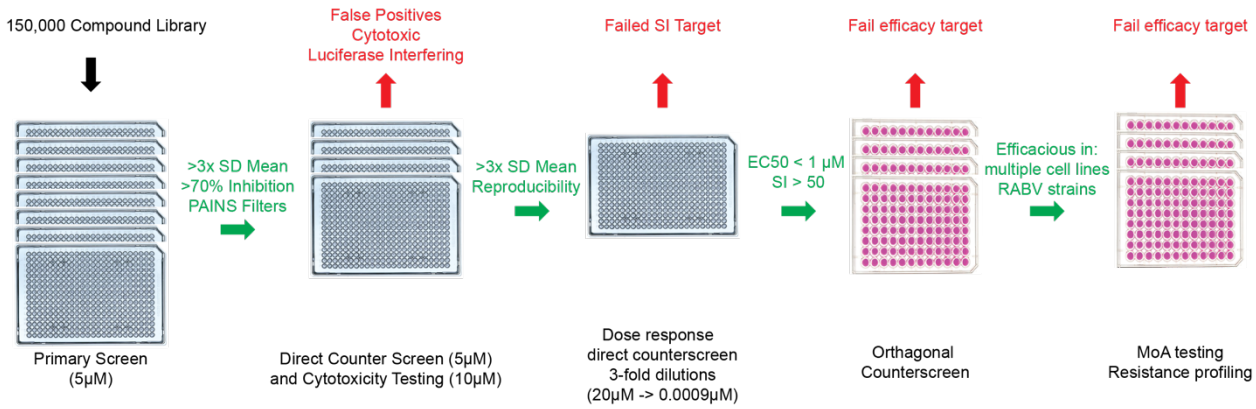

Figure 25 Flow chart detailing HTS compound hit compound identification and counter-screening strategies employed for hit compound discovery and verification. Concentrations of compound are detailed, as well as hit progression and removal criteria.

The cold-chain requirement, high cost, and lack of effectiveness against emerging zoonotic lyssaviruses of the current RABV PEP treatment has underscored an unmet need for antiviral drug discovery. To date, none of the small-scale screening campaigns against RABV have come close to presenting an alternative to current treatment that is safe, efficacious, BBB permeating, and specific to RABV.

The primary aim of this study was to address this growing clinical need by employing a high-throughput screening (HTS) campaign using a novel BSL-2 compatible RABV reporter virus that is limited to single-cycle infection. This reporter virus was tested in 384-well format

against multiple in-house open-discovery screening compound libraries specifically curated to exclude compounds with problematic chemistry. The mechanism of action and therapeutic potential of hit candidates were characterized with systematic counter and orthogonal screens. The efficacy of confirmed hits was also tested in the context of multiple replication competent RABV reporter strains. One viable hit, GRP-60367, was further characterized for mechanism of action and resistance profiling (**Figure 26**).

1.3.6 Chapter 2 Materials and Methods

Cells: Human bronchial epithelial cells (BEAS-2B; ATCC CRL-9609), human embryonic kidney cells (HEK-293T; ATCC CRL-3216), baby hamster kidney cells stably expressing T7 polymerase (BSR-T7/5) and African green monkey kidney epithelial cells (Vero; ATCC CCL1-81) were maintained at 37^{o}C in 5% CO_2 in Dulbecco's modified Eagle's medium (DMEM) supplemented with 7.5% fetal bovine serum. The BSR-T7/5 cell line was supplemented with G-148 every 5th passage and cells were transfected using GeneJuice (Novagen) according to the manufacturer's instructions.

Molecular Biology: Point mutations of escape mutants from adaptations were introduced via the QuickChange mutagenesis PCR protocol. Recombinant viruses were produced by introduction of point mutations in a shuttle vector that used restriction sites mluI and NheI to transpose the G ORF to a vector containing full length genomic DNA.

Compounds: The screening set contained a compilation of commercially available libraries (ChemDiv, 30,000 compounds; ChemBridge, 100,000 compounds; and proprietary collections from the Emory institute for drug development, 1,155 compounds; and Kansas University,11,520 compounds) that are specifically curated against compounds with pan-assay interfering or other undesirable chemical structures. The compounds from each library were

dissolved in dimethyl sulfoxide (DMSO) to a concentration of 10 μM and stored at -80°C. All HTS electronic compound management, data storage, and data analysis was performed using the MScreen software package. Prior to screening, all compounds were inventoried in Mscreen and reformatted into barcoded 384-well plates using a Nimbus96 liquid handler (Hamilton Robotics). Each 384-well daughter plate consists of positive (cycloheximide) and negative (DMSO) controls in a checkerboard pattern on the two lateral columns on both sides of every plate.

HTS Protocol: BEAS-2B cells ($3.5x10^3$/well) were seeded in barcoded 384-well white wall/clear bottom plates using a MultiFlo automated dispenser (BioTeK) equipped with dual 10 μl peristaltic pump manifolds followed by collection (150 x g for 90 sec at 25°C) and incubated for 14 hours at 37°C in 5% CO_2. Compound addition for a final concentration of 5 μM (20 nl/well) was performed by the Nimbus96 liquid handler outfitted with a high-density pintool (V&P Scientific) attached to the pipetting head. Both source and assay plates were read by the Nimbus96 unit at the time of compound stamping**.** Co-infection of recRABVΔG-SBNG (multiplicity of infection (MOI) = 0.01) at 10 μl/well was performed using a Multiflo dispenser followed by spin collection and incubation at standard conditions for 48 hours post-infection. Plates were loaded into an H1 synergy plate reader (BioTek) with a stacker and identified with an integrated barcode reader, that also automatically injected nano-Glo substrate (10 μl/well) and bioluminescence was recorded 3 minutes after substrate addition.

HTS Data normalization and Hit identification: Data analysis was performed using raw data imported from the Nimbus96 (source and assay barcode maps) and plate reader bioluminescence readouts to the Mscreen software package. Normalized relative inhibition values were calculated by dividing the results by the difference between positive and negative plate control means. Robust z-scores were calculated by the formula: robust *z*-score = (S_i –

median (S_{all}))/MAD(S_{all}) and MAD(S_{all}) = 1.4826 × median (|S_i – median (S_{all})|) (where S_i = individual compound value, and S_{all}= values of all compounds on the plate). Hit candidates were defined as compounds with ≥ 70% inhibition of normalized signal intensity against recRABVΔG-SBNG, a robust z-score ≥2.0, and <35% inhibition against RSV-FF, WSN-nano, and HPIV-3-nano. Hit candidates were also queried using the SciFinder database package to determine known bioactivity.

Automated dose-response counter-screening: BEAS-2B cells (3.5 x 10^3 cells/well) were seeded in barcoded white wall/clear bottom 384-well plates using a MultiFlo automated dispenser as described above. The Nimbus96 unit was used to prepare 3-fold dilutions hit compounds (0.078 – 10 μM) in barcoded 384-well plate format for subsequent dose-response and cytotoxicity counter-screening. BEAS-2B cells (3.5 x 10^3/well) were seeded in barcoded white wall/clear bottom 384-well plates using a MultiFlo automated dispenser as described above, then stamped with the counterscreen plates using the high-density pin tool. Cell viability in the presence of compound was tested using PrestoBlue substrate (5 μl/well) (LifeTechnologies) 48 hours post compound addition. Addition of PrestoBlue was performed according to the manufacturer's instructions and read using the H1 synergy plate reader (excitation at 560 nm, emission at 590 nm and gain of 85).

Dose response reporter Assays: The Nimbus96 unit was used to transfer three-fold or five-fold serial dilutions (as indicated by the Figure) of hit candidate compounds to 96-well plates seeded with BEAS-2B, 293T, or BSR-T7/5 cell lines (1.5 x 10^4 cells/well). Controls included four positive (1 mg/ml cycloheximide) and four negative (0.05% DMSO) wells on each plate. The cells were infected with recRABVΔG-SBNG (MOI = 0.1) using the MultiFlo dispenser and bioluminescence reporter activity was read by the H1 synergy plate reader 48

hours post infection. Dose-response inhibition curves were generated according to the formula: % inhibition = $(X_{Sample} - X_{Min})/(X_{Max} - X_{Min}) \times 100$, with X_{Min} representing the average of the positive and $X_{Max}$the average of the negative control wells and the Prism (GraphPad) nonlinear regression function with a four-parameter regression slope was applied to determine 50% effective concentration (EC_{50}) of each hit compound. All dose-response activity assays were performed in 3 independent repeats.

Kinetic cell-cell fusion assay: BEAS-2B cells (1.5 x 10^5 cells/well) were cotransfected with 1.0 μg RABV-G or RABV-$G_{escapemutant}$ expression plasmids and 0.5 μg DSP1-7 expression plasmid. DSP8-11 was transfected independently. Cells were harvested 24 hours post-transfection and reseeded with equal parts of G and DSP_{1-7} containing cells with DSP_{8-11} containing cells in a 96-well plate to a total of 4 x 10^3 cells/well. Cells were pretreated with viviren substrate 4 hours post-reseeding for 1.5 hours according to the manufacturer's instructions. Fusion was triggered by the addition of 100 μl of DMEM with pH=6.0 and ViviRen signal was measured by the Cytation5 cell imaging multimode reader (BioTek) every 30 minutes for 4 hours. Values are shown as percent normalized to RABV-G and are based on 3 independent repeats.

Virus Adaptation: BEAS-2B cells were infected with recVSV-GFP-RABV-G with an MOI of 0.1 $TCID_{50}$ units/cell and incubated for 30 min at 37°C 5% CO_2 before addition of 1.1 μM of GRP-60367. Fresh BEAS-2B cells were infected with 10-fold dilution of supernatant-associated virions every two days with gradual increase of compound until 100 μM was tolerated. Total RNA was extracted from 8 individually adapted clones and cDNAs were generated using random hexamer primers, and the G protein ORF was amplified and subjected to Sanger sequencing. Confirmed escape mutations were introduced to G protein expression

plasmids and also rebuilt into the recVSV-GFP-P plasmid background for recovery of escape mutants in the context of full-length virus.

Recombinant Virus Recovery: RecVSV-RABV-G were recovered as previously described [211]. Briefly, plasmid vectors expressing VSV-N (0.5 μg), VSV-P(0.4 μg), VSV-L (0.2 μg) and plasmid with genomic recVSV-RABV-GFP or recVSV-RABV-G-GFP mutants (1.0 μg) were transfected in BSR-T7/5 cells (2.5 x 10^5 cells/well) and incubated at 37^{o}C and monitored for viral particle formation by visualized GFP signal. Viral supernatant was overlaid onto fresh Vero-E6 cells infection was allowed to proceed and viral supernatant was collected and $TCID_{50}$ was quantified by GFP signal.

Surface biotinylation, SDS-PAGE and immunoblotting: BSR-T7/5 cells were seeded in a 6-well plate (4 x 10^5 cells/well) and transfected with 1 μg of RabV G or RABV G adaptation mutants. Twenty-four hours post-transfection cells were washed twice in cold PBS, cells were then biotinylated with 0.5 mg/ml sulfosuccinimidyl-2-(biotinamido)ethyl-1,3-dithiopropionate (Pierce) for 30 minutes, quenched with 1M Tris (pH 7.5), and washed three times with cold PBS prior to lysis in RIPA buffer (1% sodium deoxycholate, 1% nonidet P-40, 150 mM NaCl, 50 mM Tris-Cl at pH 7.2, 10 mM EDTA, 50 mM NaF, and protease inhibitors (Pierce)). Strepdavidin bead slurry was added to each cleared lysate sample (14,000 rpm for 30 minutes at 4^{o}C) and incubated on a rotor for 2 hours in 4^{o}C. Washed precipitates and total lysates were fractioned by SDS-PAGE and transferred onto a PVDF membrane by semi-dry transfer. Proteins were detected by immunoblot with anti-RABV G antibodies derived from rabbit sera followed by chemiluminescent detection with a ChemiDoc digital imaging system (Bio-RAD).

1.3.7 Chapter 2 Results

1.3.7.1 HTS Protocol Validation and HTS of RABV-ΔG-nanoLuc

One of the hurdles for large-scale anti-RABV drug discovery continues to be the requirement for BSL-2^{+} containment. In order to overcome this obstacle, we designed a first-in-class RABV reporter strain that replaces the RABV G protein ORF with that of nano-luciferase (RABV-ΔG-nanoLuc) (**Figure 26A**). RABV-ΔG-nanoLuc was rescued via co-transfection of genome-encoding plasmid with helper plasmids encoding for N, P, and L proteins in vaccine strain SAD-B19 G-expressing starter cells. The resultant virus was a recombinant pseudotyped RABV reporter strain that is limited to single-cycle infection**.**

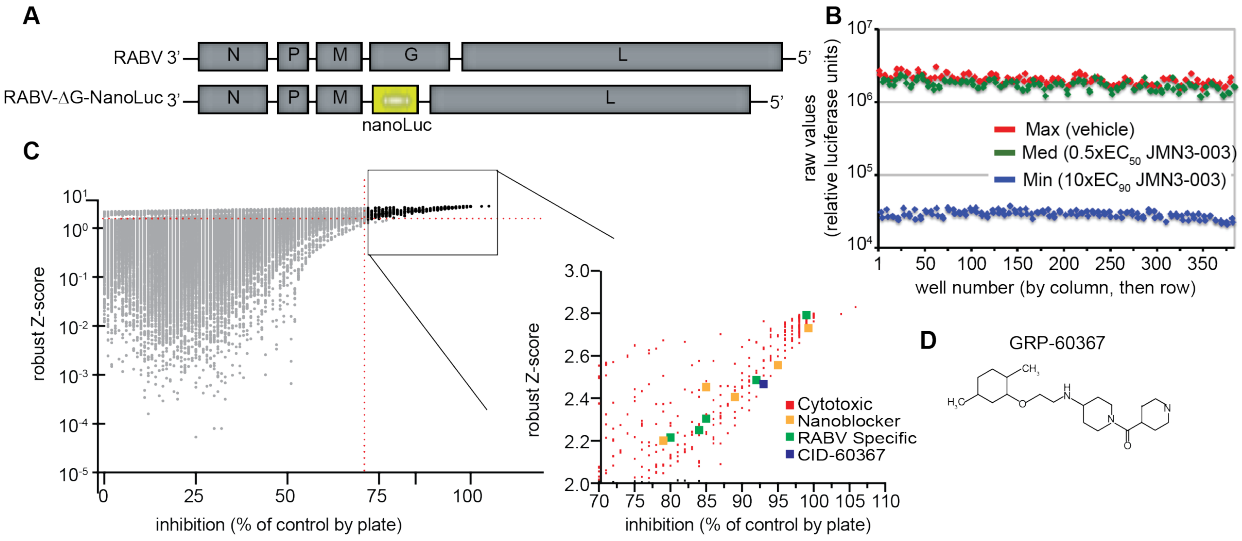

*Figure 26 Identification of a small-molecule hit specific against RABV **A)** Representation of standard RABV (top) and RABV-ΔG-nanoLuc (bottom) B) Validation assay of vehicle treated RABV-ΔG-nanoLuc compared to treatment with broad-spectrum DHODH inhibitor JMN3-003 003 at 0.5xEC50 and 10xEC90 concentrations in 384-well format. **C)** Rocket plot of compound inhibition vs. robust Z-score for hit compound identification. Red dashed line signifies cut-off criteria for hit candidates (>70% RABV inhibition and Z-score >2.0). Cytotoxic (red), nanoblocking compounds (yellow), RABV specific compounds (green) and hit candidate GRP-60367 (blue) are indicated in the zoomed in portion of the graph. **D)** Chemical structure of hit candidate GRP-60367.*

In order to validate RABV-ΔG-nanoLuc in the context of our previously established screening protocol [212, 213], we first tested the robustness of the protocol in 96-well plate format. Three reference plates were seeded with BEAS-2B cells and organized into alternating columns of vehicle (no inhibition (max)), intermediate (0.5 x EC_{50}), or sterilizing concentrations (10 x EC_{90}) of the broadly active polymerase inhibitor JMN3-003 [214] (**Figure 26B**). In order to emulate HTS conditions, fully automated cell seeding, liquid handling, and plate detection equipment was utilized. This assay served to test the ability of the protocol to reliably detect viral inhibition and allowed us to quantitatively assess signal-to-background ratios, Z' values, and coefficients of variation (CV). Forty hours post-infection, the luciferase signal was between 71.6-82.0-fold of background, the Z' value was 0.5, and the CVs averaged to 16%. All of these values were within acceptable and established thresholds, which prompted us to continue with automated HTS to search for inhibitors of RABV [212, 215].

HTS screening was accomplished by miniaturizing our assay to 384-well format and testing approximately 150,000 compounds from our highly curated in-house screening library for RABV-ΔG-nanoLuc inhibition. All compounds were tested at a final concentration of 5 μM. For hit candidate selection, we implemented our standardized bidirectional statistical approach that compares control-dependent % inhibition by plate (>70% inhibition) and robust z-score (z-score >2.0) [212, 213, 215]. This approach yielded a total of 386 hit candidate compounds. Frequently occurring hits were further filtered out based on activity in previous HTS screens. We scanned our database using the MScreen software to identify compounds with 35% inhibition or greater against previously screened viruses: WSN-nanoLuc (-18 compounds), HPIV-3-nanoLuc (-279 compounds), and RSV-FireSmash (-39 compounds) (**Figure 26C**) [213]. The remaining 50 compounds were counter-screened in 384-well format to establish reproducible efficacy, tested

for cytotoxicity and target virus-specificity in 3-fold dilutions with a range of 20 μM to 0.009 μM. Only one of the hits, GRP-60367 (**Figure 27D**), consistently exhibited promising nanomolar dose-dependent virus inhibition, RABV specificity, and had no significant cytotoxicity.

1.3.7.2 Determining the mechanism of action of GRP-60367

Strong viral inhibition by GRP-60367 was confirmed in several established human cell lines, returning EC_{50} concentrations of 3.0 nM, 2.0 nM, and 51.8 nM in BEAS-2B, HEp2, and HEK-293T cells, respectively (**Figure 27A**). There was no observable cytotoxicity in all three cell lines when the compound was added up to a concentration of 300 μM, yielding a selectivity index (SI, CC_{50}/EC_{50}) >16,000 (**Figure 27A**). In order to test the indication spectrum of GRP-60367 and its efficacy in neuronal cells, we pseudotyped RABV-ΔG-nanoLuc with the G proteins of two RABV strains: the mouse-adapted neurotropic N2c strain [216] and a bat-derived Ef strain [217] . There was no observable cytotoxicity in the neuronal cell line N2a **(Figure 27B, gray)**. The screening virus exhibited a slightly increased EC_{50} of 0.43 μM. The viruses pseudotyped with the EF and N2c G proteins exhibited even higher EC_{50} values of 2.71 μM and 3.35 μM respectively (**Figure 27B**). Previous studies have shown SAD-B19, our screening strain, to be poorly neurotropic as compared to N2c [218]. The difference in infectivity of N2a cells has been attributed to differences in propagation and selection pressure in tissue culture cell lines [219]. The decline in potency against the neurotropic N2c and EF strains may result from the slower kinetic with which SAD-B19 G infects neuronal cell lines, while ease of entry by the neurotropic EF and N2c G proteins more easily evades compound binding.

In order to mechanistically characterize GRP-60367, we employed a time-of-addition (TOA) that allowed us to ascertain which step of the viral life cycle the compound was blocking. Virucidal activity of GRP-60367 was most effective when added at the time of infection,

however, compound efficacy steadily declined each hour of addition thereafter and lost major efficacy 2 hours post infection (**Figure 27C**). This TOA profile is consistent with previously described entry inhibitors [213, 220-222]. Recently identified RABV entry inhibitor, tryphostin 9 similarly exhibited gradual decline in efficacy that eventually plateaued after 7 hpi, and contrasts with polymerase inhibitor TOA profiles, which continue to have efficacy up to 9 hpi [213].

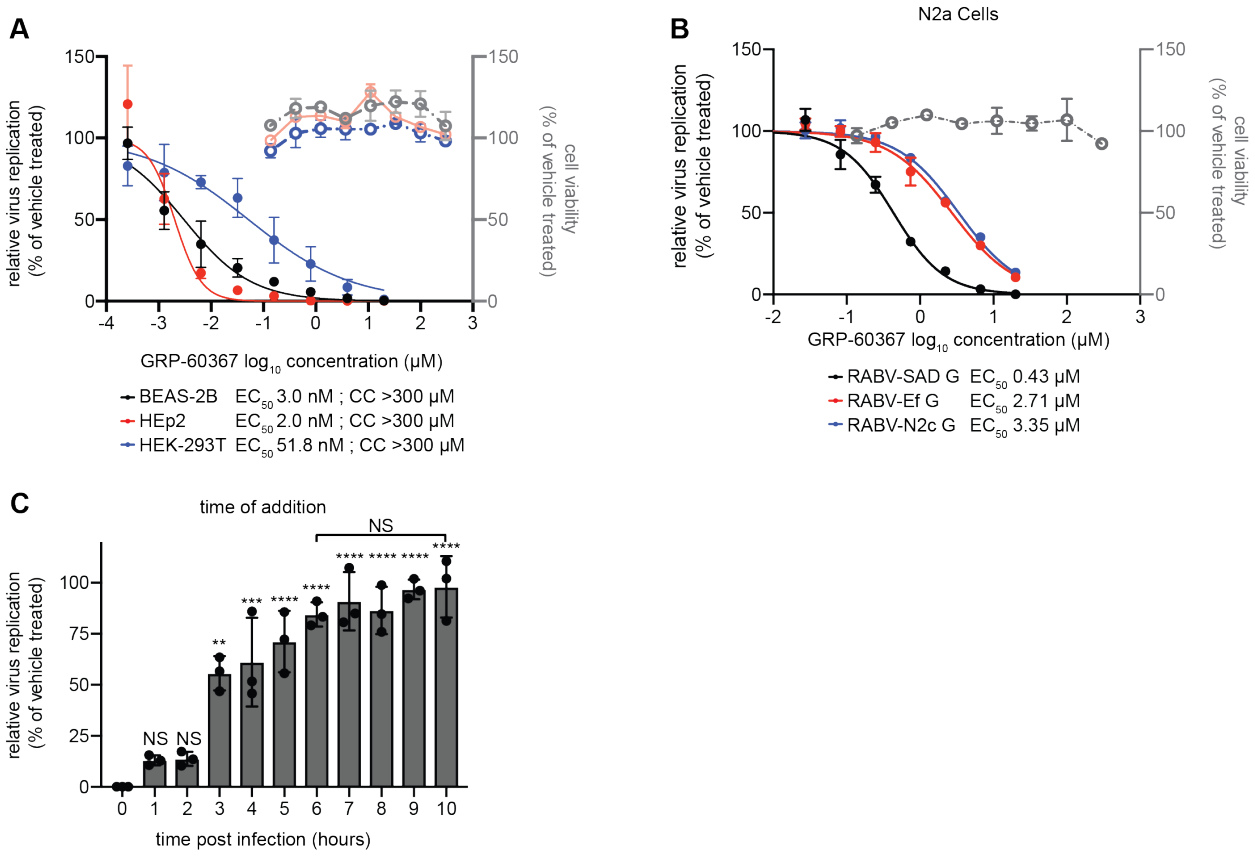

Figure 27. Mechanistic characterization of GRP-60367 **A)** dose-response inhibition curves of GRP-60367 within several cell lines: BEAS-2B (black, EC_{50} 3.0 nM), HEp2 (red, EC_{50} 2.0 nM), and HEK-293T (blue, EC_{50} 51.8 nM). Cell viability determined by Prestoblue substrate after 3 day incubation with 300μM concentration of GRP-60367 in multiple cell lines: BEAS-2B (black), HEp2 (blue), and HEK-293T (red) B) Determination of efficacy of GRP-60367 against G proteins from multiple RABV strains including the screening strain (SAD, black, EC_{50} 2.15 μM), a bat-derived strain (EF, red, EC_{50} 0.443 μM), and a mouse adapted neuronal strain (N2c, blue, EC_{50} 3.55 μM). Cytotoxicity of GRP-60367is denoted in green. C) Time of addition of GRP-60367 (10 μM) at specified times to determine efficacy over time post infection with RABV-ΔG-nanoLuc (red) and VSV-nanoLuc (black) in BEAS-2B cells.

1.3.7.3 Resistance Profiling by Viral Adaptation

In order to generate a resistance profile for GRP-60367, we exchanged VSV G for RABV G in a fully replication competent recombinant VSV virus genome background that also harbored GFP in a pre-L ORF position (**Figure 28A**). This virus was inhibited in a dose-dependent manner by GRP-60367 with an EC_{90} of 1.1 µM (**Figure 28B**). Adaptation to GRP-60367 was achieved through gradual increase of compound over time, until a concentration of 110 µM (100 x EC_{90}) was tolerated (**Figure 28C**). RT-PCR followed by Sanger sequencing of eight independently adapted lineages revealed several candidate mutations that mapped to the extracellular domain of G, and one early stop mutation in the G cytoplasmic domain (**Figure 28D**).

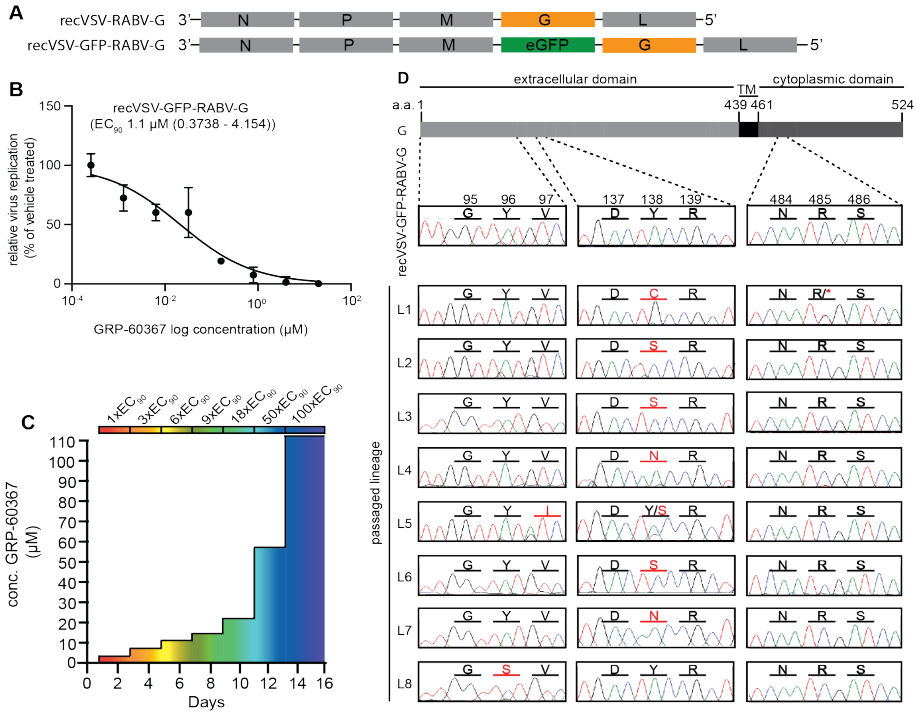

Figure 28*. Adaptation of recVSV-GFP-RABVG to GRP-60367* ***A)*** *schematic representation of recVSV-RABV-G without (top) and with GFP ORF (bottom). B) Dose-response inhibition of recVSV-GFP-RABV-G in the presence of GRP-60367* ***C)*** *Graphical representation of adaptation strategy.* ***C)*** *Mutations within 8 independently adapted viral lineages occurring within the G protein. Red amino acids represent observed mutations.*

Using a homology model generated based on the crystal structure of VSV G, all mutations were mapped to the fusion domain of RABV G (**Figure 29A**). Most adapted lineages emerged with a single point mutation located within the G fusion loops at amino acid Y138 that resulted in a change to serine, cysteine, or asparagine. Of the three point mutations, Y138S occurred the most frequently while Y138C and Y138N were found in one lineage each. Exchange of the resident tyrosine for these residues indicates a strong preference for polar groups within the fusion loops of G. The predominant Y138S is most likely favored due to a common hydroxyl group provided by the serine. We also identified two additional point mutations within the fusion loops located further upstream in the G polypeptide: Y96S and V97I. All mutations are relatively benign and most likely conferred resistance by maintaining the polar or hydrophobic micro-environment while at the same time indirectly reducing compound affinity through long-range effects [220]. We also detected a cytosine to thymine mutation within the intracellular domain of G that was located downstream of the transmembrane domain and resulted in an early stop mutation (R485*) and thus a truncated G protein.

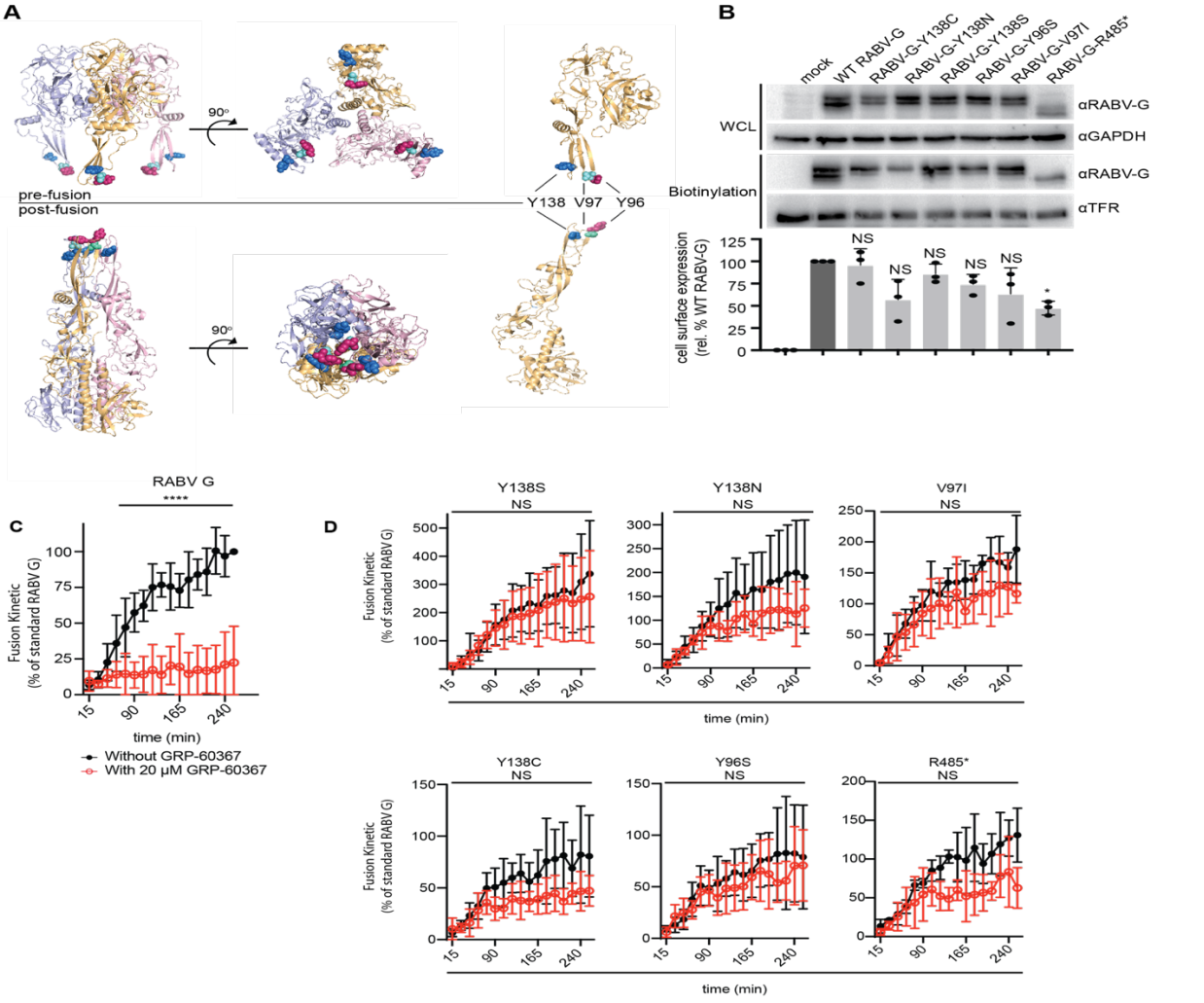

Figure 29. A) *Homology model of RABV G trimer based on the solved VSV G structures for pre-fusion (top) and post-fusion (bottom) (PDB:) Each monomer is individually colored (pink, gold, and lavender). Residues mutated from adaptation are indicated as colored spheres: Y138 (blue) V98 (green) and V97 (pink).* ***B)*** *Surface biotinylation of standard G and G escape mutants. G proteins were detected using αRABV-G and GAPDH was used as the loading control. Transferrin was detected for affirmation of biotinylation success. Relative cell surface expression as compared to standard G is graphically represented ±SD and based on 3 independent biological repeats.* ***C)*** *Kinetic fusion assay of G protein mutants based on renilla luciferase readout over four hours with >3 biological repeats.* ***D)*** *Kinetic fusion assay of G protein adaptation mutants incubated with GRP-60367 (20μM) over a four-hour period >3 biological repeats. Both kinetic fusion assays are expressed as percent of standard G renilla luciferase units at the four-hour timepoint. All statistical analyses through one-way ANOVA with Tukey's post hoc multiple comparison test. (NS, not significant; *, $p \leq 0.1$; ****: $p \leq 0.0001$).*

To further investigate their impact on G expression, we introduced each mutation into a standard G ORF After transient expression and subsequent surface biotinylation, we used densitometry of western blot protein bands to quantitatively compare relative cell membrane steady state levels (**Figure 29B**). All mutants, with the exception of R485*, were not significantly different from standard RABV G in cell surface expression. Interestingly, R485* had lower total expression, and its surface expression remained only 50% as compared to standard G. This result suggests inherent misfolding and internalization of this particular G mutant. Lowered expression of G has been shown to have little impact on pathogenicity or neurovirulence and part of the success of the current vaccine strain is overexpression of G to enhance antibody recognition [223]. For example, the higher neurovirulence of N2c as compared to B2c, a closely related and less pathogenic variant, is related to decreased surface G proteins [216, 223-225]. From these studies we can postulate that the R485* mutation causes long-range or direct changes in the compound binding pocket, yet most likely has very little impact on viral fitness.

Because the expression profiles exhibited by the other mutants (Y138C, Y138N, Y138S, Y96S, and V97I) rule out overexpression of G as a means of escape, we investigated the fusion rates of the mutants using a *Renilla* split-luciferase reporter assay. This assay relies on the reconstitution of bioactivity from two halves of the *Renilla* luciferase protein that can only trans-complement after a fusion event [29, 220, 226-228]. This was accomplished by transiently co-transfecting G mutants with an N-terminal *Renilla* fragment, while a second population of cells was independently transfected with the C-terminal fragment. After cell mixing and low pH induction, *Renilla* luciferase activity was monitored for four hours with readouts every 15 minutes using the Cytation5 automated high content imager **(Figure 29C, D)**. Only Y138S had

heightened fusion rates in the absence of compound at the four-hour timepoint, while the other mutants were not phenotypically distinct from standard G. In the presence of 20 μM compound, the Y138S mutant still had an accelerated fusion rate, and the Y138N and V97I mutations were not significantly hindered by compound as compared to standard G (Figure 29D). Enhancement of the fusion rate enables the Y138S mutant to escape by faster triggering of G protein fusion, thus narrowing the opportunity for compound interference. This mechanism of escape has been previously described for other viruses resistant to entry inhibitors and is often attributed to decreased, structural stability of the fusion machinery [220, 229]. Interestingly, the other mutations at Y138, Y96, and V97I did not result in an altered fusion rate (Figure 29D). This indicates that these mutants employ an alternative mode of escape, most likely a shift in the G structure that disrupts compound affinity.

1.3.8 Chapter 2 Discussion

The difficulty of access and cold-chain requirement of current RABV PEP treatment have underscored the unmet need for expanded therapeutic options against rabies disease. However, current containment requirements of RABV and lack of discernable cell culture cytopathic effect pose a challenge for the implementation of large-scale drug discovery efforts.

To address these obstacles, we generated a pseudo-typed Nano luciferase-expressing reporter RABV strain that is limited to single-cycle infection. RABV-ΔG-nanoLuc provides the distinct advantage of enabling quantitative assessment of viral inhibition in a BSL-2 laboratory setting. With our reporter strain, we successfully executed the first-ever high-throughput screening campaign targeting RABV with our open-discovery library comprised of over 150,000 small-molecule compounds.

Our HTS screen identified a novel first-in-class RABV inhibitor, GRP-60367, that demonstrated low nanomolar antiviral activity in multiple cell lines, including a neuronal cell line, without observable toxicity. Mechanistic characterization of GRP-60367 revealed that it blocks an early step in the viral lifecycle based on the dramatic loss of compound potency 2 hours post-infection based on time of addition studies. The role of GRP-60367 in blocking viral membrane fusion was further confirmed by engineering a cell-to-cell fusion assay that employed a dual-split luciferase reporter to quantify fusion events over time.

Direct-counter screening of GRP-60367 revealed dose-dependent inhibition of both mouse and bat RABV challenge strains in the micromolar range. However, the inhibition observed was 10-fold less potent as compared to the efficacy against the vaccine-derived screening strain. The decreased effectiveness of GRP-60367 could be attributed to strain-dependent variations in glycoprotein conformation that directly affect the structure of the candidate compound binding pocket. However, the low toxicity and chemical profile of GRP-60367 potentiates it as an ideal lead candidate scaffold for future structure-activity relationship optimization to obtain a broader indication spectrum.

Resistance profiling of GRP-60367 escape mutants revealed two mechanisms of escape. The mutants, Y138S, Y138N, and V97I, all exhibited a hyperactive fusion rate as compared to standard RABV G. Previously, several critical residues in RABV G encompassing residues 392-396 have been identified to regulate fusion activity. However, none of the escape mutations emerging in our virus adaptation study have been previously implicated in this role [188, 194-196, 230, 231]. Homology modeling of RABV G based on the solved VSV G structure revealed that residues Y96, V97, and Y138, reside within the tips of the fusion loops, which are released to anchor into the target membrane [232]. Though Y96S seems to have little effect on the fusion

kinetics, the enhanced fusion rate of the Y138S mutation suggests a dominant role in determining the fusion rate. Synonymous mutations of analogous fusion peptides of several viruses of *Paramyxoviridae* have also demonstrated accelerated fusion rates [233-236]. As with *Paramyxoviridae*, it is possible that the residues identified here may also regulate the kinetic barrier for membrane fusion and that the escape mutations destabilize G to promote triggering of the fusion machinery. Mutations within the fusion loops of closely related VSV have resulted in abrogated fusion activity by changing side chains to hydrophobic amino acids. These mutations caused destabilization of the interaction between fatty acid chains and head groups of lipids [191, 232, 237, 238]. In contrast, the acquired mutations from GRP-60367 may stabilize the lipid interaction to facilitate pore formation.

Interestingly, mutants Y138C, Y96S, and the early stop mutation demonstrated similar fusion rates compared to standard G despite proximity to the previous mutations. Modification of these residues without resulting in altered entry kinetic implicate this region either as the primary compound binding site or that these mutations directly alter the binding pocket. Several N-linked glycosylation sites containing the motif Asn-X-Ser/Thr were previously identified in RABV G [239]. Mutation of residue Y96 to serine completes this motif for an upstream asparagine. Therefore, it is tempting to postulate glycosylation as a means of escape, especially since the introduction of N-glycans can improve virus production for street RABV in neuronal cell lines [240, 241]. Truncation of the cytoplasmic tail of gp41 of HIV-1 has been shown to have long-ranging conformational effects that modulate ectodomain antigenicity at the cost of surface expression. Although surface expression of the RABV G truncated mutant was similarly decreased, it appeared not to affect viral entry. Lowered expression of G has little impact on pathogenicity or neurovirulence, and part of the success of the current vaccine strain is

overexpression of G to enhance antibody recognition [223]. For example, the higher neurovirulence of N2c as compared to B2c, a closely related and less pathogenic variant, is connected to decreased surface G proteins [126, 216, 223-225]. Based on our data, we can postulate that the R485* mutation causes long-range changes to the compound binding pocket in the ectodomain without affecting viral fitness.

Here we have provided a proof-of-concept framework for future anti-RABV HTS campaigns, developed a reliable and safe RABV reporter strain, and identified a potent and newly characterized first-in-class RABV entry inhibitor that emerged from our screen. All of the mutations identified from the adaptation studies have not been previously characterized by epitope mapping, suggesting GRP-60367 occupies a novel druggable pocket [194-196, 231, 242]. Although the exact mechanism of inhibition by GRP-60367 remains unclear, it was instrumental in identifying Y138 as a critical residue for entry mechanics. Therefore, GRP-60367 is a viable tool that can lead to further mechanistic understanding of class III fusion protein entry paving the way for better informed drug discovery against RABV.

2 Conclusions

2.1 Chapter 1 Conclusions

We have advanced the current understanding of the underlying mechanism of paramyxovirus RdRp movement along the encapsidated genome, a previously poorly understood process, by identifying and characterizing the interactions between the core RdRP constituents. This discovery was accomplished by identifying two microdomains within P for L binding. One microdomain is a highly conserved region proximal to the oligomerization domain (OD), that we predicted to serve as an anchor for L. The second contact point consists of a previously unassigned face of the PXD triangular prism. Our innovative approach of using functional trans-complementation assays between P mutants allowed us to determine the stoichiometric relationship between PXD:L and PXD:MoRE interactions, and enabled us to appreciate a regulatory role of PXD in RdRP negotiation of the viral template. Based on these discoveries, we have proposed a novel mechanistic model that posits RdRP advancement along the genomic template regulated by PXD competition for L binding. The discovery of this dynamic interaction of PXD with L has not only furthered our understanding of how the viral polymerase negotiates and regulates advancement along the genomic template, but also highlighted a potential druggable target. Because of the conserved structural homology between the polymerase assemblies of the *Paramyxoviridae*, we propose that our discovery of the PXD:L interface could serve as a valid antiviral platform for drug development against emerging viruses within the family, such as zoonotic NiV, against which currently no vaccine or antiviral treatment exists.

2.2 Chapter 2 Conclusions

We have successfully developed and implemented an innovative high-throughput cell-based drug screening protocol using a first-in-class reporter strain of RABV that is capable only

of a single round of infection. From this screen, we have identified a novel direct-acting RABV entry inhibitor, GRP-60367, that exhibits low nanomolar efficacy with a CC_{50} >300 mM in all cell lines tested. Resistance profiling revealed a previously uncharacterized amino acid, Y138, that serves as a determinant for RABV G fusion kinetics. GRP-60367 may serve as a much-needed innovative molecular point of entry for better characterization of the mechanics of currently still understudied type III viral fusion proteins

3 REFERENCES

1. Lamb, R.A., *Mononegavirales*, in *Fields Virology*, D.M.K.P.M. Howley, Editor. 2013, Lippincott Williams & Wilkins: Philadelphia, PA. p. 880-884.
2. Smallwood, S. and S.A. Moyer, *Promoter analysis of the vesicular stomatitis virus RNA polymerase.* Virology, 1993. **192**(1): p. 254-63.
3. Iverson, L.E. and J.K. Rose, *Localized attenuation and discontinuous synthesis during vesicular stomatitis virus transcription.* Cell, 1981. **23**(2): p. 477-84.
4. Ogino, T. and A.K. Banerjee, *Unconventional mechanism of mRNA capping by the RNA-dependent RNA polymerase of vesicular stomatitis virus.* Mol Cell, 2007. **25**(1): p. 85-97.
5. Ogino, T. and T.J. Green, *RNA Synthesis and Capping by Non-segmented Negative Strand RNA Viral Polymerases: Lessons From a Prototypic Virus.* Front Microbiol, 2019. **10**: p. 1490.
6. Furuichi, Y. and A.J. Shatkin, *Viral and cellular mRNA capping: past and prospects.* Adv Virus Res, 2000. **55**: p. 135-84.
7. O'Brien, K.L., T. Nolan, and S.W.o. Rabies, *The WHO position on rabies immunization - 2018 updates.* Vaccine, 2018.
8. Angelo, K.M., et al., *Spread of Measles in Europe and Implications for US Travelers.* Pediatrics, 2019. **144**(1).
9. Guerra, F.M., et al., *The basic reproduction number (R0) of measles: a systematic review.* Lancet Infect Dis, 2017. **17**(12): p. e420-e428.
10. Patterson, J.B., M. Manchester, and M.B. Oldstone, *Disease model: dissecting the pathogenesis of the measles virus.* Trends Mol Med, 2001. **7**(2): p. 85-8.
11. Gokiert, J.G. and W.E. Beamish, *Altered reactivity to measles virus in previously vaccinated children.* Can Med Assoc J, 1970. **103**(7): p. 724-7.
12. Rammohan, K.W., H.F. McFarland, and D.E. McFarlin, *Subacute sclerosing panencephalitis after passive immunization and natural measles infection: role of antibody in persistence of measles virus.* Neurology, 1982. **32**(4): p. 390-4.
13. Norrby, E. and K. Kristensson, *Measles virus in the brain.* Brain Res Bull, 1997. **44**(3): p. 213-20.
14. Angius, F., et al., *Analysis of a Subacute Sclerosing Panencephalitis Genotype B3 Virus from the 2009-2010 South African Measles Epidemic Shows That Hyperfusogenic F Proteins Contribute to Measles Virus Infection in the Brain.* J Virol, 2019. **93**(4).
15. Mathieu, C., et al., *Measles Virus Bearing Measles Inclusion Body Encephalitis-Derived Fusion Protein Is Pathogenic after Infection via the Respiratory Route.* J Virol, 2019. **93**(8).
16. Kweder, H., et al., *Measles Virus: Identification in the M Protein Primary Sequence of a Potential Molecular Marker for Subacute Sclerosing Panencephalitis.* Adv Virol, 2015. **2015**: p. 769837.
17. Mina, M.J., et al., *Long-term measles-induced immunomodulation increases overall childhood infectious disease mortality.* Science, 2015. **348**(6235): p. 694-9.

18. Centers for Disease, C. and Prevention, *Postexposure prophylaxis, isolation, and quarantine to control an import-associated measles outbreak--Iowa, 2004.* MMWR Morb Mortal Wkly Rep, 2004. **53**(41): p. 969-71.
19. McLean, H.Q., et al., *Prevention of measles, rubella, congenital rubella syndrome, and mumps, 2013: summary recommendations of the Advisory Committee on Immunization Practices (ACIP).* MMWR Recomm Rep, 2013. **62**(RR-04): p. 1-34.
20. Gastanaduy, P.A., et al., *Public health responses during measles outbreaks in elimination settings: Strategies and challenges.* Hum Vaccin Immunother, 2018. **14**(9): p. 2222-2238.
21. Barnard, D.L., *Inhibitors of measles virus.* Antivir Chem Chemother, 2004. **15**(3): p. 111-9.
22. Jeulin, H., et al., *In vivo antiviral activity of ribavirin/alpha-cyclodextrin complex: evaluation on experimental measles virus encephalitis in mice.* Int J Pharm, 2008. **357**(1-2): p. 148-53.
23. Pal, G., *Effects of ribavirin on measles.* J Indian Med Assoc, 2011. **109**(9): p. 666-7.
24. Barnard, D.L., et al., *Inhibition of measles virus replication by 5'-nor carbocyclic adenosine analogues.* Antivir Chem Chemother, 2001. **12**(4): p. 241-50.
25. Barnard, D.L., et al., *Coumarins and pyranocoumarins, potential novel pharmacophores for inhibition of measles virus replication.* Antivir Chem Chemother, 2002. **13**(1): p. 39-59.
26. Zhang, N., et al., *in vitro inhibition of the measles virus by novel ring-expanded ('fat') nucleoside analogues containing the imidazo[4,5-e]diazepine ring system.* Bioorg Med Chem Lett, 2002. **12**(23): p. 3391-4.
27. Elia, G., et al., *In vitro efficacy of ribavirin against canine distemper virus.* Antiviral Res, 2008. **77**(2): p. 108-13.
28. Jeulin, H., et al., *Effective ribavirin concentration in mice brain using cyclodextrin as a drug carrier: evaluation in a measles encephalitis model.* Antiviral Res, 2009. **81**(3): p. 261-6.
29. Sun, A., et al., *Nonpeptide inhibitors of measles virus entry.* J Med Chem, 2006. **49**(17): p. 5080-92.
30. Sun, A., et al., *Non-nucleoside inhibitors of the measles virus RNA-dependent RNA polymerase complex activity: Synthesis and in vitro evaluation.* Bioorg Med Chem Lett, 2007. **17**(18): p. 5199-203.
31. White, L.K., et al., *Nonnucleoside inhibitor of measles virus RNA-dependent RNA polymerase complex activity.* Antimicrob Agents Chemother, 2007. **51**(7): p. 2293-303.
32. Krumm, S.A., et al., *An orally available, small-molecule polymerase inhibitor shows efficacy against a lethal morbillivirus infection in a large animal model.* Sci Transl Med, 2014. **6**(232): p. 232ra52.
33. Mathieu, C., et al., *Prevention of measles virus infection by intranasal delivery of fusion inhibitor peptides.* J Virol, 2015. **89**(2): p. 1143-55.
34. Plemper, R.K. and R.M. Cox, *Biology must develop herd immunity against bad-actor molecules.* PLoS Pathog, 2018. **14**(6): p. e1007038.
35. Sourimant, J. and R.K. Plemper, *Organization, Function, and Therapeutic Targeting of the Morbillivirus RNA-Dependent RNA Polymerase Complex.* Viruses, 2016. **8**(9).

36. Parks, R.A.L.a.G.D., *Paramyxoviridae*, in *Fields Virology*, D.M.K.a.P.M. Howley, Editor. 2013, Lippincott williams and wilkins: Philadelphia PA. p. 957-995.
37. White, J.M., et al., *Structures and mechanisms of viral membrane fusion proteins: multiple variations on a common theme.* Crit Rev Biochem Mol Biol, 2008. **43**(3): p. 189-219.
38. Hashiguchi, T., et al., *Crystal structure of measles virus hemagglutinin provides insight into effective vaccines.* Proc Natl Acad Sci U S A, 2007. **104**(49): p. 19535-40.
39. Plemper, R.K., A.L. Hammond, and R. Cattaneo, *Measles virus envelope glycoproteins hetero-oligomerize in the endoplasmic reticulum.* J Biol Chem, 2001. **276**(47): p. 44239-46.
40. Plemper, R.K., M.A. Brindley, and R.M. Iorio, *Structural and mechanistic studies of measles virus illuminate paramyxovirus entry.* PLoS Pathog, 2011. **7**(6): p. e1002058.
41. Brindley, M.A., S. Chaudhury, and R.K. Plemper, *Measles virus glycoprotein complexes preassemble intracellularly and relax during transport to the cell surface in preparation for fusion.* J Virol, 2015. **89**(2): p. 1230-41.
42. Hsu, E.C., et al., *CDw150(SLAM) is a receptor for a lymphotropic strain of measles virus and may account for the immunosuppressive properties of this virus.* Virology, 2001. **279**(1): p. 9-21.
43. Schneider-Schaulies, J., et al., *Receptor usage and differential downregulation of CD46 by measles virus wild-type and vaccine strains.* Proc Natl Acad Sci U S A, 1995. **92**(9): p. 3943-7.
44. Manchester, M., et al., *Multiple isoforms of CD46 (membrane cofactor protein) serve as receptors for measles virus.* Proc Natl Acad Sci U S A, 1994. **91**(6): p. 2161-5.
45. Baker, K.A., et al., *Structural basis for paramyxovirus-mediated membrane fusion.* Mol Cell, 1999. **3**(3): p. 309-19.
46. Plemper, R.K. and R.W. Compans, *Mutations in the putative HR-C region of the measles virus F2 glycoprotein modulate syncytium formation.* J Virol, 2003. **77**(7): p. 4181-90.
47. Brindley, M.A., et al., *A stabilized headless measles virus attachment protein stalk efficiently triggers membrane fusion.* J. Virol., 2013. **87**: p. 11693-11703.
48. Plumet, S., W.P. Duprex, and D. Gerlier, *Dynamics of viral RNA synthesis during measles virus infection.* J Virol, 2005. **79**(11): p. 6900-8.
49. Salditt, A., et al., *Measles virus M protein-driven particle production does not involve the endosomal sorting complex required for transport (ESCRT) system.* J Gen Virol, 2010. **91**(Pt 6): p. 1464-72.
50. Harrison, M.S., T. Sakaguchi, and A.P. Schmitt, *Paramyxovirus assembly and budding: building particles that transmit infections.* Int J Biochem Cell Biol, 2010. **42**(9): p. 1416-29.
51. Votteler, J. and W.I. Sundquist, *Virus budding and the ESCRT pathway.* Cell Host Microbe, 2013. **14**(3): p. 232-41.
52. Fearns, R. and R.K. Plemper, *Polymerases of paramyxoviruses and pneumoviruses.* Virus Res, 2017. **234**: p. 87-102.
53. Cattaneo, R., et al., *Altered transcription of a defective measles virus genome derived from a diseased human brain.* EMBO J, 1987. **6**(3): p. 681-8.

54. Harty, R.N. and P. Palese, *Measles virus phosphoprotein (P) requires the NH2- and COOH-terminal domains for interactions with the nucleoprotein (N) but only the COOH terminus for interactions with itself.* J Gen Virol, 1995. **76 (Pt 11)**: p. 2863-7.
55. Kolakofsky, D., et al., *Viral DNA polymerase scanning and the gymnastics of Sendai virus RNA synthesis.* Virology, 2004. **318**(2): p. 463-73.
56. Guryanov, S.G., et al., *Crystal Structure of the Measles Virus Nucleoprotein Core in Complex with an N-Terminal Region of Phosphoprotein.* J Virol, 2015. **90**(6): p. 2849-57.
57. Gutsche, I., et al., *Near-atomic cryo-EM structure of the helical measles virus nucleocapsid.* Science, 2015. **348**(6235): p. 704-707.
58. Jensen, M.R., et al., *Intrinsic disorder in measles virus nucleocapsids.* Proc Natl Acad Sci U S A, 2011. **108**(24): p. 9839-44.
59. Bourhis, J.M., et al., *The intrinsically disordered C-terminal domain of the measles virus nucleoprotein interacts with the C-terminal domain of the phosphoprotein via two distinct sites and remains predominantly unfolded.* Protein Science, 2005. **14**(8): p. 1975-1992.
60. Karlin, D., S. Longhi, and B. Canard, *Substitution of two residues in the measles virus nucleoprotein results in an impaired self-association.* Virology, 2002. **302**(2): p. 420-32.
61. Bankamp, B., et al., *Domains of the measles virus N protein required for binding to P protein and self-assembly.* Virology, 1996. **216**(1): p. 272-7.
62. Communie, G., et al., *Atomic resolution description of the interaction between the nucleoprotein and phosphoprotein of Hendra virus.* PLoS Pathog, 2013. **9**(9): p. e1003631.
63. Schoehn, G., et al., *The 12 A structure of trypsin-treated measles virus N-RNA.* J Mol Biol, 2004. **339**(2): p. 301-12.
64. Shu, Y., et al., *Plasticity in structural and functional interactions between the phosphoprotein and nucleoprotein of measles virus.* J Biol Chem, 2012. **287**(15): p. 11951-67.
65. Wang, Y., et al., *Multiscaled exploration of coupled folding and binding of an intrinsically disordered molecular recognition element in measles virus nucleoprotein.* Proc Natl Acad Sci U S A, 2013. **110**(40): p. E3743-52.
66. Brunel, J., et al., *Sequence of events in measles virus replication: role of phosphoprotein-nucleocapsid interactions.* J Virol, 2014. **88**(18): p. 10851-63.
67. Bloyet, L.M., et al., *Modulation of Re-initiation of Measles Virus Transcription at Intergenic Regions by PXD to NTAIL Binding Strength.* PLoS Pathog, 2016. **12**(12): p. e1006058.
68. Gruet, A., et al., *Dissecting partner recognition by an intrinsically disordered protein using descriptive random mutagenesis.* J Mol Biol, 2013. **425**(18): p. 3495-509.
69. Communie, G., et al., *Intrinsically disordered proteins implicated in paramyxoviral replication machinery.* Curr Opin Virol, 2014. **5**: p. 72-81.
70. Bonetti, D., et al., *Analyzing the Folding and Binding Steps of an Intrinsically Disordered Protein by Protein Engineering.* Biochemistry, 2017. **56**(29): p. 3780-3786.
71. Krumm, S.A., M. Takeda, and R.K. Plemper, *The Measles Virus Nucleocapsid Protein Tail Domain Is Dispensable for Viral Polymerase Recruitment and Activity.* Journal of Biological Chemistry, 2013. **288**(41): p. 29943-29953.

72. Thakkar, V.D., et al., *The Unstructured Paramyxovirus Nucleocapsid Protein Tail Domain Modulates Viral Pathogenesis through Regulation of Transcriptase Activity.* J Virol, 2018. **92**(8).
73. Cox, R.M., et al., *The structurally disordered paramyxovirus nucleocapsid protein tail domain is a regulator of the mRNA transcription gradient.* Sci Adv, 2017. **3**(2): p. e1602350.
74. Cevik, B., et al., *The phosphoprotein (P) and L binding sites reside in the N-terminus of the L subunit of the measles virus RNA polymerase.* Virology, 2004. **327**(2): p. 297-306.
75. Horikami, S.M., et al., *An amino-proximal domain of the L protein binds to the P protein in the measles virus RNA polymerase complex.* Virology, 1994. **205**(2): p. 540-5.
76. Malur, A.G., et al., *Analysis of the mutations in the active site of the RNA-dependent RNA polymerase of human parainfluenza virus type 3 (HPIV3).* Gene Expr, 2002. **10**(3): p. 93-100.
77. Gopinath, M. and M.S. Shaila, *Evidence for N(7) guanine methyl transferase activity encoded within the modular domain of RNA-dependent RNA polymerase L of a Morbillivirus.* Virus Genes, 2015. **51**(3): p. 356-60.
78. Nishio, M., et al., *Human parainfluenza virus type 2 L protein regions required for interaction with other viral proteins and mRNA capping.* J Virol, 2011. **85**(2): p. 725-32.
79. Duprex, W.P., F.M. Collins, and B.K. Rima, *Modulating the function of the measles virus RNA-dependent RNA polymerase by insertion of green fluorescent protein into the open reading frame.* Journal of Virology, 2002. **76**(14): p. 7322-7328.
80. Dochow, M., et al., *Independent structural domains in paramyxovirus polymerase protein.* J Biol Chem, 2012. **287**(9): p. 6878-91.
81. Gilman, M.S.A., et al., *Structure of the Respiratory Syncytial Virus Polymerase Complex.* Cell, 2019. **179**(1): p. 193-204 e14.
82. Liang, B., et al., *Structure of the L Protein of Vesicular Stomatitis Virus from Electron Cryomicroscopy.* Cell, 2015. **162**(2): p. 314-327.
83. Tao, Y., et al., *RNA synthesis in a cage--structural studies of reovirus polymerase lambda3.* Cell, 2002. **111**(5): p. 733-45.
84. Rahmeh, A.A., et al., *Critical phosphoprotein elements that regulate polymerase architecture and function in vesicular stomatitis virus.* Proc Natl Acad Sci U S A, 2012. **109**(36): p. 14628-33.
85. Guryanov, S.G., et al., *Crystal Structure of the Measles Virus Nucleoprotein Core in Complex with an N-Terminal Region of Phosphoprotein.* Journal of Virology, 2016. **90**(6): p. 2849-2857.
86. Communie, G., et al., *Structure of the tetramerization domain of measles virus phosphoprotein.* J Virol, 2013. **87**(12): p. 7166-9.
87. Johansson, K., et al., *Crystal structure of the measles virus phosphoprotein domain responsible for the induced folding of the C-terminal domain of the nucleoprotein.* J Biol Chem, 2003. **278**(45): p. 44567-73.
88. Karlin, D. and R. Belshaw, *Detecting remote sequence homology in disordered proteins: discovery of conserved motifs in the N-termini of Mononegavirales phosphoproteins.* PLoS One, 2012. **7**(3): p. e31719.

89. Yabukarski, F., et al., *Structure of Nipah virus unassembled nucleoprotein in complex with its viral chaperone.* Nat Struct Mol Biol, 2014. **21**(9): p. 754-9.
90. Leyrat, C., et al., *Structure of the vesicular stomatitis virus N(0)-P complex.* PLoS Pathog, 2011. **7**(9): p. e1002248.
91. Bruhn, J.F., et al., *Crystal structure of the nipah virus phosphoprotein tetramerization domain.* J Virol, 2014. **88**(1): p. 758-62.
92. Bruhn, J.F., et al., *A Conserved Basic Patch and Central Kink in the Nipah Virus Phosphoprotein Multimerization Domain Are Essential for Polymerase Function.* Structure, 2019.
93. Bloyet, L.M., et al., *Regulation of measles virus gene expression by P protein coiled-coil properties.* Sci Adv, 2019. **5**(5): p. eaaw3702.
94. Blocquel, D., et al., *Coiled-coil deformations in crystal structures: the measles virus phosphoprotein multimerization domain as an illustrative example.* Acta Crystallographica. Section D, Biological Crystallography, 2014. **70**(Pt 6): p. 1589-1603.
95. Dosnon, M., et al., *Demonstration of a folding after binding mechanism in the recognition between the measles virus NTAIL and X domains.* ACS Chem Biol, 2015. **10**(3): p. 795-802.
96. Kingston, R.L., et al., *Structural basis for the attachment of a paramyxoviral polymerase to its template.* Proc Natl Acad Sci U S A, 2004. **101**(22): p. 8301-6.
97. Gruet, A., et al., *Fuzzy regions in an intrinsically disordered protein impair protein-protein interactions.* FEBS J, 2016. **283**(4): p. 576-94.
98. Gely, S., et al., *Solution structure of the C-terminal X domain of the measles virus phosphoprotein and interaction with the intrinsically disordered C-terminal domain of the nucleoprotein.* Journal of Molecular Recognition, 2010. **23**(5): p. 435-447.
99. Liston, P., C. Diflumeri, and D.J. Briedis, *Protein Interactions Entered into by the Measles-Virus P-Proteins, V-Proteins, and C-Proteins.* Virus Research, 1995. **38**(2-3): p. 241-259.
100. Chattopadhyay, A. and M.S. Shaila, *Rinderpest virus RNA polymerase subunits: Mapping of mutual interacting domains on the Large protein L and Phosphoprotein P.* Virus Genes, 2004. **28**(2): p. 169-178.
101. Saikia, P. and M.S. Shaila, *Identification of functional domains of phosphoproteins of two morbilliviruses using chimeric proteins.* Virus Genes, 2008. **37**(1): p. 1-8.
102. Bloyet, L.M., et al., *HSP90 Chaperoning in Addition to Phosphoprotein Required for Folding but Not for Supporting Enzymatic Activities of Measles and Nipah Virus L Polymerases.* J Virol, 2016. **90**(15): p. 6642-6656.
103. Geller, R., R. Andino, and J. Frydman, *Hsp90 inhibitors exhibit resistance-free antiviral activity against respiratory syncytial virus.* PLoS One, 2013. **8**(2): p. e56762.
104. Smith, D.R., et al., *Inhibition of heat-shock protein 90 reduces Ebola virus replication.* Antiviral Res, 2010. **87**(2): p. 187-94.
105. Connor, J.H., et al., *Antiviral activity and RNA polymerase degradation following Hsp90 inhibition in a range of negative strand viruses.* Virology, 2007. **362**(1): p. 109-19.
106. Krumm, S.A., M. Takeda, and R.K. Plemper, *The measles virus nucleocapsid protein tail domain is dispensable for viral polymerase recruitment and activity.* J Biol Chem, 2013. **288**(41): p. 29943-53.

107. Doyle, J., et al., *Two domains that control prefusion stability and transport competence of the measles virus fusion protein.* J Virol, 2006. **80**(3): p. 1524-36.
108. Chan, W.M., et al., *How many mutant p53 molecules are needed to inactivate a tetramer?* Mol Cell Biol, 2004. **24**(8): p. 3536-51.
109. Rima, B.K. and W.P. Duprex, *New concepts in measles virus replication: getting in and out in vivo and modulating the host cell environment.* Virus Res, 2011. **162**(1-2): p. 47-62.
110. Blocquel, D., et al., *Compaction and binding properties of the intrinsically disordered C-terminal domain of Henipavirus nucleoprotein as unveiled by deletion studies.* Mol Biosyst, 2012. **8**(1): p. 392-410.
111. Harbury, P.B., et al., *A switch between two-, three-, and four-stranded coiled coils in GCN4 leucine zipper mutants.* Science, 1993. **262**(5138): p. 1401-7.
112. Bloyet, L.M., et al., *Modulation of Re-initiation of Measles Virus Transcription at Intergenic Regions by P-XD to N-TAIL Binding Strength.* Plos Pathogens, 2016. **12**(12).
113. Radecke, F., et al., *Rescue of measles viruses from cloned DNA.* EMBO J, 1995. **14**(23): p. 5773-84.
114. Schrag, S.J., P.A. Rota, and W.J. Bellini, *Spontaneous mutation rate of measles virus: direct estimation based on mutations conferring monoclonal antibody resistance.* J Virol, 1999. **73**(1): p. 51-4.
115. Kolakofsky, D., *Paramyxovirus RNA synthesis, mRNA editing, and genome hexamer phase: A review.* Virology, 2016. **498**: p. 94-98.
116. Kolakofsky, D., et al., *Viral RNA polymerase scanning and the gymnastics of Sendai virus RNA synthesis.* Virology, 2004. **318**(2): p. 463-473.
117. Morin, B., et al., *The polymerase of negative-stranded RNA viruses.* Curr Opin Virol, 2013. **3**(2): p. 103-10.
118. Longhi, S., et al., *How order and disorder within paramyxoviral nucleoproteins and phosphoproteins orchestrate the molecular interplay of transcription and replication.* Cellular and Molecular Life Sciences, 2017. **74**(17): p. 3091-3118.
119. World Health, O., *Rabies vaccines: WHO position paper, April 2018 - Recommendations.* Vaccine, 2018. **36**(37): p. 5500-5503.
120. Gillet, J.P., P. Derer, and H. Tsiang, *Axonal transport of rabies virus in the central nervous system of the rat.* J Neuropathol Exp Neurol, 1986. **45**(6): p. 619-34.
121. Singh, R., et al., *Rabies - epidemiology, pathogenesis, public health concerns and advances in diagnosis and control: a comprehensive review.* Vet Q, 2017. **37**(1): p. 212-251.
122. Shlim, D.R., *Preventing rabies: the new WHO recommendations and their impact on travel medicine practice.* J Travel Med, 2018. **25**(1).
123. Tawanwongsri, W. and P. Wattanakrai, *Serum Sickness after Equine Rabies Immunoglobulin in Identical Male Twins: Two Case Reports.* Case Rep Dermatol, 2019. **11**(1): p. 40-47.
124. Sirikun, J., et al., *Immunogenic response in obese patients undergoing rabies post-exposure prophylaxis with combined equine rabies immunoglobulin and rabies vaccination.* Vaccine, 2018. **36**(2): p. 285-291.

125. Lang, J., et al., *Evaluation of the safety, immunogenicity, and pharmacokinetic profile of a new, highly purified, heat-treated equine rabies immunoglobulin, administered either alone or in association with a purified, Vero-cell rabies vaccine.* Acta Trop, 1998. **70**(3): p. 317-33.
126. Badrane, H., et al., *Evidence of two Lyssavirus phylogroups with distinct pathogenicity and immunogenicity.* J Virol, 2001. **75**(7): p. 3268-76.
127. Du Pont, V., R.K. Plemper, and M.J. Schnell, *Status of antiviral therapeutics against rabies virus and related emerging lyssaviruses.* Curr Opin Virol, 2019. **35**: p. 1-13.
128. Douglas S. Lyles, I.V.K., and Charles E. Rupprecht, *Rhabdoviridae*, in *Fields Virology*, a.P.M.H. David M. Knipe, Editor. 2013, Lippincott Williams and Wilkens: Philadelphia, PA. p. 885-922.
129. Ge, P., et al., *Cryo-EM model of the bullet-shaped vesicular stomatitis virus.* Science, 2010. **327**(5966): p. 689-93.
130. Guo, Y., et al., *Early events in rabies virus infection-Attachment, entry, and intracellular trafficking.* Virus Res, 2019. **263**: p. 217-225.
131. Lafon, M., *Rabies virus receptors.* J Neurovirol, 2005. **11**(1): p. 82-7.
132. Piccinotti, S. and S.P. Whelan, *Rabies Internalizes into Primary Peripheral Neurons via Clathrin Coated Pits and Requires Fusion at the Cell Body.* PLoS Pathog, 2016. **12**(7): p. e1005753.
133. Piccinotti, S., T. Kirchhausen, and S.P. Whelan, *Uptake of rabies virus into epithelial cells by clathrin-mediated endocytosis depends upon actin.* J Virol, 2013. **87**(21): p. 11637-47.
134. Gaudin, Y., et al., *Low-pH conformational changes of rabies virus glycoprotein and their role in membrane fusion.* J Virol, 1993. **67**(3): p. 1365-72.
135. Gaudin, Y., et al., *Reversible conformational changes and fusion activity of rabies virus glycoprotein.* J Virol, 1991. **65**(9): p. 4853-9.
136. Miyamoto, K. and S. Matsumoto, *The nature of the Negri body.* J Cell Biol, 1965. **27**(3): p. 677-82.
137. Covell, W.P. and W.B. Danks, *Studies on the Nature of the Negri Body.* Am J Pathol, 1932. **8**(5): p. 557-572 3.
138. Finke, S., J.H. Cox, and K.K. Conzelmann, *Differential transcription attenuation of rabies virus genes by intergenic regions: generation of recombinant viruses overexpressing the polymerase gene.* J Virol, 2000. **74**(16): p. 7261-9.
139. Wu, X., et al., *Both viral transcription and replication are reduced when the rabies virus nucleoprotein is not phosphorylated.* J Virol, 2002. **76**(9): p. 4153-61.
140. Yang, J., et al., *Phosphorylation of rabies virus nucleoprotein regulates viral RNA transcription and replication by modulating leader RNA encapsidation.* J Virol, 1999. **73**(2): p. 1661-4.
141. Finke, S. and K.K. Conzelmann, *Dissociation of rabies virus matrix protein functions in regulation of viral RNA synthesis and virus assembly.* J Virol, 2003. **77**(22): p. 12074-82.
142. Finke, S., R. Mueller-Waldeck, and K.K. Conzelmann, *Rabies virus matrix protein regulates the balance of virus transcription and replication.* J Gen Virol, 2003. **84**(Pt 6): p. 1613-21.
143. Mebatsion, T., M. Konig, and K.K. Conzelmann, *Budding of rabies virus particles in the absence of the spike glycoprotein.* Cell, 1996. **84**(6): p. 941-51.

144. Willoughby, R.E., Jr., et al., *Survival after treatment of rabies with induction of coma.* N Engl J Med, 2005. **352**(24): p. 2508-14.
145. Lampejo, T., et al., *Caring for a patient with rabies: implications of the Milwaukee protocol for infection control and public health measures.* J Hosp Infect, 2017. **96**(4): p. 385-391.
146. Zeiler, F.A. and A.C. Jackson, *Critical Appraisal of the Milwaukee Protocol for Rabies: This Failed Approach Should Be Abandoned.* Can J Neurol Sci, 2016. **43**(1): p. 44-51.
147. Wilde, H. and T. Hemachudha, *The "Milwaukee protocol" for treatment of human rabies is no longer valid.* Pediatr Infect Dis J, 2015. **34**(6): p. 678-9.
148. Aramburo, A., et al., *Failure of the Milwaukee protocol in a child with rabies.* Clin Infect Dis, 2011. **53**(6): p. 572-4.
149. Rubin, J., et al., *Applying the Milwaukee protocol to treat canine rabies in Equatorial Guinea.* Scand J Infect Dis, 2009. **41**(5): p. 372-5.
150. Crance, J.M., et al., *Interferon, ribavirin, 6-azauridine and glycyrrhizin: antiviral compounds active against pathogenic flaviviruses.* Antiviral Res, 2003. **58**(1): p. 73-9.
151. Enria, D.A. and J.I. Maiztegui, *Antiviral treatment of Argentine hemorrhagic fever.* Antiviral Res, 1994. **23**(1): p. 23-31.
152. Hosoya, M., et al., *High-dose intravenous ribavirin therapy for subacute sclerosing panencephalitis.* Antimicrob Agents Chemother, 2001. **45**(3): p. 943-5.
153. Huggins, J.W., R.K. Robins, and P.G. Canonico, *Synergistic antiviral effects of ribavirin and the C-nucleoside analogs tiazofurin and selenazofurin against togaviruses, bunyaviruses, and arenaviruses.* Antimicrob Agents Chemother, 1984. **26**(4): p. 476-80.
154. Jordan, I., et al., *Ribavirin inhibits West Nile virus replication and cytopathic effect in neural cells.* J Infect Dis, 2000. **182**(4): p. 1214-7.
155. Kumar, R., et al., *Randomized, controlled trial of oral ribavirin for Japanese encephalitis in children in Uttar Pradesh, India.* Clin Infect Dis, 2009. **48**(4): p. 400-6.
156. Carrillo-Bustamante, P., et al., *Determining Ribavirin's mechanism of action against Lassa virus infection.* Sci Rep, 2017. **7**(1): p. 11693.
157. Lau, J.Y., et al., *Mechanism of action of ribavirin in the combination treatment of chronic HCV infection.* Hepatology, 2002. **35**(5): p. 1002-9.
158. Leyssen, P., et al., *The predominant mechanism by which ribavirin exerts its antiviral activity in vitro against flaviviruses and paramyxoviruses is mediated by inhibition of IMP dehydrogenase.* J Virol, 2005. **79**(3): p. 1943-7.
159. Colombo, G., et al., *Brain distribution of ribavirin after intranasal administration.* Antiviral Res, 2011. **92**(3): p. 408-14.
160. Warrell, M.J., et al., *Failure of interferon alfa and tribavirin in rabies encephalitis.* BMJ, 1989. **299**(6703): p. 830-3.
161. Crumpacker, C., et al., *Ribavirin enters cerebrospinal fluid.* Lancet, 1986. **2**(8497): p. 45-6.
162. Marschalek, A., L. Drechsel, and K.K. Conzelmann, *The importance of being short: the role of rabies virus phosphoprotein isoforms assessed by differential IRES translation initiation.* Eur J Cell Biol, 2012. **91**(1): p. 17-23.

163. Lockhart, B.P., N. Tordo, and H. Tsiang, *Inhibition of rabies virus transcription in rat cortical neurons with the dissociative anesthetic ketamine.* Antimicrob Agents Chemother, 1992. **36**(8): p. 1750-5.
164. Benet, L.Z., et al., *BDDCS, the Rule of 5 and drugability.* Adv Drug Deliv Rev, 2016. **101**: p. 89-98.
165. Chavez, J.H., et al., *Evaluation of antiviral activity of phenolic compounds and derivatives against rabies virus.* Vet Microbiol, 2006. **116**(1-3): p. 53-9.
166. Wu, Y.H., et al., *Structure Properties and Mechanisms of Action of Naturally Originated Phenolic Acids and Their Derivatives against Human Viral Infections.* Curr Med Chem, 2017. **24**(38): p. 4279-4302.
167. Lingappa, U.F., et al., *Host-rabies virus protein-protein interactions as druggable antiviral targets.* Proc Natl Acad Sci U S A, 2013. **110**(10): p. E861-8.
168. Marosi, A., et al., *Evaluation of in vitro inhibitory potential of type-I interferons and different antiviral compounds on rabies virus replication.* Vaccine, 2018.
169. Han, Z., et al., *Small-molecule probes targeting the viral PPxY-host Nedd4 interface block egress of a broad range of RNA viruses.* J Virol, 2014. **88**(13): p. 7294-306.
170. Appolinario, C.M. and A.C. Jackson, *Antiviral therapy for human rabies.* Antivir Ther, 2015. **20**(1): p. 1-10.
171. Jochmans, D. and J. Neyts, *The path towards effective antivirals against rabies.* Vaccine, 2019. **37**(33): p. 4660-4662.
172. Marosi, A., et al., *Combination therapy of rabies-infected mice with inhibitors of pro-inflammatory host response, antiviral compounds and human rabies immunoglobulin.* Vaccine, 2019. **37**(33): p. 4724-4735.
173. Randrup Hansen, C., et al., *Effects and Side Effects of Using Sorafenib and Sunitinib in the Treatment of Metastatic Renal Cell Carcinoma.* Int J Mol Sci, 2017. **18**(2).
174. Gole, P., et al., *Side effects of Sorafenib and sunitinib: A new concern for dermatologist and oncologist.* Indian Dermatol Online J, 2014. **5**(1): p. 89-91.
175. Wolf, G., *[Comments on the article "Cutaneous side effects of the multikinase inhibitors sorafenib and sunitinib"].* Hautarzt, 2011. **62**(7): p. 560; author reply 561-4.
176. Wollenberg, A., M. Staehler, and T. Eames, *[Cutaneous side effects of the multikinase inhibitors sorafenib and sunitinib].* Hautarzt, 2010. **61**(8): p. 662-7.
177. Autier, J., et al., *[Cutaneous side effects of sorafenib and sunitinib].* Ann Dermatol Venereol, 2008. **135**(2): p. 148-53; quiz 147, 154.
178. Jackson, A.C., *Is minocycline useful for therapy of acute viral encephalitis?* Antiviral Res, 2012. **95**(3): p. 242-4.
179. Zink, M.C., et al., *Neuroprotective and anti-human immunodeficiency virus activity of minocycline.* JAMA, 2005. **293**(16): p. 2003-11.
180. Jackson, A.C., et al., *Therapy with minocycline aggravates experimental rabies in mice.* J Virol, 2007. **81**(12): p. 6248-53.
181. Yang, Y.J., et al., *Small interfering RNAs targeting the rabies virus nucleoprotein gene.* Virus Res, 2012. **169**(1): p. 169-74.
182. Gupta, P.K., et al., *Intracerebral delivery of small interfering RNAs (siRNAs) using adenoviral vector protects mice against lethal peripheral rabies challenge.* Virus Res, 2012. **163**(1): p. 11-8.

183. DeVincenzo, J., et al., *Evaluation of the safety, tolerability and pharmacokinetics of ALN-RSV01, a novel RNAi antiviral therapeutic directed against respiratory syncytial virus (RSV).* Antiviral Res, 2008. **77**(3): p. 225-31.
184. Ferreira, H.L., et al., *Inhibition of avian metapneumovirus (AMPV) replication by RNA interference targeting nucleoprotein gene (N) in cultured cells.* Antiviral Res, 2007. **74**(1): p. 77-81.
185. Lu, L., Y. Ho, and J. Kwang, *Suppression of porcine arterivirus replication by baculovirus-delivered shRNA targeting nucleoprotein.* Biochem Biophys Res Commun, 2006. **340**(4): p. 1178-83.
186. Real, E., et al., *Antiviral drug discovery strategy using combinatorial libraries of structurally constrained peptides.* J Virol, 2004. **78**(14): p. 7410-7.
187. Castel, G., et al., *Peptides that mimic the amino-terminal end of the rabies virus phosphoprotein have antiviral activity.* J Virol, 2009. **83**(20): p. 10808-20.
188. Papaneri, A.B., et al., *Alanine scanning of the rabies virus glycoprotein antigenic site III using recombinant rabies virus: implication for post-exposure treatment.* Vaccine, 2013. **31**(49): p. 5897-902.
189. Holmes, E.C., et al., *Genetic constraints and the adaptive evolution of rabies virus in nature.* Virology, 2002. **292**(2): p. 247-57.
190. Sakamoto, S., et al., *Studies on the structures and antigenic properties of rabies virus glycoprotein analogues produced in yeast cells.* Vaccine, 1999. **17**(3): p. 205-18.
191. Roche, S., et al., *Structures of vesicular stomatitis virus glycoprotein: membrane fusion revisited.* Cell Mol Life Sci, 2008. **65**(11): p. 1716-28.
192. Grill, A.K., *Approach to management of suspected rabies exposures: what primary care physicians need to know.* Can Fam Physician, 2009. **55**(3): p. 247-51.
193. Lentz, T.L., E. Hawrot, and P.T. Wilson, *Synthetic peptides corresponding to sequences of snake venom neurotoxins and rabies virus glycoprotein bind to the nicotinic acetylcholine receptor.* Proteins, 1987. **2**(4): p. 298-307.
194. Evans, J.S., et al., *Antigenic site changes in the rabies virus glycoprotein dictates functionality and neutralizing capability against divergent lyssaviruses.* J Gen Virol, 2018. **99**(2): p. 169-180.
195. Sun, L., et al., *[Generation of Human ScFv Antibodies for Antigenic Site III of Rabies Virus Glycoprotein from Antibody-phage Libraries by Chain Shuffling].* Bing Du Xue Bao, 2016. **32**(4): p. 393-8.
196. Fallahi, F., A.I. Wandeler, and S.A. Nadin-Davis, *Characterization of epitopes on the rabies virus glycoprotein by selection and analysis of escape mutants.* Virus Res, 2016. **220**: p. 161-71.
197. Kankanamge, P.J., et al., *Mapping of the low pH-sensitive conformational epitope of rabies virus glycoprotein recognized by a monoclonal antibody #1-30-44.* Microbiol Immunol, 2003. **47**(7): p. 507-19.
198. Schnell, M.J. and K.K. Conzelmann, *Polymerase activity of in vitro mutated rabies virus L protein.* Virology, 1995. **214**(2): p. 522-30.
199. Campbell, J.B., et al., *The inhibition of rabies virus by arabinosyl cytosine. Studies on the mechanism and specificity of action.* Virology, 1968. **34**(4): p. 701-8.

200. Harmon, M.W. and B. Janis, *Effects of cytosine arabinoside, adenine arabinoside, and 6-azauridine on rabies virus in vitro and in vivo.* J Infect Dis, 1976. **133**(1): p. 7-13.
201. Sodja, I. and A. Holy, *Effect of 9-(S)-(2,3-dihydroxypropyl)adenine on experimental rabies infection in laboratory mice.* Acta Virol, 1980. **24**(5): p. 317-24.
202. Banyard, A.C., et al., *Re-evaluating the effect of Favipiravir treatment on rabies virus infection.* Vaccine, 2019. **37**(33): p. 4686-4693.
203. Yamada, K., et al., *Efficacy of Favipiravir (T-705) in Rabies Postexposure Prophylaxis.* J Infect Dis, 2016. **213**(8): p. 1253-61.
204. Poch, O., et al., *Sequence comparison of five polymerases (L proteins) of unsegmented negative-strand RNA viruses: theoretical assignment of functional domains.* J Gen Virol, 1990. **71 (Pt 5)**: p. 1153-62.
205. Albertini, A.A., et al., *Structural aspects of rabies virus replication.* Cell Mol Life Sci, 2008. **65**(2): p. 282-94.
206. Li, J., J.T. Wang, and S.P. Whelan, *A unique strategy for mRNA cap methylation used by vesicular stomatitis virus.* Proc Natl Acad Sci U S A, 2006. **103**(22): p. 8493-8.
207. Li, J., E.C. Fontaine-Rodriguez, and S.P. Whelan, *Amino acid residues within conserved domain VI of the vesicular stomatitis virus large polymerase protein essential for mRNA cap methyltransferase activity.* J Virol, 2005. **79**(21): p. 13373-84.
208. Hemachudha, T., et al., *Failure of therapeutic coma and ketamine for therapy of human rabies.* J Neurovirol, 2006. **12**(5): p. 407-9.
209. Anindita, P.D., et al., *Ribavirin-related compounds exert in vitro inhibitory effects toward rabies virus.* Antiviral Res, 2018. **154**: p. 1-9.
210. Banyard, A.C., et al., *Re-evaluating the effect of Favipiravir treatment on rabies virus infection.* Vaccine, 2017.
211. Rose, J.K., *Positive strands to the rescue again: a segmented negative-strand RNA virus derived from cloned cDNAs.* Proc Natl Acad Sci U S A, 1996. **93**(26): p. 14998-5000.
212. Yan, D., et al., *Dual myxovirus screen identifies a small-molecule agonist of the host antiviral response.* J Virol, 2013. **87**(20): p. 11076-87.
213. Weisshaar, M., et al., *Identification and Characterization of Influenza Virus Entry Inhibitors through Dual Myxovirus High-Throughput Screening.* J Virol, 2016. **90**(16): p. 7368-7387.
214. Krumm, S.A., et al., *Potent host-directed small-molecule inhibitors of myxovirus RNA-dependent RNA-polymerases.* PLoS One, 2011. **6**(5): p. e20069.
215. Zhang, J.H., T.D. Chung, and K.R. Oldenburg, *A Simple Statistical Parameter for Use in Evaluation and Validation of High Throughput Screening Assays.* J Biomol Screen, 1999. **4**(2): p. 67-73.
216. Yan, X., et al., *The rabies virus glycoprotein determines the distribution of different rabies virus strains in the brain.* J Neurovirol, 2002. **8**(4): p. 345-52.
217. Ellison, J.A., et al., *Multidisciplinary approach to epizootiology and pathogenesis of bat rabies viruses in the United States.* Zoonoses Public Health, 2013. **60**(1): p. 46-57.
218. Reardon, T.R., et al., *Rabies Virus CVS-N2c(DeltaG) Strain Enhances Retrograde Synaptic Transfer and Neuronal Viability.* Neuron, 2016. **89**(4): p. 711-24.
219. Morimoto, K., et al., *Rabies virus quasispecies: implications for pathogenesis.* Proc Natl Acad Sci U S A, 1998. **95**(6): p. 3152-6.

220. Yan, D., et al., *Cross-resistance mechanism of respiratory syncytial virus against structurally diverse entry inhibitors.* Proc Natl Acad Sci U S A, 2014. **111**(33): p. E3441-9.
221. Mackman, R.L., et al., *Discovery of an oral respiratory syncytial virus (RSV) fusion inhibitor (GS-5806) and clinical proof of concept in a human RSV challenge study.* J Med Chem, 2015. **58**(4): p. 1630-43.
222. Lama, Z., et al., *Kinase inhibitors tyrphostin 9 and rottlerin block early steps of rabies virus cycle.* Antiviral Res, 2019. **168**: p. 51-60.
223. Wirblich, C. and M.J. Schnell, *Rabies virus (RV) glycoprotein expression levels are not critical for pathogenicity of RV.* J Virol, 2011. **85**(2): p. 697-704.
224. Morimoto, K., et al., *Reinvestigation of the role of the rabies virus glycoprotein in viral pathogenesis using a reverse genetics approach.* J Neurovirol, 2000. **6**(5): p. 373-81.
225. Takayama-Ito, M., et al., *Multiple amino acids in the glycoprotein of rabies virus are responsible for pathogenicity in adult mice.* Virus Res, 2006. **115**(2): p. 169-75.
226. Perron, M., et al., *GS-5806 Inhibits a Broad Range of Respiratory Syncytial Virus Clinical Isolates by Blocking the Virus-Cell Fusion Process.* Antimicrob Agents Chemother, 2015. **60**(3): p. 1264-73.
227. Hashiguchi, T., et al., *Structures of the prefusion form of measles virus fusion protein in complex with inhibitors.* Proc Natl Acad Sci U S A, 2018. **115**(10): p. 2496-2501.
228. Ozawa, T., *Designing split reporter proteins for analytical tools.* Anal Chim Acta, 2006. **556**(1): p. 58-68.
229. Abrahamyan, L.G., et al., *The cytoplasmic tail slows the folding of human immunodeficiency virus type 1 Env from a late prebundle configuration into the six-helix bundle.* J Virol, 2005. **79**(1): p. 106-15.
230. Gaudin, Y., et al., *Biological function of the low-pH, fusion-inactive conformation of rabies virus glycoprotein (G): G is transported in a fusion-inactive state-like conformation.* J Virol, 1995. **69**(9): p. 5528-34.
231. Ilina, E.N., et al., *Recombinant Monoclonal Antibodies for Rabies Post-exposure Prophylaxis.* Biochemistry (Mosc), 2018. **83**(1): p. 1-12.
232. Sun, X., S. Belouzard, and G.R. Whittaker, *Molecular architecture of the bipartite fusion loops of vesicular stomatitis virus glycoprotein G, a class III viral fusion protein.* J Biol Chem, 2008. **283**(10): p. 6418-27.
233. Plattet, P., et al., *Signal peptide and helical bundle domains of virulent canine distemper virus fusion protein restrict fusogenicity.* J Virol, 2007. **81**(20): p. 11413-25.
234. Horvath, C.M. and R.A. Lamb, *Studies on the fusion peptide of a paramyxovirus fusion glycoprotein: roles of conserved residues in cell fusion.* J Virol, 1992. **66**(4): p. 2443-55.
235. Sergel, T.A., L.W. McGinnes, and T.G. Morrison, *A single amino acid change in the Newcastle disease virus fusion protein alters the requirement for HN protein in fusion.* J Virol, 2000. **74**(11): p. 5101-7.
236. Terrier, O., et al., *Characterization of naturally occurring parainfluenza virus type 2 (hPIV-2) variants.* J Clin Virol, 2008. **43**(1): p. 86-92.
237. Fredericksen, B.L. and M.A. Whitt, *Vesicular stomatitis virus glycoprotein mutations that affect membrane fusion activity and abolish virus infectivity.* J Virol, 1995. **69**(3): p. 1435-43.

238. Martinez, I. and G.W. Wertz, *Biological differences between vesicular stomatitis virus Indiana and New Jersey serotype glycoproteins: identification of amino acid residues modulating pH-dependent infectivity.* J Virol, 2005. **79**(6): p. 3578-85.
239. Shakin-Eshleman, S.H., et al., *N-linked glycosylation of rabies virus glycoprotein. Individual sequons differ in their glycosylation efficiencies and influence on cell surface expression.* J Biol Chem, 1992. **267**(15): p. 10690-8.
240. Yamada, K., et al., *Addition of a single N-glycan to street rabies virus glycoprotein enhances virus production.* J Gen Virol, 2013. **94**(Pt 2): p. 270-5.
241. Yamada, K., K. Noguchi, and A. Nishizono, *Characterization of street rabies virus variants with an additional N-glycan at position 247 in the glycoprotein.* Arch Virol, 2014. **159**(2): p. 207-16.
242. Gaudin, Y., et al., *Identification of amino acids controlling the low-pH-induced conformational change of rabies virus glycoprotein.* J Virol, 1996. **70**(11): p. 7371-8.

4 APPENDICES

4.1 Appendix A Chapter 1 Results and Discussion Source

PLOS PATHOGENS

RESEARCH ARTICLE

Bipartite interface of the measles virus phosphoprotein X domain with the large polymerase protein regulates viral polymerase dynamics

Venice Du Pont[1], **Yi Jiang**[2], **Richard K. Plemper**[1]*

1 Institute for Biomedical Sciences, Georgia State University, Atlanta, Georgia, United States of America, **2** Department of Mathematics and Statistics, Georgia State University, Atlanta, Georgia, United States of America

* rplemper@gsu.edu

OPEN ACCESS

Citation: Du Pont V, Jiang Y, Plemper RK (2019) Bipartite interface of the measles virus phosphoprotein X domain with the large polymerase protein regulates viral polymerase dynamics. PLoS Pathog 15(8): e1007995. https://doi.org/10.1371/journal.ppat.1007995

Editor: Sean P.J. Whelan, Harvard Medical School, UNITED STATES

Received: May 3, 2019

Accepted: July 22, 2019

Published: August 5, 2019

Data Availability Statement: All relevant data are within the manuscript and its Supporting Information files.

Funding: This work was supported, in part, by Public Health Service grants R01CA201340 and 1R01EY028450 from the NIH/NCI and NIH/NEI, respectively (to Y.J.), and AI071002 and HD079327 from the NIH/NIAID and NIH/NICHD, respectively (to R.K.P.). The funders had no role in study design, data collection and analysis, decision to publish, or preparation of the manuscript.

Abstract

Measles virus (MeV) is a highly contagious, re-emerging, major human pathogen. Replication requires a viral RNA-dependent RNA polymerase (RdRP) consisting of the large (L) polymerase protein complexed with the homo-tetrameric phosphoprotein (P). In addition, P mediates interaction with the nucleoprotein (N)-encapsidated viral RNA genome. The nature of the P:L interface and RdRP negotiation of the ribonucleoprotein template are poorly understood. Based on biochemical interface mapping, swapping of the central P tetramerization domain (OD) for yeast GCN4, and functional assays, we demonstrate that the MeV P-to-L interface is bipartite, comprising a coiled-coil microdomain proximal to the OD and an unoccupied face of the triangular prism-shaped C-terminal P X-domain (P-XD), which is distinct from the known P-XD face that binds N-tail. Mixed null-mutant P tetramers regained L-binding competence in a ratio-dependent manner and fully reclaimed bioactivity in minireplicon assays and recombinant MeV, demonstrating that the individual L-binding interface elements are physically and mechanistically distinct. P-XD binding competence to L and N was likewise trans-complementable, which, combined with mathematical modeling, enabled the mechanistic characterization of P through two- and stoichiometrically-controlled three-way complementations. Only one each of the four XDs per P tetramer must be L or N binding-competent for bioactivity, but interaction of the same P-XD with L and N was mutually exclusive, and L binding superseded engaging N. Mixed P tetramers with a single, designated L binding-competent P-XD caused significant RdRP hyperactivity, outlining a model of iterative resolution and reformation of the P-XD:L interface regulating polymerase mobility.

Author summary

MeV belongs to the order of non-segmented negative polarity RNA viruses, which includes devastating human pathogens. While all feature encapsidated RNA genomes and P-L type polymerase complexes, insight into the intermolecular interactions within the

4.2 Appendix B Chapter 2 Introduction, Tables, Figures 15 and 16 Source

Available online at www.sciencedirect.com

ScienceDirect

Current Opinion in Virology

Status of antiviral therapeutics against rabies virus and related emerging lyssaviruses

Venice Du Pont[1], Richard K Plemper[1] and Matthias J Schnell[2]

Rabies virus (RABV) constitutes a major social and economic burden associated with 60 000 deaths annually worldwide. Although pre-exposure and post-exposure treatment options are available, they are efficacious only when initiated before the onset of clinical symptoms. Aggravating the problem, the current RABV vaccine does not cross-protect against the emerging zoonotic phylogroup II lyssaviruses. A requirement for an uninterrupted cold chain and high cost of the immunoglobulin component of rabies prophylaxis generate an unmet need for the development of RABV-specific antivirals. We discuss desirable anti-RABV drug profiles, past efforts to address the problem and inhibitor candidates identified, and examine how the rapidly expanding structural insight into RABV protein organization has illuminated novel druggable target candidates and paved the way to structure-aided drug optimization. Special emphasis is given to the viral RNA-dependent RNA polymerase complex as a promising target for direct-acting broad-spectrum RABV inhibitors.

Addresses
[1] Institute for Biomedical Sciences, Georgia State University, Atlanta, GA, United States
[2] Department of Microbiology and Immunology, Sidney Kimmel Medical College at Thomas Jefferson University, Philadelphia, PA, United States

Corresponding authors: Plemper, Richard K (rplemper@gsu.edu), Schnell, Matthias J (matthias.schnell@jefferson.edu)

Current Opinion in Virology 2019, **35**:1–13

This review comes from a themed issue on **Antiviral strategies**

Edited by **Margo A Brinton** and **Richard K Plemper**

For a complete overview see the Issue and the Editorial

Available online 10th February 2019

https://doi.org/10.1016/j.coviro.2018.12.009

Introduction

The devastating signs and symptoms of rabies disease have been documented as far back as 2000 B.C. in the Eshnunna tablets of Mesopotamia [1]. Even now, in the second millennia A.D, rabies disease continues to be a social and economic hardship with approximately 60 000 deaths worldwide, nearly $8.6 billion in economic burden, and $1.5 billion spent on post-exposure prophylaxis treatment (PEP) alone [2]. The causative agents, lyssaviruses, within the *Rhabdoviridae* family, are characterized as zoonotic, neurotropic negative-sense non-segmented RNA viruses. Transmission of rabies virus (RABV) occurs typically through the transfer of infectious saliva from the percutaneous bite of a mammal, usually a dog [2]. Through axoplasmic transport, RABV enters the central nervous system (CNS) where it begins to replicate, causing severe neuronal dysfunction [3–5]. Rabies is vaccine-preventable as well as treatable early after infection. After the onset of clinical symptoms, however, almost all patients succumb to the infection, progressing toward coma and ultimately death [6•]. RABV's ability to effectively subvert the host immune system through evasion of TLR signaling, down-regulation of IFN signaling, and prevention of adaptive responses by maintaining lowered blood–brain barrier (BBB) permeability, and induction of T-cell apoptosis exemplifies why early intervention is critical [7,8,9•]. As depicted in Figure 1, treatment of rabies consists of rabies immune-globin (RIG) and four doses of the vaccine over a four-week period. PEP is recommended for previously vaccinated individuals as well, and consists of vaccine doses on days 0 and 3. A single PEP regimen costs at least $3000 in the United States [2]. This expense of rabies PEP is predominantly due to the high cost of producing human rabies immune-globin HRIG, a human plasma-based product, with a relatively short shelf life and need for extensive quality assurance [10]. A second contributor to the high treatment cost is the requirement of four doses of rabies vaccine, which typically costs $260 per dose in the USA and Europe. In Africa and Asia, where 95% of rabies-related deaths occur, PEP averages $40 and $49, respectively. This expense is often out of reach in areas with a daily family income of approximately $1–2. The number of people worldwide that receive rabies PEP as well as the crippling debt associated with it is estimated to reach a staggering 15 million annually [2]. Furthermore, the current vaccine is likely ineffective against emerging zoonotic lyssaviruses of phylogroup II such as Mokola (MOKV) and Lagos bat viruses [11–15]. The high cost of HRIG and the current vaccine, along with cold-chain requirements for both, present an urgent and unmet clinical need for the development of safe, cost-effective, efficacious, shelf-stable, and cross-protective antivirals against lyssavirus phylogroups associated with human rabies disease. Antiviral compounds could be used to replace the HRIG or other RIG component in current rabies PEP (Table 1).

Lyssavirus virion organization

Lyssaviruses contain RNA genomes of approximately 12 kb. The virion of lyssaviruses, as with the other family members of *Rhabdoviridae*, is characterized by a bullet-